Development of a Passively Q-switched Microchip Laser Operating at 914 nm for Automotive Lidar Applications

A thesis accepted by the Faculty of Aerospace Engineering and Geodesy of the University of Stuttgart in partial fulfilment of the requirements for the degree of Doctor rerum naturalium (Dr. rer. nat.)

by
Marco Nägele
born in Künzelsau

Main referee: Prof. Dr. rer. nat. Thomas Dekorsy
Co-referee: PD Dr. habil. Christian Kränkel
Date of defense: 11. July 2022

Institute of Aerospace Thermodynamics
University of Stuttgart
Institute of Technical Physics
DLR, Stuttgart
2022

CONTENTS

ABSTRACT

Since most solid-state lasers have emission wavelengths above one micrometer, they cannot be used for contemporary lidar systems in combination with inexpensive and widely established silicon-based detector technology. Therefore, the aim of this work is to investigate and realize a passively Q-switched Nd^{3+}:YVO_4 laser at a wavelength of 914 nm for the application in an automotive lidar sensor.

To investigate the laser parameters relevant for the lidar application, a total of three experimental resonator configurations is used. Thereby, the configurations are chosen in such a way that the laser parameters can be analyzed as decoupled as possible from the overall system. Experimental investigations demonstrate that the quasi-continuously pumped Nd^{3+}:YVO_4 laser can achieve pulse durations in the single-digit nanosecond range and pulse energies of almost 40 µJ. Moreover, for a possible lidar application, the repetition rate can be scaled up to about 60 kHz via the applied pump power without significantly affecting the other parameters. Theoretical comparison via a rate equation model provides close agreement with the experiments and enables an assessment of the future potential for possible applications of the laser. Across all studies, a very good beam quality was observed, which suggests an excellent resolution capability in lidar applications.

In addition to the consideration of various system relationships using the experimental configurations, a passively Q-switched monolithic resonator approach is presented operating in a single-pulse regime at a repetition rate of 200 Hz. The system is pumped by a 808 nm single broad area laser diode, which offers a more compact overall system and a narrower linewidth compared to a fiber-coupled diode laser module.

Consequently, the entire laser system can be operated without active temperature control in a temperature range of 20-50 °C merely by adjusting the pump laser current. Besides short pulse durations, the short resonator of the monolithic laser crystal allows operation on a single longitudinal mode and consequently a spectral emission bandwidth of a few picometers only. This results in excellent stability of the spectral properties, the pulse energy, and the pulse duration for long-term measurements over 60 minutes.

ZUSAMMENFASSUNG

Die meisten Festkörperlaser besitzen Emissionswellenlängen oberhalb eines Mikrometers und können deshalb nicht für moderne Lidarsysteme in Kombination mit günstiger und weit etablierter siliziumbasierten Detektortechnologie verwendet werden. Ziel dieser Arbeit ist daher die Untersuchung und Realisierung eines passiv gütegeschalteten Nd^{3+}:YVO_4 Lasers bei einer Wellenlänge von 914 nm für die Anwendung in einem automobilen Lidar Sensor.
Zur Untersuchung der für die Lidaranwendung relevanten Laserparameter werden insgesamt drei experimentelle Resonatorkonfigurationen verwendet. Die Konfigurationen sind dabei so gewählt, dass die Laserparameter möglichst entkoppelt vom Gesamtsystem analysiert werden können. Experimentelle Untersuchungen zeigen, dass der quasikontinuierlich gepumpte Nd^{3+}:YVO_4 Laser Pulsdauern im einstelligen Nanosekundenbereich und Pulsenergien von knapp 40 µJ erreichen kann. Zudem lässt sich für eine mögliche Lidaranwendung die Repetitionsrate bis ungefähr 60 kHz über die verwendete Pumpleistung skalieren. Der Vergleich mit der Theorie basierend auf Ratengleichungen zeigt eine gute Übereinstimmung zum Experiment, woraus sich das zukünftige Potential des Lasers für mögliche Anwendungen abschätzen lässt. Über alle Untersuchungen hinweg konnte eine sehr gute Strahlqualität beobachtet werden, was in der Lidaranwendung ein hervorragendes Auflösevermögen verspricht.
Neben der Betrachtung verschiedener Systemzusammenhänge mittels experimenteller Konfigurationen wird ein kompakter, monolithischer, passiv gütegeschalteter Demonstratoraufbau im Einzelpulsbetrieb bei einer Wiederholrate von 200 Hz präsentiert. Hierbei kommt als Pum-

plaser ein 808 nm Breitstreifen-Diodenlaser zum Einsatz, welcher verglichen mit einem fasergekoppelten Laserdiodenmodul nicht nur ein deutlich kompakteres Gesamtsystem verspricht, sondern ebenfalls eine schmalere Linienbreite besitzt. Folglich kann das Gesamtsystem allein durch Anpassung des Pumplaserstroms und ohne aktive Temperaturstabilisierung in einem Temperaturbereich von 20-50 °C stabil betrieben werden. Zudem liefert der kurze Resonator des monolithischen Laserkristalls nicht nur kurze Pulsdauern, sondern ermöglicht ebenfalls den Betrieb auf einer einzelnen longitudinalen Mode und folglich spektrale Emissionsbandbreiten von wenigen Pikometern. Hierdurch ergibt sich für Langzeitmessungen über 60 Minuten eine hervorragende Stabilität der spektralen Eigenschaften, der Pulsenergie und der Pulsdauer.

1 INTRODUCTION

Nowadays, light detection and ranging (lidar) systems are indispensable. They play an important role in metrology, where weather and climate data are collected [1–3], in agriculture, where deforestation [4], terrain profiles [5], and the targeted distribution of fertilizers are mapped, but also find application in the measurement of air pollution [6, 7]. Likewise, lidar sensors can be used in the automotive industry [8] and take an important role in the mobility of the future where these systems are considered as one of the key technologies for automated driving [9].
While the applications of lidar systems are extremely diverse, the underlying principle of all sensors is the same. Light is emitted from the sensor via a laser, reflected at objects in the field, and then imaged via a receive path onto the detector to sense the environment. Thereby, the distance determination to the object can be conducted either using an indirect coherent method or a direct time-of-flight (TOF) measurement. With the coherent detection method, the emitted signal is compared with a local oscillator which is tunable in time. Using this technique, both the phase and the intensity of the received signal can be measured. However, the major challenge with this method is that an optically heterodyne system is required. For this reason, the continuously operated laser must have a coherence length as large as possible, at which the amplitude or frequency can be tuned quickly and, especially, independent of environmental influences.
Regardless of which of the two detection methods is used, the laser, along with the detector and electronics, plays an important role related to the overall performance of the lidar sensor.

The key requirements of an automotive lidar sensor include a sufficiently long detection range, an accurate depth resolution, a large field of view (FOV), a precise angular resolution, and a high measurement speed. In addition, the sensor should be as compact as possible, inexpensive, and insensitive to external environmental influences and background light. Since in many cases the different requirements influence each other, a certain trade-off has to be taken into account, and consequently requirements must be prioritized according to the application.
Even with comparatively low pulse energies and poorly reflecting targets, high sensor ranges can be achieved using single-photon detectors and evaluation electronics based on photon-timing (time-to-digital converter, TDC) and photon-counting (digital gated counter) [10]. In addition to photomultiplier tubes, modern silicon-based single-photon avalanche diode (SPAD) arrays are suitable as single-photon detectors [11–13]. These detectors are available in large quantities, have a high pixel count up to the megapixel range [14, 15], and can reliably detect even single reflected photons. Furthermore, with a typical dead time of a few nanoseconds, they can be used at repetition rates up to 100 MHz [16].
To suppress background light and maximize the sensing range, a histogram can be computed from incoming photons. Further, spectrally narrowband laser light sources can be combined with narrow optical bandpass filters. However, the challenge here is to ensure that the laser linewidth is in the sub-nanometer range and, in addition, the central wavelength should shift only slightly with an alternating temperature of the gain medium. Relative to the temperature requirement range of the lidar sensor, this typically results in bandpass filters with a spectral transmission window between 5 nm to 40 nm width [10].
Besides the choice of detector and suppression of background light, the straightforward route to extend the sensor range is to increase the emitted pulse energy. On one hand, this requires that the laser is capable

of increasing the pulse energy at the required repetition rate and pulse duration. On the other hand, eye safety considerations also have to be ensured for lidar sensors in the automotive sector.

According to the international standard, the maximum permissible exposure (MPE) is the maximum permissible energy density and depends strongly on the laser wavelength used. Although significantly higher energy densities are possible at wavelengths above 1400 nm compared with 900 nm as defined by the MPE, this is by no means the only criterion for the choice of laser [17]. Other important factors are the availability, overall performance, as well as the cost of detectors and lasers. Moreover, external environmental conditions play a non-negligible role in the choice of laser wavelength, as absorption bands of air molecules, fog, rain, and snow can have a significant influence on the range of the lidar sensor [18].

Alternatively, the energy density can be reduced by widening the beam diameter or the utilization of a micropulse lidar approach. Using a micropulse lidar approach, low energy pulses in the microjoule regime are averaged at repetition rates of several kilohertz to improve the signal-to-noise ratio. Due to the low individual pulse energies and sufficient beam expansion, the lidar system remains eye-safe. When this approach was invented in 1993, it was still limited by comparatively insensitive detector technology and the maximum repetition rate of the lasers [19]. However, the aforementioned single-photon detectors and in combination with passively Q-switched lasers with repetition rates in the sub-100 kHz range and pulse energies in the mid-double-digit µJ range, open up completely new possibilities. With short pulse durations of a few nanoseconds, good longitudinal resolution can be achieved, while high repetition rates provide sufficient signal at the detector and high acquisition rates.

For lidar sensors, different possibilities for the illumination of the scene can be considered to detect objects in the field [20]. Besides point scan-

ning of the field using micro or galvo mirror systems and the flash approach, where the whole scene is illuminated at once, illuminating the scene with a laser line offers a good compromise. Using a laser line it is possible to achieve both a relatively large FoV while maintaining a high frame rate, as well as acquisition speed and comparatively low pulse energy [10]. At the same time, when illuminating the scene using a scanning or rotating laser line, it is possible to use the laser in a quasi-continuous wave (QCW) operation mode. Thereby the laser is modulated periodically and the illumination of the field is synchronized with the laser to achieve the desired FoV. For QCW operation, the duty cycle indicates the ratio of the lasing duration to the total periodic duration. Thus a low duty cycle can reduce the thermal load in the laser itself, but also in the entire sensor.

The laser types most frequently used in lidar systems are based on semiconductor technology. Reasons for this are the wide market availability, the emission wavelength that can be mostly selected by design, and an attractive price at least for low pulse energies and high volumes. In this context, semiconductor edge and surface emitters are used in equal measure. But both of these lasers have their own characteristics and limitations.
For edge emitters, the output power scales with the width of the active zone. In addition, depending on the output power, the ratio of the exit aperture varies greatly, resulting in a very asymmetrical beam profile with a slow and fast optical axis. In contrast, surface emitters have a comparatively low output power but good beam quality. To achieve sufficient pulse energies, they can be arranged as an array, but this, in turn, requires the use of elaborate lens assemblies to homogenize the single emitters. The common features of both types of semiconductor lasers in pulsed laser operation are the high required peak currents and the relatively poor conversion efficiency. Moreover, the achievement of

short laser pulses in the ns range requires the use of complex driver circuits, as well as good shielding of electromagnetic compatibility (EMC) sensitive components due to the high electromagnetic fields.

A possible alternative to semiconductor lasers is the use of a solid-state laser. Especially for lidar applications with pulse energies above a few microjoules, passively Q-switched solid-state lasers offer enormous potential and provide certain advantages compared to semiconductor lasers.

First of all, those lasers generally possess an almost diffraction-limited beam quality which allows high spatial resolutions to be achieved in lidar applications. Furthermore, compared to semiconductor lasers, the pulse energy does not scale with the emitter or array size, but only with the average power of the pump laser. Consequently, extremely compact systems with scalable pulse energies down to the double-digit mJ range are already state-of-the-art [21, 22]. In addition, shielding of EMC-sensitive components is not required due to the lack of high peak currents and complex driver circuits. In particular, passively Q-switched microchip lasers possess a short resonator, which allows short pulse durations in the ns or sub-ns range [23, 24]. In general, this not only allows for a small package volume but also enables a small longitudinal resolution of the lidar sensor due to short laser pulse durations. Another advantage of solid-state lasers is that in the case of rare-earth ion doped crystals they can have very small gain bandwidths. Therefore operation on a single longitudinal mode is possible with short resonators. Also, the atomic transition leads to temperature-dependent wavelength shifts in the range of a few picometers per degree Kelvin [25]. Likewise, semiconductor lasers can also achieve relatively narrow linewidths <0.2 nm [26], but this typically translates into smaller output powers or significantly more complex device design and fabrication [27]. On top of that, the greater thermal wavelength shift of $0.3\,\mathrm{nm\,K^{-1}}$ for edge emitters and $0.07\,\mathrm{nm\,K^{-1}}$ for surface emitters, respectively, typically leads to lim-

itations when considering the automotive temperature requirement for lidar sensors [28, 29].
However, for pulsed lidar sensors based on solid-state lasers, semiconductor lasers are still required. Diode lasers in continuous wave (CW) and QCW operation are extremely efficient with wall-plug conversion efficiencies >50 % and are therefore ideally suited as pump sources for solid-state lasers. Due to the relatively narrow-band emission, a good spectral overlap with the absorption bands of active ions of solid-state laser crystals can be generated. Furthermore, laser diodes in the longitudinal pump configuration allow a high spatial overlap with the solid-state laser mode and consequently an extremely efficient excitation.

Overall, it appears that diode-pumped passively Q-switched solid-state lasers are well suited for lidar applications. However, there are certain challenges and points that need to be considered. Passively Q-switched lasers offer an extremely simplistic system design without active modulators and large applied voltages, but the timing is determined by the laser dynamics itself. The resulting temporal jitter is roughly on the order of a few percent of the laser repetition rate [30] and consequently requires timing monitoring and synchronization of the system to the laser for use in the lidar sensor.
Another important issue is market availability combined with wavelength availability for Q-switched solid-state lasers. While in semiconductor lasers the emitting wavelength can be shifted by design, solid-state lasers have fixed atomic transitions and are thus much more limited. These solid-state laser transitions are often located in the near and far-infrared spectral range above one micrometer. Above one micrometer, atmospheric water absorptions increase strongly and further inexpensive state-of-the-art silicon-based detector systems can no longer be used. Conversely, there are comparatively few laser crystals that can be operated at emission wavelengths in the near-infrared spectrum (NIR)

below 1000 nm.

To achieve narrow-band spectral transitions, only rare-earth ions in combination with certain host crystals can be considered. Primarily, various Nd^{3+}-doped host materials operating as quasi-three-level lasers based on Nd^{3+}:YAG at 946nm [31], Nd^{3+}:YVO_4 at 914 nm [32], or Nd^{3+}:$GdVO_4$ at 912 nm [33] have thus been realized in the past. Compared to the classical four-level system typically operating above one micrometer, these quasi-three-level systems are much more difficult to realize. First, for these quasi three-level lasers, the stimulated-emission cross-section is about one order of magnitude smaller, which is the reason why high resonator losses for the undesired four-level transition have to be realized by the cavity coatings. Apart from that, the coating-induced reflectivity for the desired emission wavelength has to be as high as possible, while on the pump facet a high transmission of the pump wavelength has to be ensured. This sets high demands on the optical coating to operate the laser on the desired wavelength as loss-free as possible and thus with maximum efficiency. Another limitation for quasi-three-level systems is reabsorption since the lower laser level also forms the upper ground-state manifold and therefore has a non-negligible thermal occupancy. Finally, for the use in a lidar sensor, these lasers require a compact and robust, if possible monolithic, cavity design without active temperature control.

Concerning the possible amplification materials, it turns out that Nd^{3+}-doped YVO_4 and $GdVO_4$ offer several advantages compared to the popular and commonly used YAG-based host material: i) the stimulated-emission cross-section and the absorption cross-section is larger [34, 35], ii) the isotropy of the YAG host crystal leads to random linear polarization with additional depolarization losses in comparison to YVO_4 and $GdVO_4$ favoring a linear polarisation [36], and iii) the slightly shorter wavelength of the quasi-three-level transition leads to a better quantum efficiency in commercially available silicon detectors [37].

Compared to the CW operation of these quasi-three-level systems [32, 33, 38–40], passive Q-switching possesses further challenges, and hence only a few systems based on Nd^{3+}-doped vanadate crystals have been investigated in the past [41–43].
Therefore, to fully exploit the potential of passively Q-switched solid-state lasers for use in automotive lidar sensors based on silicon detectors, further work and investigations are needed.

The goal of this thesis is the investigation and realization of a passively Q-switched Nd^{3+}:YVO_4 microchip laser at 914 nm for the application in an automotive lidar sensor based on silicon detector technology. In particular, the case of a scanning or rotating lidar system is considered and thus a QCW operation mode with a low duty cycle is selected. In this context, the laser should preferably provide µJ pulse energies and pulse durations in the sub-10 ns range at repetition rates in the double-digit kHz regime. Additional simulations allow a comparison with the underlying theory and an outlook in case of variation of the different system parameters. As a final step, a passively Q-switched laser based on a monolithic resonator setup serves as a demonstrator for future lidar systems and experiments.

In addition to this introduction, the dissertation is divided into the following chapters:

Chapter 2 introduces the relevant fundamentals of laser operation and passive Q-switching of solid-state lasers.

Chapter 3 presents the different simulation methods, which are used in the following chapter to match experimental investigations.

Chapter 4 investigates different system relationships of a passively Q-switched laser considering the requirement for use in an automotive lidar sensor. Additional simulations were performed to provide a theoretical alignment and give a possible outlook on how the system would behave if certain system parameters were varied.

Chapter 5 presents a single-pulse operating passively Q-switched microchip laser design and provides a possible outlook for its use in a lidar system.

Chapter 6 summarizes the results of this thesis and gives an outlook on possible future experiments.

2 BASICS

This chapter summarizes the basics of laser crystals and their energy levels, light-matter interaction, as well as lasers and optical resonators. Furthermore, the fundamentals of passively Q-switched lasers and saturable absorbers for passive Q-switching are discussed.
Unless otherwise stated, the following fundamentals are inspired by various books [44–47].

2.1 LASER CRYSTALS AND ENERGY STRUCTURE

Solid-state lasers consist of an active medium into which laser-active ions are doped, which have the optical transitions at the desired laser wavelength. The host material, in which the active ions are incorporated to a very small percentage, consists of a crystal, glass, or ceramic. The electric field of the host material essentially influences the energy levels of the laser-active ions. In general, a distinction is made between two main groups of laser-active ions, the rare-earth ions, and the transition metal ions.

2.1.1 Rare-earth ions

The rare-earth ions include the atoms with an atomic number from Z = 58 to Z = 71 (Ce, Pr, Nd, Pm, Sm, Eu, Gd, Tb, Dy, Ho, Er, Tm, Yb, Lu). For laser operation, these ions are doped at a low percentage into a suitable host material and are triply ionized. The electronic transitions are usually pure 4f-4f transitions (exception is Ce^{3+} with a 5d-4f transition), which are spectrally very sharp [47]. Due to further outlying 5s and 5p electrons, which do not participate in the laser transition, the 4f electrons are strongly shielded from the electric fields of the host crystal. Here, due to the weak influence of the crystal field, the degenerate energy levels are only weakly split (Stark splitting) and spectrally only slightly shifted compared to the free ions. Thus, the energy levels of the ions in the crystal field are very similar to those of the free ions and the term symbol notation is still valid. Accordingly, the degenerate energy levels in the crystal field are split into 2J+1 sublevels. Here J is the total angular momentum which is the sum of orbital angular momentum L and spin angular momentum S (J = L + S).

As a further consequence of the weak crystal field influence, rare-earth ions have a relatively narrow absorption and emission bandwidth. The narrow absorption bandwidth thus enables very efficient pumping with narrowband laser diodes, while the narrow emission bandwidth enables the realization of single-frequency lasers.

For rare-earth ions, the pump and laser transitions are so-called weakly allowed transitions with a comparatively small oscillator strength.

Weakly allowed transitions are transitions where dipole transitions are excluded by the selection rules. Due to the internal electric and magnetic fields of the crystal, however, symmetry breaking can occur, which makes these transitions possible with a significantly higher probabil-

ity [47]. While for allowed transitions the upper state lifetimes due to spontaneous emission are typically in the range of several nanoseconds, these can be comparatively long for weakly allowed transitions with lifetimes of micro to milliseconds. This, in turn, is an advantage for pulsed lasers, since large pulse energies are possible, as much energy can be stored in the upper level [47]. Furthermore, the lifetime of the upper energy levels is prolonged due to the narrow decay routes.
Compared to transition metal ions, rare earth ions typically have different photon decay routes starting from the upper pump level. Thus, a crystal offers different wavelengths for laser operation, and the desired transition can be selected by losses in the mirror and crystal coatings [44, 45].

2.1.2 Transition metal ions

The transition metal ions include the atoms with an atomic number from Z = 21 to Z = 30 (Sc, Ti, V, Cr, Mn, Fe, Co, Ni, Cu, Zn). When these atoms are doped into a host material, different valence states are formed, which, depending on the substitution site in the host material, occur in divalent, trivalent, or tetravalent form. In these atoms, the 3d orbital is the outermost orbital occupied by electrons and no 4f electrons are present. Consequently, the 3d electrons are not shielded from external electric fields by outer electrons, which leads to a strong shift and a strong splitting of the degenerate energy levels when doped into a host material. The strength of the shift and the splitting depends strongly on the electric field of the host material but also on the local site symmetry. Since the energy levels of the ions deviate significantly from those of the free ions due to the external electric field, a notation according to the term symbol is no longer permissible. The transition metals have absorption and emission bandwidths which are very strongly broadened

due to the strong interaction of the electronic transitions with phonons. For this reason, lasers based on transition metal ions are also called vibronic lasers. Due to the broadband emission, these can be used very well for broadband tunable lasers. The tunability of wavelength is generated by the energy of the laser transition can be continuously partitioned between photons and phonons [44]. On the other hand, broadband absorption offers the use as an absorber for passive Q-switching. The broadband absorption in the visible spectral region gives rise to the observable color of transition metal ion-doped materials.
Compared with rare-earth ions, transition metals have only one suitable transition for laser operation. The lower laser level, from which non-radiative decay processes occur due to phonons, is slightly above the ground state. Therefore, lasers based on transition metal ions are usually quasi-three-level lasers. This means that when these laser crystals are heated, a wavelength shift into the infrared occurs with a narrowing emission bandwidth. Moreover, with increasing temperature, increasingly non-radiative processes, such as cross relaxation, take place in the upper laser levels, limiting the quantum efficiency. For these reasons, efficient cooling is very important for transition metal lasers [45, 47, 48].

2.1.3 Host materials and importance of phonons

There are several requirements when choosing the right host crystal. Basically, the host material should have high transparency for both the pump and laser wavelengths. Good thermal and mechanical properties are also important. These include, of course, good thermal conductivity and a low thermo-optical refractive index. As shown in the previous two chapters, the electric field of the host material also plays a very important role in splitting and shifting the energy levels of the dopant ion. In addition, the emission and absorption cross-section, as well as

the fluorescence lifetime are significantly influenced by the crystal field. Since a lattice atom of the host material is replaced by a laser ion during the doping process, both the size and the valence should be well matched. In addition, the host crystal should have lattice sites where the local electric field has the desired influence on the doped ion in terms of symmetry and strength so that the ion has the necessary spectroscopic properties for the desired laser operation. In general, the ion should have a long radiative lifetime and emission cross-sections in the order of 10^{-20} cm^2 in the host crystal [44].

In addition, a possible directional dependence of the crystal lattice influences the local electric field and thus a preferred direction of light polarization. Thus, isotropic crystals have a symmetric local crystal field and thus no fixed preferred direction for polarization. This does not mean that the light from a doped ion is unpolarized, only that there is no significant preferred direction for polarization. Microscopic crystal differences may nevertheless lead to a preferred polarization, which may not be stable against external influences. For example, thermally induced depolarization can occur in Nd^{3+}:YAG with an isotropic crystal lattice. In comparison, yttrium orthovanadate (YVO_4) is an anisotropic crystal and therefore the crystal field has a certain asymmetry that polarizes the ion and its emission. The natural birefringence of the crystal leads to a preferential direction of polarization compared to Nd^{3+}:YAG [47].

Phonons are the quantized vibration of the crystal lattice. In terms of host materials, they are primarily associated with the removal of heat but have a much more important role in laser operation. When degenerate energy levels are split in the crystal field, phonons enable rapid (on the order of picoseconds) thermalization between sub-levels, forming a Boltzmann distribution within states. This rapid thermalization allows effective transition cross-sections to be used rather than each individual sublevel being attributed its own cross-sections. Experimentally, the

determination of these individual cross-sections would be difficult to implement, since the degenerate levels have the same energy. Besides fast thermalization, multi-phonon transitions are essential for laser operation. These processes lead to the fact that after excitation of the ion with a spectrally broad pump light source, the electron is very quickly in the upper laser level, and thus stimulated emission can take place. The spectral broadness of the pump source excites the electron into one of the upper manifolds. Without phonons, it would be nearly impossible for the electron to relax into the upper pump state. With spontaneous emission, the transition to a lower state with a larger energy difference would be much more likely. A similar problem would also occur after the laser transition, when the ion is in the lower state of the laser transition. Here, rapid thermalization by phonons prevents reabsorption of the laser emission and allows rapid relaxation to the lower pumping level. This allows the ion to participate in further emission processes as quickly as possible again and efficient laser operation is possible [47].

2.1.4 Transitions and selection rules

For free ions, transitions between two energy states are only possible if the selection rules are satisfied. These are summarized for light hydrogen-like atoms for the lowest order of multipole transitions in Table 2.1. The left and middle columns list the selection rules for electric and magnetic dipole transitions, respectively. The right column gives a short note on the respective selection rule.

electric dipole	magnetic dipole	note
$\Delta l = \pm 1$	$\Delta l = 0$	
$\Delta S = 0$	$\Delta S = 0$	spin is preserved
$\Delta L = 0, \pm 1$	$\Delta L = 0$	L = 0 $\rightarrow$ 0 is forbidden
$\Delta J = 0, \pm 1$	$\Delta J = 0, \pm 1$	J = 0 $\rightarrow$ 0 is forbidden

Table 2.1: Selection rules for electric and magnetic dipole transitions of light hydrogen-like atoms.

The probability for such a transition is calculated from the transition matrix element

$$p_{i \rightarrow f} = \langle \psi_f | \mu | \psi_i \rangle \,, \tag{2.1}$$

where $|\psi_i\rangle$ is the initial state, $\langle \psi_f|$ is the final state and μ is the transition moment operator. The transition moment operator distinguishes between electric dipole transition and magnetic dipole transition. Even if an electric dipole transition is forbidden by the selection rule, a magnetic dipole transition can take place in the state. However, compared to electric dipole transitions, magnetic dipole transitions are about five orders of magnitude weaker [49].

If the selection rules are violated, the transition matrix element is 0 and this transition is called dipole forbidden or weakly allowed. This means that although the transition is not possible by dipole radiation, it may be allowed by other mechanisms such as multipole radiation (quadrupole or octupole). The electric and magnetic crystal fields can lead to symmetry breaking so that a forbidden dipole transition becomes possible by mixing states of different parity. However, the transition probability is significantly lower compared to dipole transitions. Here, the parity describes the symmetry of the wave function concerning reflection and can take the values +1 and -1. It is important to mention that the selection rules for multipole radiation differ from the rules shown in Table 2.1 [46, 47].

2.2 LASERS AND OPTICAL RESONATORS

A laser generally consists of a gain medium and an optical resonator. Depending on the laser medium used, or the interaction between the gain medium and the resonator, different numbers of energy levels of the gain crystal are involved in the laser operation. A basic distinction is made between four-level and three- or quasi-three-level systems. In this section, the basics of the quasi-three-level system, optical resonators and modes, and thermal effects will be discussed.

2.2.1 Three-level lasers

In addition to four-level lasers, quasi-three-level lasers are widely used as bulk solid-state or fiber lasers. Pure three-level lasers are used more rarely and have considerable disadvantages compared to four-level and quasi-three-level lasers. Figure 2.1 shows the idealized energy levels of a three-level laser on the left, a four-level laser in the middle, and a quasi-three-level laser on the right.
The first laser was built in 1960 and was a **three-level laser** based on a Ruby crystal
(Cr^{3+}:Al_2O_3). The left side of Figure 2.1 shows a pure three-level laser. Here the lower laser level (1) is also the ground state. The laser threshold is comparatively high since a population inversion can only be achieved when more than half of the ions are in an excited state (2), or state (3), respectively. In this case, the transition τ_{23} is very fast (on the order of picoseconds) and prevents excited ions from being de-excited by stimulated emission due to pump photons.

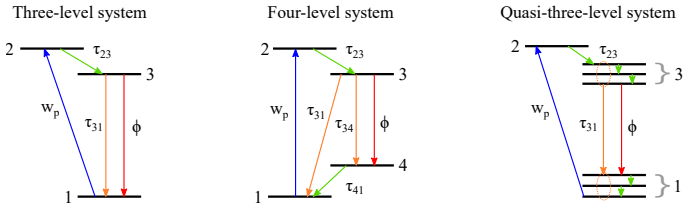

Figure 2.1: Simplified view of the energy levels of different laser systems. The pump transition is shown in blue, while non-radiative phonon transitions are shown in green. In addition, orange and red arrows correspond to transitions by spontaneous emission and stimulated emission, respectively.

Compared to the three-level laser, **four-level lasers** have a lower threshold because the lower laser level (2) is not the ground state (1) and is depopulated very quickly by multi-phonon transitions. As a result, the achievable population inversion is larger and there is also negligible reabsorption of the laser light. The best known solid-state laser is a four-level Nd^{3+}:YAG laser operating at 1064 nm.

The right schematic in Figure 2.1 is a **quasi-three level system**. An example of such a system is the ${}^4F_{3/2} \rightarrow {}^4I_{9/2}$ operation of a Nd^{3+}:YAG laser emitting at 946 nm. In comparison to a four-level laser, the lower laser level is the upper Stark multiplet of the ground state manifold and therefore only a few $100\,cm^{-1}$ above the ground state multiplet. Due to this, the lower laser level has a high thermal occupancy in thermal equilibrium at room temperature ($kT \sim 207\,cm^{-1}$ at 300 K). Comparatively, in a typical four-level system the lower laser level is thermally nearly unoccupied because it is about $10 \cdot kT$ above the ground state at room temperature (300 K).

Due to the thermal occupation of the Stark manifolds, the population inversion becomes smaller and **reabsorption processes** take place, which indirectly reduces the laser efficiency and increases the laser threshold. However, reabsorption is not equivalent to an actual energy loss, since the absorbed photon is not lost, but re-excites the ion, which can then

contribute to the laser operation again by stimulated emission. However, a higher excitation level is required due to reabsorption and the associated increased threshold, so additional losses are incurred due to spontaneous emission. In addition, for longitudinally pumped lasers, a trade-off must be made between pump absorption efficiency and reabsorption losses due to the process of reabsorption. If the complete pump power shall be absorbed, the laser crystal has to be chosen accordingly long or has to be highly doped. The longer or higher doped laser crystal increases the reabsorption while at the weakly pumped end of the crystal comparatively little pump light is absorbed. Therefore, to optimize the system for maximum conversion efficiency, a trade-off between pump efficiency and reabsorption has to be made. Another consequence of the higher excitation level is that quasi-three level lasers require more pump power, which in turn can lead to further thermal effects. Due to the temperature-dependent refractive index, the thermal lensing is increased and the additional heat input causes a reduction of the effective laser cross-sections. While pump saturation is usually not an issue for four-level lasers, it should not be disregarded especially for passively Q-switched quasi three-level lasers with small pump spots. The Q-switching initially increases the threshold value and the gain medium is pumped significantly longer compared to CW operation.

For a quasi-three level laser, the laser threshold in CW mode is

$$P_{th} = \frac{\pi h\nu_p}{4\sigma_g \tau (f_a + f_b)} (\omega_p^2 + \omega_l^2)[2 f_a \sigma_g N_g L_g + \ln(R)], \tag{2.2}$$

where $h\nu_p$ is the pump photon energy, σ_g is the stimulated emission effective cross-section, τ is the fluorescence lifetime, and f_a and f_b are the relative occupation densities in the lower and upper Stark manifolds, respectively [50]. Furthermore, ω_p and ω_l are the radii of the pump and resonator modes, N_g is the doping of the gain medium, L_g is the length

of the gain medium, and R is the resonator internal losses including the output coupler mirror (OCM) and other parasitic losses.
The equation consists of two parts that contribute descriptively to the threshold value. The first part $\propto 2 f_a \sigma_g N_g L_g$ is the pump power required to achieve a population inversion. This corresponds to the round-trip absorption of the laser wavelength and is therefore also called the reabsorption loss. The second part $\propto \ln(R)$ is the pump power required to compensate for the cavity round-trip losses due to the OCM and other parasitic losses.
To minimize the threshold, both a small pump and resonator mode should be chosen with the length of the gain medium being as short as possible. These two conditions speak for the use of laser diodes as pump lasers since they can be focused on a much smaller pump volume ($\sim$ pump mode $\times$ length of the gain medium) compared to flash lamps.

The saturation fluence of the laser crystal is an important parameter, especially for passive Q-switching (see the following subsection). It has a significant influence on the achievable pulse energy and the repetition rate of the laser. If a pulse with the fluence F_{pulse} (unit energy density) propagates through the laser crystal, it is amplified and reduces the gain in the crystal. The saturation fluence of the gain material is defined as

$$F_{sat} = \frac{h\nu}{\sigma_g + \sigma_{reab}}, \tag{2.3}$$

and reduces the gain by $1/\mathrm{e}$ ($\sim 37\,\%$). Hereby, σ_{reab} is the effective reabsorption cross-sections of the gain medium. From the saturation fluence along with the mode area A, the saturation energy can be calculated as

$$E_{sat} = A \cdot F_{sat} = A \cdot \frac{h\nu}{\sigma_g + \sigma_{reab}}. \tag{2.4}$$

This is often more practical for design and optimization since the laser mode area is known or can be measured. In the three-level system, the effective reabsorption cross-section σ_{reab} of the laser wavelength is taken into account, which is omitted in the case of a four-level system.

2.2.2 Optical resonators and modes

Optical resonators are an essential part of lasers since they provide optical feedback to the gain medium and thus amplify the stimulated emission. The resonator determines the mode structure in the transverse and longitudinal direction as eigensolutions of the electric field.

Transversal modes, as the name implies, have a field distribution perpendicular to the direction of propagation in the resonator. The transverse modes are so-called eigenmodes of the resonator, which means that the field distribution, apart from diffraction losses, must be in the initial state after one resonator round trip. The transverse modes have a major influence on the beam divergence and the beam diameter of the laser.
Mathematically, the transverse modes can be described either by Hermite polynomials (in cartesian coordinates) or Laguerre polynomials (in cylindrical coordinates), dependent on the choice of coordinate system. The overlap between resonator mode and the mode diameter of the pump laser has significant influence on the transverse operation modes of the laser. By choosing a pump spot that is too large, higher transverse modes can resonate, while with a pump spot that is too small, the conversion efficiency of the laser may deteriorate.

A laser operating in the fundamental transverse mode has a beam with a Gaussian intensity profile, which is also called a **Gaussian beam**. The

name follows from the shape of the transverse intensity profile, which can be written mathematically as

$$I(r,z) = \frac{P}{\pi w(z)^2/2} \exp\left(-2\frac{r^2}{w(z)^2}\right), \tag{2.5}$$

where r is the distance from the optical axis, z is the position of the propagation direction of the beam, P is the optical power, and $w(z)$ is the beam radius. Although the intensity distribution maintains a Gaussian profile for all propagation positions z, the beam radius $w(z)$ changes as a function of the axis position z and thus the width of the intensity distribution. The beam radius $w(z)$ of a Gaussian beam as a function of propagation z is described by a hyperbolic form

$$w(z) = w_0\sqrt{\left(1+\frac{z}{z_R}\right)^2} \tag{2.6}$$

with the minimum beam diameter $2 \cdot w_0$ and the Rayleigh length

$$z_R = \frac{\pi w_0^2}{\lambda}, \tag{2.7}$$

where λ is the wavelength of the laser. The Rayleigh length is defined as the distance from the minimum beam diameter at which the beam area has doubled ($w(z_R) = \sqrt{2}w_0$). Alternatively, the confocal parameter b is often defined as $b = 2z_R$. In this range, the beam is assumed to be collimated. Figure 2.2 shows schematically the hyperbolic shape of a Gaussian beam around the position of the focus. The Gaussian intensity profile extends to infinity, but the intensity for diameter $2w_0$ has already dropped to $1/e^2$ (13.5 %), which is indicated by the red envelope. In the far-field, the hyperbolic shape can be approximated by a linear divergence angle, resulting in

$$\theta = \lim_{z\to\infty} a_n \frac{2w(z)}{z} = \frac{2\lambda}{\pi w_0}. \tag{2.8}$$

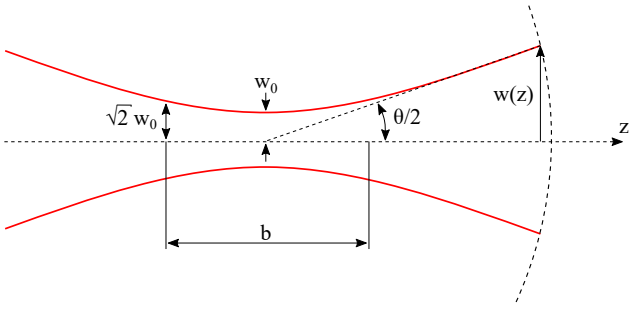

Figure 2.2: Spatial propagation of a Gaussian beam along the z-axis. Different parameters characterizing the beam are indicated by the black arrows.

This means that the beam radius $w(z)$ and the divergence angle θ increase linearly in the far-field. By rearranging Equation 2.8, it can be seen that the product of beam radius w_0 and divergence angle θ is constant and equals λ/π. The constant product implies that as the beam radius becomes smaller, the divergence angle increases and vice versa. The product of the two quantities is defined as beam parameter product (BPP) and used as a measure to determine beam quality.

A Gaussian beam has the smallest possible BPP and therefore the highest possible beam quality, causing it to be called diffraction-limited. Beams with a larger BPP can also be described by Gaussian beams considering the beam quality factor M^2. While the fundamental mode of the resonator has an $M^2 = 1$, higher transverse modes have an $M^2 > 1$. The larger the M^2, the more higher modes are present, and the larger the minimum focusable diameter becomes. The factor M^2 results from the quotient of the measured BPP and the minimum possible diffraction-limited BPP and is a measure of how well the laser can be

focused or collimated. Taking into account the beam quality factor M^2 and the Rayleigh length the beam radius $w(z)$ finally changes to

$$w(z) = w_0 \sqrt{\left(1 + \frac{M^2 \lambda z}{\pi w_0^2}\right)^2}. \tag{2.9}$$

When propagating through lenses and crystals, Gaussian beams maintain their Gaussian intensity profile and beam quality, whereas only the associated beam parameters w_0 and θ change. However, this assumption is valid only under consideration of the paraxial approximation, which loses validity for large divergence angles.

In a linear resonator, a standing wave is formed analogously to a Fabry-Pérot etalon. The constructively interfering waves with frequency ν are called **longitudinal modes** and follow the resonance condition

$$\nu = q \frac{c}{2L_{opt}}. \tag{2.10}$$

Here q is the order of the longitudinal mode, c is the speed of light, and L_{opt} is the optical resonator length. From this condition follows an equidistant frequency spacing $\Delta\nu = c/(2L_{opt})$ between adjacent frequencies which in the wavelength space becomes

$$\Delta\lambda = \frac{\lambda^2}{2L_{opt}}, \tag{2.11}$$

where λ is the wavelength of the propagating light. For an exemplary Nd^{3+}:YAG laser at 1064 nm with a compact resonator having an optical length of 20 cm, this results in a longitudinal mode spacing of about 28 pm. Of course, the number of laser modes does not only depend on the resonator but is also determined by the gain medium, since only modes which are located within the gain bandwidth are amplified. For a rough estimate, the number of longitudinal modes can be calculated

from the ratio of the gain bandwidth and the mode spacing. For the above resonator, in the case of Nd^{3+}:YAG with a gain bandwidth of 0.6 nm, the laser operates on an estimated number of 21 modes. Simply put, if the resonator is shortened, the number of longitudinal modes is reduced, and theoretically, a single-frequency laser can be generated which operates on a single longitudinal mode.

2.2.3 Thermal effects

The pumping process and operation of a solid-state laser leads to a heat contribution in the gain medium, which has a great influence on the performance and stability of the laser. The heat input and associated thermal effects reduce the maximum achievable output power, as well as the beam quality, and in the worst-case lead to breakage of the laser crystal. There are various causes and effects of heat input. These are partly based on the intrinsic properties of the materials used but can be minimized by system optimization. The quantum defect is the energy difference of the pump photon to that of the emitted laser photon and has a significant contribution to the heat due to non-radiative phonon transitions. Depending on the crystal, laser transition, and pump laser used, this value varies. As an example, the quantum defect for an 808 nm pumped Nd^{3+}:YVO_4 laser is 11.6 % when the laser is operated at 914 nm. This means that at 10 W of continuous pump power, more than one watt of the heat already accumulates in the crystal and has to be dissipated. When pumping at 880 nm, the quantum defect is only 3.7 %, but the absorption cross-section is also much smaller so that a longer crystal or higher doping must be selected, which can lead to further effects. Moreover, the pump spot diameter should be chosen to match the resonator mode, otherwise, regions in the gain crystal will be pumped, leading either to higher transverse modes or

an additional heat contribution by fluorescence. With a good overlap between pump laser mode and resonator mode, the contribution of fluorescence during laser operation in saturation can be neglected, since the contribution by stimulated emission is usually much larger than the spontaneous emission and thus relatively few ions are excited by fluorescence. Concerning deposited heat, the use of diode-pumped lasers is also advantageous compared to flash-lamp pumped lasers. Due to the relatively narrow spectral width of pump diodes, the pump transition of the crystal can be well-targeted. In contrast, the wide pump spectrum of flash lamps leads to background absorption by the host material and impurity atoms.

In longitudinally pumped solid-state lasers, the heat introduced by the pumping process leads to a temperature gradient in the laser crystal. The crystal is typically actively cooled via the side faces, where thermal bonding can be improved by inserting an indium foil between the crystal and the crystal holder. The end faces of the crystal, on the other hand, are passively cooled by ambient air, resulting in an inhomogeneous and non-uniform temperature profile in the crystal. The resulting temperature gradient leads in the crystal in radial direction and along the optical axis finally to an optical path difference (OPD) and consequently to a thermal lens with a focal length of

$$f = \frac{KA}{P_{heat}} \left[\frac{1}{2} \frac{dn}{dT} + \alpha_{th} C_r n^3 + \frac{\alpha_{th} r_0 (n-1)}{l} \right]^{-1} \tag{2.12}$$

with

$$P_{heat} = \eta \cdot P_{pump}. \tag{2.13}$$

Here, K is the thermal conductivity, A is the cross-sectional area of the pump spot, P_{heat} is the heat dissipated in the crystal, η is the pump absorption efficiency, P_{pump} is the applied pump power, dn/dT is the temperature-dependent refractive index change, a_{th} is the thermal expansion coefficient, C_r is the photoelastic coefficient, n is the refractive

index, r_0 is the radius of the crystal, and l is the crystal length [44].

Equation 2.12 consists of three different parts which are related to the temperature and stress-dependent change of the refractive index and distortion and the end-face curvature of the crystal. Due to the different temperature gradients in the radial and axial direction, a refractive index difference dn/dT arises which leads to a thermal lens. Dependent on the gain crystal and the associated refractive index variation, the modification can have a positive or negative sign and the resulting lens is either convex or concave. In addition to this, the thermal gradient leads to non-uniform crystal expansion, which creates mechanical stress in the crystal lattice and thus also contributes to an inhomogeneous refractive index change dn/dr. Furthermore, the thermal expansion of the crystal can lead to bulging of the planar end faces of the crystal and thus a lensing effect. At the pumped end face of the crystal, the temperature gradient and the resulting thermal lensing are most pronounced. The exponential absorption of pump light along the optical axis results in an exponentially decaying temperature profile. In the radial direction, the cooled side surfaces lead to strong heat dissipation and a strong temperature gradient. In the radial direction, the cooled side surfaces lead to a strong logarithmic decrease in the temperature. Overall, the contribution of the temperature-dependent refractive index variation is dominant concerning the induced thermal lensing. For instance, experiments with a Nd^{3+}:YAG laser showed at higher pump power levels that a comparatively small contribution of 20 % for the stress-dependent variation of the refractive index, while the temperature-dependent expansion had hardly any influence at less than 6 % [51]. For this reason, especially for low pump powers, the bulging effect of the crystal end faces, the stress-induced influence of the refractive index, and the

temperature-dependent crystal expansion can be neglected, reducing Equation 2.12 to

$$f = \frac{K\pi\omega_p^2}{\eta P_{pump}(dn/dT)} \left(\frac{1}{1 - \exp(-\alpha_{th} l)} \right). \tag{2.14}$$

In general, the thermal lens deteriorates the beam quality and negatively affects the resonator stability as a function of pump power. In the case of plane-parallel an resonators, however, some thermal lensing is quite desirable and essential to stabilize the resonator, which is otherwise operated at its stability limit.

In principle, even a strong thermal lens can be compensated by adjusting the laser design for a specific operating point. Especially for high output powers and correspondingly high intracavity powers, a slight deviation of the power can have a large impact on the stability of the laser and stop the laser operation or cause crystal fracture. Further, a strong thermal lens inevitably leads to strong aberrations, making high beam quality difficult to achieve. As an example, Figure 2.3 shows the resulting thermal lens for a Nd^{3+}:YVO_4 crystal according to Equation 2.14 as a function of the applied pump power and the assumption that 24 % of the pump power is converted to heat [52]. In addition, a crys-

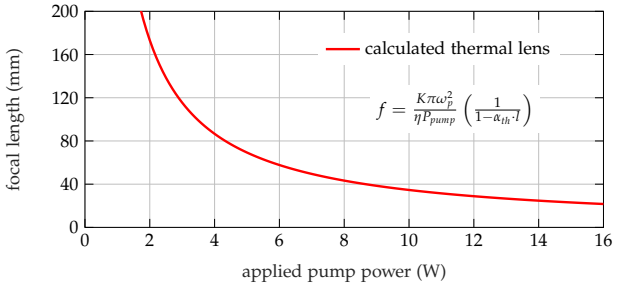

Figure 2.3: Calculated thermal lens of a Nd^{3+}:YVO_4 crystal as a function of applied pump power.

tal of 3x3x5 mm^3 and a Gaussian pumping distribution with a diameter of 400 µm was assumed. For the material-dependent constants, K = 5.1 $W\,m^{-1}\,K^{-1}$, $dn/dt = 8.5 \times 10^{-6}\,K^{-1}$ and a_{th} = 5.32 cm^{-1} were assumed [53].

2.3 PASSIVE Q-SWITCHING

Passive Q-switching is a technique to obtaining laser pulses in the nano- and sub-nanosecond regime. The principle of Q-switching is that high cavity losses are introduced while continuous pumping enables high storage of energy without laser operation. Sudden reduction of internal losses results in an intense laser pulse as a significant amount of stored energy is extracted. For passive Q-switching, the temporary cavity losses are attributed to a passive element like a saturable absorber.

2.3.1 General operation principle

The dynamics of a passively Q-switched operation are shown in Figure 2.4. Hereby, the evolution of the gain coefficient is shown in blue, the saturable absorber losses in green, and the generated photon density in the form of a laser pulse in red. Initially, the population inversion, which is proportional to the gain coefficient, is increased via the external pumping process and the laser operation is suppressed due to the high losses of the saturable absorber. Consequently, the population inversion reaches a level that is far above the natural laser threshold without the saturable absorber. The maximum energy stored in the gain crystal is limited by the process of spontaneous emission or by

too low losses of the saturable absorber. If now suddenly the losses generated by the saturable absorber are reduced, an electric field in the resonator builds up exponentially from spontaneous emission. The gain decreases simultaneously and gets saturated once the saturation fluence of the gain medium is reached. Further, when the gain reaches the remaining resonator losses (equal to the threshold inversion) the maximum photon density is reached. As the change of inversion is negative and further the intracavity power is high, the population inversion still decreases until a final population density is reached. The passive Q-switching element is increasing intracavity losses once the intracavity photon density decreases. Usually, the Q-switching element should recovery quicker than the gain material to obtain stable pulse operation. For continuously pump lasers, the population inversion increases again above threshold inversion, and the whole process repeats.
In comparison to active Q-switching, passive Q-switching [44, 47] requires no active elements such as an electro-optic or acusto-optic driver as well as a RF signal generator. Therefore a simple and cost-effective system is possible which can be additionally quite compact and robust. In addition, high voltages can lead to electromagnetic compatibility

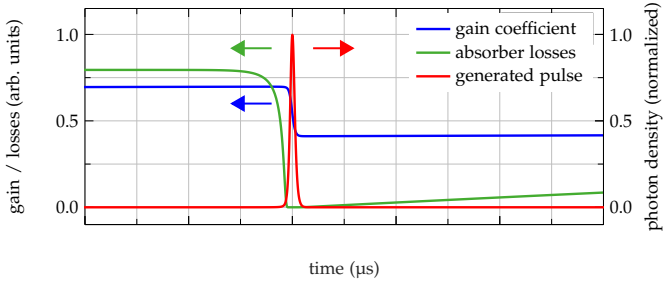

Figure 2.4: Dynamics of a passively Q-switched laser showing the time evolution of the gain coefficient (blue), the saturable absorber losses (green) and the generated photon density in the form of a laser pulse (red).

problems with other components and are also potentially dangerous from a work point of view. Another advantage of passively Q-switched lasers is the possibility of generating very high repetition rates whereas actively Q-switching is somehow more limited due to a maximum required switching time. In contrast, passively Q-switched lasers show temporal pulse-to-pulse fluctuations as the laser dynamics determine the time when the pulse is triggered. For example, even small variations in pump energy or ambient conditions can lead to significant temporal jitter. Further, the lower laser output is achieved in general due to residual absorption in form of non-saturable losses of the Q-switching element.

2.3.2 Features and properties of passively Q-switched laser

In the following, important features and properties will now be introduced and discussed in the context of passively Q-switched lasers concerning the later experiments.

For passively Q-switched lasers with short resonators the **pulse build-up time** is in the regime of 1 µs as the number of round-trips in the resonator is approximately 1000 once the saturable absorber is switched. In contrast for active Q-switching, pulse formation takes place within several tens of round trips and therefore the pulse build-up time is an order of magnitude smaller. In passively Q-switched lasers with saturable absorbers, the switching process is triggered by the first built-up longitudinal mode. Compared to other modes starting later, this mode already consists of a certain photon density. As soon as the second and other modes reach the threshold, the first mode has already grown significantly due to the highest gain. As a result, the first longitudinal mode usually differs from other modes by more than one order of magnitude,

and single-frequency operation is easier [54, 55]. Furthermore, the longitudinal mode spacing can be increased by shortening the resonator. Due to the relatively narrow gain-bandwidth of rare-earth-doped crystals, modes can be selected by placing them outside the gain. Another possibility to achieve single-frequency operation is the insertion of a frequency-selective element, e.g. a thin Fabri-Pérot etalon in the form of an undoped crystal. Due to the long pulse build-up time, many resonator cycles are covered and frequencies that are not resonant at the etalon are suppressed [56].

Passively Q-switched lasers possess **pulse duration** in the nanosecond and sub-nanosecond regime dependent on the utilized gain material, saturable absorber, output coupler reflectivity and internal cavity losses. Usually, it takes several round trips until the exponentially growing photon flux extracts the stored energy. A reasonable estimate for the pulse duration in the case of a Q-switching element with strong saturation is

$$\tau_p \sim 4.6 \frac{T_{\text{round}}}{q_0}, \tag{2.15}$$

where q_0 ($\sim$ 1 - T_0) is the saturable loss and T_0 the initial transmission of the Q-switching element. Further, T_{round} is the resonator round trip time which is again linearly dependent on the resonator length. Thus, the easiest way to change pulse duration is done by adjustment of the resonator length whereas a change of the saturable losses typically affects the general laser dynamics [47].

The **pulse energy** of passively Q-switched lasers typically ranges from sub-micro joule up to a few milli-joules dependent on the pulse repetition rate and design specification. Analytically, the pulse energy of a passively Q-switched laser can be derived as

$$E_p = \frac{h\nu A}{2\sigma\gamma} \ln\left(\frac{1}{R}\right) \ln\left(\frac{n_i}{n_f}\right), \tag{2.16}$$

with the laser photon energy $h\nu$, effective beam cross-section area A, stimulated-emission cross-section σ, inversion reduction factor γ, and output coupler reflectivity R [57]. Large pulse energies are obtained for a big mode-area which can be realized by a large pump spot but this usually results in higher-order transversal modes and an increase of laser threshold. Further, a small stimulated-emission cross-section and an output coupler mirror with low reflection are favorable. Moreover, the ratio n_i/n_f is directly related to the saturable losses of the element. This means that large pulse energies can be achieved more easily if the saturable losses are low which again increases the pump laser threshold. It should be noted that high pulse energies are always a trade-off and typically reduced the repetition rate. For pump power levels well above threshold pump power, the **repetition rate** is approximated by

$$f_{rep} \sim \left[\tau \ln\left(\frac{P_{th}/P}{P_{th}/P-1}\right)\right]^{-1}, \tag{2.17}$$

with gain medium fluorescence lifetime τ, pump power threshold P_{th}, and applied pump power P [58]. In the case of a low-power system using a saturable absorber for passive Q-switching the maximum achievable repetition rate is limited by the recovery time of the absorber. For high repetition rates, the time between adjacent pulses approaches a regime where the saturable absorber is not able to fully recover after a pulse is generated. In that case, unstable laser dynamics dominate and disturb steady laser operation. In contrast, for high-power lasers, the maximum achievable repetition rate is typically restricted due to thermal effects at higher pump powers [56].

With **satellite pulses**, the actual laser pulse is followed by a second pulse which is delayed in time concerning the main pulse and which has a smaller pulse amplitude. The interval between the two pulses is of the order of nanoseconds and is thus significantly smaller than the

actual pulse interval at repetition rates in the kilohertz range. In general, the occurrence of satellite pulses can have two reasons:

① When the first longitudinal mode has built up in the form of a laser pulse, the remaining gain can be sufficiently high that a second adjacent longitudinal mode and thus a second laser pulse builds up. However, this requires that the remaining gain is above the threshold and the difference in build-up time between the two modes is not too large. Since the gain is already significantly reduced by the build-up of the first pulse, the second pulse has considerably smaller pulse energy and thus a longer pulse duration. When the satellite pulses are generated by this effect, the laser runs on two different longitudinal modes. In this case, satellite pulses can be suppressed if there is a large gain difference between the main mode and competing mode. For this purpose, the mode spacing should be as large as possible (short resonator length) and the main mode should be as close as possible to the maximum of the gain curve (tuning via temperature or pump power). A good rule of thumb is: The closer the main mode is tuned to the maximum of the gain curve, the greater the delay between main and satellite pulse and the smaller the amplitude of the satellite pulse [59].

② It has been shown that satellite pulses can occur if the photon lifetime in the resonator is significantly smaller than the thermalization time in the degenerate Stark submanifolds of the lower laser level. Once a laser pulse is generated, the remaining population in the upper laser level can lead to a new population inversion if a delayed depopulation by thermalization occurs in the Stark sublevels of the lower laser level. If the new population inversion is larger than the threshold value of another longitudinal mode, a satellite pulse is generated. Since the gain has already been significantly reduced by the main pulse, the satellite pulse has a significantly smaller amplitude [59]. In this case, the satellite

pulse is generated similar to the gain-switching of pulsed lasers. Compared to the upper possibility of satellite pulse generation, both pulses are usually in the same longitudinal mode. In addition, the two pulses can have a very stable delay and amplitudes.

Depending on which gain material is used, the thermalization time varies in the Stark multiplets and satellite pulses may occur. For example, while Nd^{3+}:YAG has a very short lifetime of about 225 ps in the lower Stark multiplet, Nd^{3+}:$GdVO_4$ or Nd^{3+}:YVO_4 has around 20 ns. For resonator lengths of a few millimeters, the photon cavity decay time is on the order of nanoseconds and satellite pulses have been observed at Nd^{3+}:$GdVO_4$ [60].

Figure 2.5 shows an exemplary satellite pulse based on rate equation simulations. Here, the origin of the satellite pulse is based on possibility ②, where the thermalization time in the Stark submanifolds was reduced in the model to be shorter than the photon lifetime in the resonator. The generated main pulse with a pulse duration of 18.9 ns (FWHM) is followed by a satellite pulse with a pulse duration of 108.2 ns separated by 219 ns. For passively Q-switched lasers, the exact timing for laser pulses is determined by the laser system dynamics. By pump-

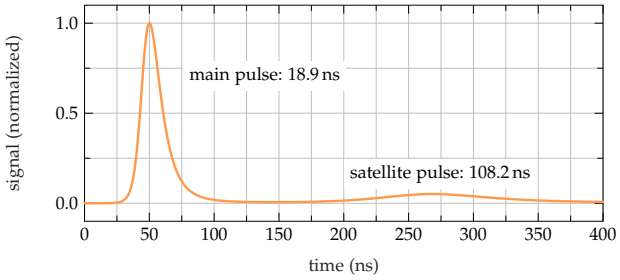

Figure 2.5: Exemplary satellite pulse based on rate equation simulations. The generated main pulse with a pulse duration of 18.9 ns (FWHM) is followed by a satellite pulse with a pulse duration of 108.2 ns separated by 219 ns.

ing, a population inversion builds up in the laser crystal and a pulse is triggered as soon as a longitudinal mode builds up from spontaneous emission which is strong enough to switch through the saturable absorber.

Due to the dynamic process, various factors can influence the exact switching time of the saturable absorber and thus generate a **temporal jitter** between successive laser pulses. Typical temporal jitter is on the order of the pulse duration or even larger. Starting with the pump laser, small fluctuations in the pump power, a slight drift of the pump wavelength but also temperature-induced changes in the polarization can disturb the dynamics of the laser. Furthermore, temperature influences at the laser crystal and saturable absorber but also mechanical vibrations are added as disturbance of the laser dynamics. While the exact switching time of passively Q-switched lasers is influenced by these disturbances, the pulse energy, and pulse duration remain largely unaffected [61].

In principle, temporal jitter is an inherent property of passively Q-switched lasers, but there are several ways to reduce it. At low repetition rates, the pump power can be modulated and pulsed. In this case, the solid-state laser can be pumped continuously just below the laser threshold and pulses are generated by briefly raising the pump power until a single pulse is formed. The maximum switching speed of the pump laser but also the overall efficiency is limited with this method [62]. Furthermore, injection seeding can be used to reduce the pulse build-up time and to synchronize the wavelength of the seed laser and the passively Q-switched laser. However, this method requires very good temperature stability of the whole system and makes the laser setup larger and more complex [63]. In addition to this, there is also the possibility of bleaching the saturable absorber with another pulsed laser. In this case, however, the laser that bleaches the absorber must have a significantly better timing jitter than the laser that is passively

Q-switched. In addition, the setup is of course also significantly more complex and expensive than the single passively Q-switched laser [64].

2.4 SATURABLE ABSORBERS FOR PASSIVE Q-SWITCHING

Saturable absorbers have a nonlinear absorption behavior, which can be used for a sudden reduction of the resonator losses and thus for the generation of short laser pulses. The nonlinear absorption behavior of the absorber can be generated here by saturating a spectral transition for high intensities.

There are **different types of saturable absorbers** for passive Q-switching which are predominantly based on transition metals ion-doped crystals or glasses. Probably the most commonly used saturable absorber material is a chromium-doped yttrium aluminum garnet crystal (Cr^{4+}:YAG). These absorbers have broadband absorption, as well as good chemical, thermal, and mechanical properties.

Furthermore, semiconductor saturable absorber mirrors (SESAMs) are interesting for passive Q-switching, but due to a very low damage threshold, they are preferably used for passive mode-locking to generate ultrashort pulses. A major advantage of SESAMs is that they can be specially designed and optimized for specific wavelengths. In addition, compared to crystalline absorbers doped with transition metal ions, they increase the resonator length only insignificantly, which in principle can also lead to shorter pulses. However, due to the relatively low damage threshold and a short recovery time, SESAMs are preferred for applications with low pulse energy and high repetition rates. Another important point is that SESAMs act as end mirrors by their design, therefore an additional output coupler mirror must be used which often makes the system design larger and more complex. Much rarer are ex-

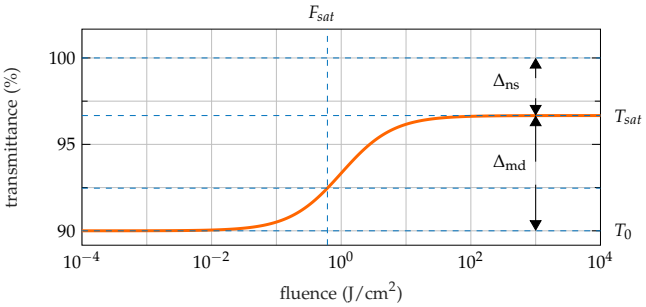

Figure 2.6: Characteristic switching behavior of the transmission of a saturable absorber for increasing fluences on the absorber.

otic saturable absorbers based on quantum dots, organic dye solutions, color centers, or even graphene layers. Since the absorbers used in this work are based on transition metal ion-doped crystals, these absorbers will be the main focus of the following subsection.

Figure 2.6 shows the characteristic switching behavior of the transmission as a function of the fluence of a saturable absorber. The **initial transmission** T_0 is the transmission of the absorber for small signals or fluence. For an absorber of thickness l with absorption coefficient, this results in

$$T_0 = \exp(-\alpha l) = \exp(-N_{gs}\sigma_{GSA} l), \tag{2.18}$$

where the absorption coefficient for small signals without the contribution of ESA can be calculated to $\alpha = N_{gs}\sigma_{GSA}$. Here, N_{gs} is the occupation density in the ground state of the absorber and σ_{GSA} is the ground-state absorption (GSA) cross-section. The initial transmittance of an absorber can be determined relatively easily and, along with the thickness, is an important parameter in the design of a laser.

The **saturation fluence** F_{sat} is the energy per area needed to increase

the initial transmission value by $1/e$ ($\sim 37\,\%$). It is expressed as

$$F_{\text{sat}} = \frac{h\nu}{\sigma_{\text{GSA}}}, \tag{2.19}$$

and thus the ratio of photon energy and GSA. Here, non-saturable excited-state processes are neglected. It is important to note that the saturation fluence usually does not depend on the thickness of the saturable absorber if the absorber is not too thick to change the fluence as a function of penetration depth. Likewise, the saturation fluence does not take into account the mode area on the absorber. The mode area is taken into account by the **saturation energy** which is the product of saturation fluence and mode area. The maximum achievable transmission of a saturable absorber is the **saturation transmission** T_{sat}. The maximum transmission is only 100 % in the ideal case and is reduced by the **non-saturable losses** Δ_{ns}. These losses can be generated in ion-doped insulator saturable absorbers by ESA. In this process, the already excited ion is further excited to an even higher electronic state by the absorption of light. The strength of the ESA is characterized by the **excited-state absorption cross-section** σ_{ESA}. In passive Q-switching, non-saturable losses are undesirable because they do not contribute to the switching behavior, but reduce the achievable pulse energy and conversion efficiency of the laser while increasing the system threshold. ESA is a problem especially for broadband absorbing media such as transition metal ion-doped absorbers and does not play a major role for rare-earth-doped materials. While GSA leads to a higher absorber transmission with increasing fluence, ESA behaves in exactly the opposite way. While GSA leads to higher absorber transmission with increasing fluence, ESA behaves in exactly the opposite way. Absorption by ESA rises with increasing fluence as the excited state becomes more populated. For saturable absorbers which are used for passive Q-switching, the influence of GSA must be dominant. More precisely, $\sigma_{\text{GSA}} > \sigma_{\text{ESA}}$ must hold. Ab-

sorbers, where the ESA is dominant compared to the GSA, are called reverse saturable absorbers [65]. These absorbers cannot be used for passive Q-switching but can be used, for example, for self-stabilization of passively mode-locked lasers since the total transmission decreases with increasing absorber fluence [66]. A good measure to judge the absorber quality is the ratio of both cross-sections. This ratio is called figure of merit (*FOM*) and is defined as

$$FOM = \frac{\sigma_{\mathrm{GSA}}}{\sigma_{\mathrm{ESA}}}, \tag{2.20}$$

[67]. In general, however, the higher the FOM, the better the saturable absorber is suited for passive Q-switching. Similar to the stimulated-emission cross-section of the gain material, the GSA and ESA cross-sections depend on the wavelength.

The modulation depth Δ_{md} of a saturable absorber is the difference between the maximum and minimum transmittance. This value is largely determined by the initial transmission and non-saturable losses of the absorber. In passive Q-switching, the modulation depth has a great influence on the pulse energy and thus also on the pulse duration. To generate high-energy pulses at a lower repetition rate, a large modulation depth is required. In addition, it is also important that the saturation energy in the gain medium, i.e. the maximum storable energy, is large. Similar to the saturable absorber, the saturation energy is the product of saturation fluence and mode area. Therefore, for large pulse energies, a small stimulated-emission cross-section and the largest possible mode area in the gain medium are important. Conversely, high repetition rates with smaller pulse energies can be achieved more easily if the stimulated-emission cross-section is large and the mode area in the gain crystal is rather low.

The **saturation intensity** I_{sat} (power per area) becomes important for saturable absorbers only if the recovery time is in the order of magnitude of the passively Q-switched pulse duration since then the sat-

urable absorber already recovers during the pulse build-up time. The saturation intensity is defined as

$$I_{\text{sat}} = \frac{h\nu}{\sigma_{\text{GSA}}\tau} = \frac{F_{\text{sat}}}{\tau} \tag{2.21}$$

where F_{sat} is the saturation fluence and τ is the recovery time of the absorber.

The **recovery time** τ of a saturable absorber is the time until the absorber has recovered by $1/e$ ($\sim 37\,\%$) after complete bleaching. In saturable absorbers based on a doped insulator, the excited state decays back to the ground state by spontaneous emission. This period should ideally be significantly longer than the pulse duration of the generated laser pulse, to avoid that the saturable absorber already recovers during the pulse build-up time and thus attenuates the building-up pulse by re-absorption. On the other hand, the recovery time should not be too long, otherwise a satellite pulse can be formed by reaching population inversion in the gain medium again while pumping the system continuously.

In addition, with passively Q-switched lasers at high repetition rates, a long recovery time can lead to a situation where the saturable absorber is not fully recovered when the subsequent pulse is formed. If this is the case, the subsequent pulse has a reduced modulation depth and thus smaller pulse energy, which leads to unwanted dynamics and instability in the laser. As a rough estimate, the recovery time should be between the pulse duration and the upper-state lifetime of the gain medium being used. As an example, Figure 2.7 shows an idealized exponential decay with a fictitious excitation by an ultrashort pulse at time τ_0. The subsequent decay of the excited states with a recovery time of $4\,\mu s$ $(1/e)$ takes $18.5\,\mu s$ until the absorber is almost completely recovered ($>99\,\%$). In this case, at repetition rates of about $54\,\text{kHz}$ ($\approx 1/18\mu s^{-1}$), the absorber would not recover completely between succes-

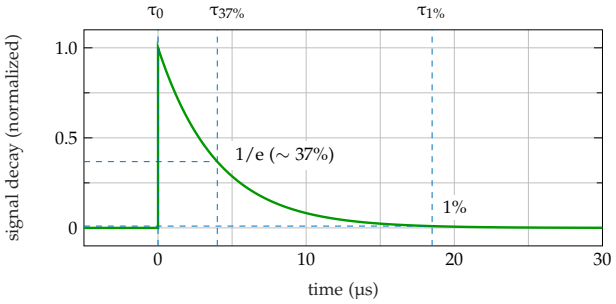

Figure 2.7: Idealized exponential decay of excited states of a saturable absorber after it has been excited by a fictitious ultrashort pulse at time τ_0.

sive pulses and thus develop unwanted dynamics (e.g. satellite pulses) and instabilities. Compared to the idealized decay rate, the decay processes of saturable absorbers can be more complicated in reality and thus deviate from a simple single-exponential decay e.g. exhibiting a double-exponential decay.

3 SIMULATION AND SYSTEM DESIGN

In this Chapter different simulation methods are introduced, which will be used in the following chapters to improve the understanding of the system and to reconcile theory and experimental investigations. In this context, a rate equation model is used to calculate the temporal occupation dynamics of the gain medium and the saturable absorber by coupled rate equations. This allows subsequently to calculate different systems output quantities such as pulse energy, repetition rate, or pulse duration for a passively Q-switched system. Furthermore, the second threshold criterion for passively Q-switched lasers is considered and applied to a quasi-three-level system based on Nd^{3+}:YVO_4 as gain medium and Cr^{4+}:YAG as saturable absorber. In addition, the resonator stability is investigated using a matrix formalism approach. Here, in addition to the fundamental mode, higher-order transverse modes are also considered and the influence of the pump-induced thermal lensing on the resonator stability is examined. Finally, the gain crystal is thermally analyzed using finite element analysis (FEA), and the influence of the pump spot diameter, pump wavelength, and applied pump power on the peak temperature in the crystal is investigated.

3.1 RATE-EQUATION MODEL

According to previous work on the theory of passively Q-switched lasers [44, 45, 68–70], the coupled rate equations taking into account ESA of the saturable absorber and reabsorption losses of the quasi-three level system are given by

$$\frac{d\phi}{dt} = \frac{\phi}{t_r}[2\sigma_g N_g l_g - 2\sigma_{\text{reab}} l_g - 2\sigma_{\text{GSA}} N_{GS} l_{SA} - 2\sigma_{\text{ESA}} N_{ES} l_{SA} - L + \ln(R)] \tag{3.1}$$

$$\frac{dN_g}{dt} = W_p - \frac{N_g}{\tau_g} - \gamma\sigma_g c\phi N_g \tag{3.2}$$

$$\frac{dN_{GS}}{dt} = \frac{N_{SA} - N_{GS}}{\tau_{SA}} - \sigma_{GSA} c\phi N_{GS} \frac{A_g}{A_{SA}} \tag{3.3}$$

with

$$N_{SA} = N_{GS} + N_{ES}. \tag{3.4}$$

Where Φ is the photon density in the resonator, t_r is the resonator round-trip time, σ_g is the stimulated-emission cross-section of the laser crystal, N_g is the population inversion density in the gain medium, l_g is the length of the laser crystal, σ_{reab} is the reabsorption cross-section in the quasi-three level system, σ_{GSA} and σ_{ESA} are the GSA and ESA cross-sections of the saturable absorber, respectively. Further, l_{SA} is the length, N_{GS} and N_{ES} are the occupation densities of the ground and excited absorber states, respectively, L is the non-saturable resonator losses, R is the reflectivity of the OCM, τ_g is the upper laser level lifetime, γ is the inversion reduction factor, t_{SA} is the excited lifetime of the saturable absorber, and A_g and A_{SA} are the beam area in the gain

medium and saturable absorber, respectively.
In addition to this, the volumetric pump rate

$$W_p = \eta_q P_{pump} \frac{1 - \exp(-2\sigma_{abs} l_g)}{h\nu A_g l_g} \tag{3.5}$$

can be expressed by the pump efficiency n_q, the applied pump power P_{pump}, the absorption cross-section of the gain medium σ_{abs}, the Planck's action quantum h, and the pump frequency ν. Again, the resonator round-trip time is given by

$$t_r = l_c / c \tag{3.6}$$

from the resonator length l_c and the speed of light c. In addition, the initial population inversion in the gain medium for low intensities in the resonator can be expressed by

$$N_{g_i} = \frac{L - \ln(R) - \ln(T_0^2)}{2\sigma_g l_g} \tag{3.7}$$

while the threshold occupation inversion assuming a fully bleached absorber can be expressed as [71]

$$N_{g_{th}} \cong \frac{2\sigma_g N_{SA} l_{SA} + \ln\left(\frac{1}{R}\right) + L}{2\sigma_g l_g}. \tag{3.8}$$

Besides, under the assumption that the photon density is small after the Q-switched pulse is decoupled, the following transcendental equation

$$N_{g_i} - N_{g_f} - N_{g_{th}} \ln\left(\frac{N_{g_i}}{N_{g_f}}\right) = 0 \tag{3.9}$$

is obtained which couples the final occupation inversion of the gain medium with the initial and the threshold occupation inversion.

The numerical solution of this transcendental Equation 3.9 [72] finally leads to the values for N_{g_i}, $N_{g_{th}}$, and N_{g_f}, which can be used to obtain the pulse energy [57]

$$E_p = \frac{h\nu A_g}{2\sigma_g \gamma} \ln\left(\frac{1}{R}\right) \ln\left(\frac{N_{g_i}}{N_{g_f}}\right) \tag{3.10}$$

and peak power

$$P_p = \frac{h\nu A_g l_g}{\gamma t_r} \ln\left(\frac{1}{R}\right) \left[N_{g_i} - N_{g_{th}} - N_{g_{th}} \ln\left(\frac{N_{g_i}}{N_{g_f}}\right)\right]. \tag{3.11}$$

By the pulse energy E_p and peak power P_p finally the pulse duration

$$t_p \approx \frac{E_p}{P_p} \tag{3.12}$$

can be estimated.
If the system is pumped continuously, the repetition rate f_{rep} of successive pulses can be calculated by the upper laser level lifetime τ_g, the volumetric pumping rate W_p and the initial, as well as final occupation inversion N_{g_i} and N_{g_f} to [73]

$$f_{rep} = \frac{1}{\tau_g} \ln\left(\frac{W_p t_g - N_{g_i}}{W_p t_g - N_{g_f}}\right). \tag{3.13}$$

Figure 3.1 shows an exemplary numerical solution of the coupled rate equations 3.1 - 3.3 for a period of 40 µs in the case of a continuously pumped system. The equations were solved in Matlab using a standard ordinary differential equation solver (ODE45) based on the Runge-Kutta method [72]. The time evolution of the occupation inversion of the gain medium and the saturable absorber is shown as blue and green line, respectively, while the resonator-internal photon density is shown as red line. The continuous pumping process causes the occupation in-

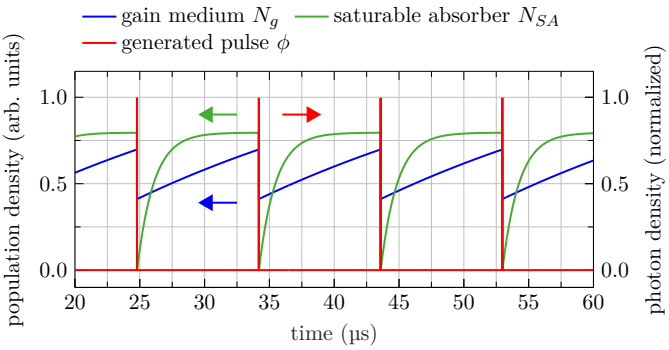

Figure 3.1: Solution of rate equations 3.1 - 3.3 for repeated passive Q-switching based on simulation parameters of Table 3.1. The evolution of the occupation density of the gain medium (blue line) and saturable absorber (green line) are part of the left axis, while the resulting photon density is shown as a red line and belongs to the right axis.

version in the gain medium to increase, while the spontaneous emission increases due to the increasing occupation inversion, which also leads to a limited increase of occupation inversion in the saturable absorber. At a certain point in time, the absorber suddenly switches through, causing the photon density in the resonator to increase abruptly and the energy stored in the gain medium to become apparent in a laser pulse. This reduces the occupation inversion in the gain medium and the process starts all over again due to continuous pumping. For a continuously pumped system like this, the pump power and the resulting volumetric pump rate are used to set the duration of the build-up of the population inversion, which has a direct influence on the repetition rate of the system. For the simulation shown in Figure 3.1 and all subsequent calculations in Chapter 4, the constants shown in Table 3.1 were used unless otherwise specified.

symbol	parameter	value	unit
σ_g	stimulated-emission cross-section	2.1×10^{-20}	cm^2
l_g	length gain medium	5	mm
σ_r	reabsorption coefficient	0.2×10^{-20}	cm^2
τ_g	relaxation time gain medium	90	µs
T_0	saturable absorber initial transmission	96	%
R	output coupler reflectivity	92	%
L	non-saturable loses	3	%
l_{SA}	length saturable absorber	0.7	mm
σ_{GSA}	GSA cross-section	4.4×10^{-18}	cm^2
σ_{ESA}	ESA cross-section	2×10^{-18}	cm^2
τ_{SA}	relaxation time saturable absorber	4	µs
ω_{gain}	waist radius gain medium	100	µm
ω_{SA}	waist radius saturable absorber	100	µm
γ	inversion reduction factor	2	
η_q	pump efficiency	45	%
P_{pump}	applied pump power	25	W
σ_{abs}	pump absorption coefficient	8	cm^{-1}
ν	pump frequency	371	THz
l_c	resonator length	15	mm

Table 3.1: Overview of the simulation parameters used for the rate equation analysis for a passively Q-switched laser based on Nd^{3+}:YVO_4 and Cr^{4+}:YAG.

3.2 SECOND THRESHOLD CONDITION

The laser threshold of Equation 2.2 was defined as the point where the gain exceeds unsaturated cavity losses and the intensity inside the cavity can grow at all. For passively Q-switched operation another expression called the second threshold condition is of great importance [74, 75]. The second threshold condition defines whether the temporal derivative of the intracavity photon density is positive or negative. A positive derivative is linked to an increase in photon density due to

dominating laser gain whereas a negative sign means the density decreases as the saturable absorber loses are dominating. Practically this means that the saturable absorber losses have to saturate before saturation of the gain medium takes place to obtain Q-switched operation.
Starting from the first formulation in 1978 [76], the second threshold condition was continuously evolved [45, 77] and finally extended by Bai et al. [78] to include the influence of ESA.
In the case that the inequation of the second threshold condition is not fulfilled the laser tends to operate in CW operation [45, 56]. The second threshold condition is defined as

$$\frac{\ln(1/T_0^2)}{\ln(1/T_0^2)+\ln(1/R)+L}\,\frac{\sigma_{\mathrm{GSA}}}{\sigma_{\mathrm{gain}}}\,\frac{A_{\mathrm{gain}}}{A_{sa}} > \frac{\gamma}{1-\beta}, \tag{3.14}$$

where T_0 is the saturable absorber initial transmission, R the reflectivity of the output coupler, L the non-saturable dissipative cavity losses, σ_{GSA} is the stimulated-emission cross-section of the gain crystal, and A_{gain}/A_{sa} the ratio of laser mode area and mode area in the saturable absorber. Further, γ is the population inversion reduction factor (one for a four-level system and two for a three-level laser) and $\beta = \sigma_{\mathrm{ESA}}/\sigma_{\mathrm{GSA}}$ the ratio of the ESA and GSA cross-section.
For $\beta < 1$ due to predominating saturable absorption, it is obvious that the right side of Inequation 3.14 is always greater than two for a three-level laser. However, the first term on the right side is always significantly smaller than one due to a certain initial transmission, output coupler reflectivity, and non-negligible dissipative cavity losses. Consequently, both the ratio of cross-sections $\sigma_{\mathrm{GSA}}/\sigma_{\mathrm{gain}}$ as well as the ratio of laser mode areas $A_{\mathrm{gain}}/A_{\mathrm{sa}}$ have to be noticeably greater than one, to fulfill the inequation. It is obvious that this is not naturally fulfilled and puts serious conditions on the design of a Q-switched laser system. For this reason, the second threshold condition (Inequation 3.15) in the case of a quasi-three-level laser system based on Nd^{3+}:YVO_4 as gain

medium and Cr^{4+}:YAG as saturable absorber is calculated and investigated subsequently for typical system parameters. Therefore, the initial transmittance T_0 of the saturable absorber and the reflectivity R of the OCM were varied in a certain range for the later laser design. In addition, the ratio of the beam area of the laser mode and the area of the saturable absorber was assumed to be one, since the plane-parallel resonator should be rather short to obtain short pulse durations and consequently the spot diameter in the gain medium and saturable absorber does not differ significantly. Additionally, an illustrative value of 3 % was estimated for the nonsaturable losses, while literature values were used for the cross-sections of the saturable absorber (σ_{GSA} = 3.9×10^{-18} cm^2 and σ_{GSA} = 1.4×10^{-18} cm^2 [79]) and the stimulated-emission cross-section of Nd^{3+}:YVO_4 at 914 nm (σ_{gain} = 4.8×10^{-20} cm^2 [34]). The constants used for the calculation are summarized in Tab. 3.2. To perform the simulations, Equation 3.14 was adapted to

$$\frac{\ln(1/T_0^2)}{\ln(1/T_0^2) + \ln(1/R) + L} \frac{\sigma_{\mathrm{GSA}}}{\sigma_{\mathrm{gain}}} \frac{A_{\mathrm{gain}}}{A_{sa}} \frac{1-\beta}{\gamma} > 1, \tag{3.15}$$

symbol	parameter	value	unit
T_0	saturable absorber initial transmission	80-100	%
R	output coupler reflectivity	80-100	%
L	non-saturable loses	3	%
σ_{GSA}	GSA cross-section	3.9×10^{-18}	cm^2
σ_{ESA}	ESA cross-section	1.4×10^{-18}	cm^2
σ_{gain}	stimulated-emission cross-section	4.8×10^{-20}	cm^2
ω_{gain}	waist radius gain medium	100	µm
ω_{SA}	waist radius saturable absorber	100	µm
γ	inversion reduction factor	2	

Table 3.2: Overview of the simulation parameters used to calculate the second threshold criterion.

and then a parameter sweep was performed on the initial transmission, as well as the reflectivity of the OCM in Matlab using loops. The result of the simulation is shown in Figure 3.2 for different initial transmissions and output coupler reflectivities between 80-100 %. Due to the rearranged second threshold condition (Inequation 3.15), the passive Q-switched operation requires that the left part of the inequation is greater than one.

Overall, the calculated values are for all combinations of initial transmission and output coupler reflectivities well above a value of two and consequently, the passively Q-switched operation should work in principle.

The reason that in quasi-three level operation the second threshold condition is satisfied quite easily is due to the relatively small stimulated-emission cross-section at 914 nm ($\sigma_{gain} = 4.8 \times 10^{-20}\,\mathrm{cm}^2$) compared to the ground state absorption cross-section of the saturable absorber ($3.9 \times 10^{-20}\,\mathrm{cm}^2$).

In comparison to that, for the four-level system, the literature value of the stimulated-emission cross-section at 1064 nm ($1.2 \times 10^{-18}\,\mathrm{cm}^2$ [80]) is larger by a factor of 25, and consequently, care must be taken in the choice of design parameters to satisfy the second threshold condition. A possible solution, in this case, is to reduce the spot size on the saturable absorber compared to the spot size in the gain medium. This can be done for example by using a curved resonator mirror.

The minimum in Figure 3.2 was reached with 0.99 for a purely hypothetical initial transmission of 100 % and an output coupler reflectivity of 80 % (upper left corner). Like the maximum value of 24.2, which was reached for an initial transmission theoretical output coupler reflectivity of 100 %, the minimum value for a purely hypothetical initial transmission of 100 % makes no physical sense. For an initial transmission of 100 %, the saturable absorber would be vividly completely transparent and the laser would not be passively Q-switched but would

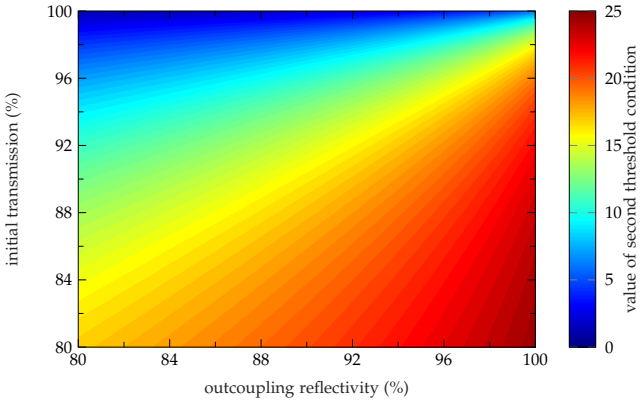

Figure 3.2: Calculated parameter sweep of the left side of the second threshold criterion over the initial transmittance of the saturable absorber and the reflectance of the output coupler mirror according to the left side of Inequation 3.15). Hereby, simulation parameters of Table 3.2 were utilized.

run in CW mode. On the other hand, an output coupler reflectivity of 0 % would mean that the output coupler is completely transparent and consequently the laser would not work because the optical feedback through the resonator is missing.

3.3 MATRIX FORMALISM - CAVITY STABILITY

The following derivation is adapted from the work of Kogelnik et al. [81] and Hodgson et al. [82]. Accordingly, in a paraxial approximation, the beam propagation of an optical system can be described by ray transfer matrices [83]. Assuming a uniform heat input, a gain crystal in the resonator can be approximated consequently as a thick lens, with the distance h of the principal planes from the end are given by

$$h = \frac{l}{2n_0}, \tag{3.16}$$

where n_0 is the refractive index of the laser crystal and l is the length of the gain medium [84–88]. Without a thermal lens, the system can be described via the stability parameter

$$g_i = 1 - (d_1 + d_2)/\rho_i \qquad i, j = 1, 2; i \neq j \tag{3.17}$$

and the resonator length

$$L = d_1 + d_2. \tag{3.18}$$

Here, $d1$ and $d2$ are the respective mirror spacing and ρ_i is the radius of curvature of the mirror i.
For the propagation of a Gaussian beam, the concept of the stability parameters g_i can be adapted, according to which the system with a thermal lens of refractive power $D = 1/f$ can be described via

$$g_i^* = g_i - Dd_j(1 - d_i/\rho_i) \qquad i, j = 1, 2; i \neq j \tag{3.19}$$

$$L^* = d_1 + d_2 - Dd_1d_2. \tag{3.20}$$

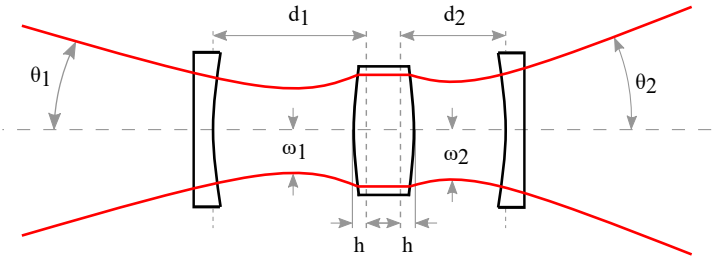

Figure 3.3: Schematic overview of the components and parameters of the ray transfer matrix model for calculating resonator stability as a function of thermal dioptric power.

As shown in Figure 3.3, d_1 and d_2 correspond to the mirror distance from the principal planes of the crystal while L^* is the effective resonator length considering a thick lens.

Analogous to a resonator without a thermal lens, a stability diagram can be defined via the g^* parameters, where the resonator stability is now a function of the refractive power D. Such a diagram is exemplarily shown in Figure 3.4 for a 5 mm long Nd^{3+}:YVO_4 crystal ($n = 1.9647$ [89]), where the in-coupling resonator mirror is dielectrically deposited on the crystal ($d_1 = h$, $r_1 = \infty$) and the planar external output coupler mirror ($r_2 = \infty$) has a distance of d_2 =10 mm to the principal plane of the equivalent thick lens principal plane. These and other parameters used below are summarized in Tab. 3.3.

Without a thermal lens, the plane-parallel resonator is located at the stability boundary (blue point, $g_1^* g_2^* = 1$), which is represented by the green line. Outside this zone (gray area), laser operation is not possible, since the Gaussian beam does not reproduce itself after a resonator revolution, but becomes larger. With increasing cavity round trips a strong power drop can be observed due to diffraction of the beam. Thermal lensing causes the resonator stability point to move along the red dashed line through the stable (white area) and unstable zones. As the

symbol	parameter	value	unit
l	length of the gain medium	5	mm
n_0	refractive index of the gain medium	1.965	
d_1	left mirror to principal plane distance	h = 1.3	mm
d_2	right mirror to principal plane distance	10 - h	mm
ρ_1	radius of curvature mirror 1	∞	mm
ρ_2	radius of curvature mirror 2	∞	mm
D	thermal dioptric power	0 - 1000	m^{-1}
λ	laser wavelength	914	nm
b	gain medium beam radius	150	µm

Table 3.3: Overview of parameters used to calculate resonator stability based on ray transfer matrices.

thermal lens increases, there are a total of four characteristic points at which the resonator has an intersection with the stability boundary. These four points are given by

$$D_I = -\frac{1}{\rho_1 - d_1} - \frac{1}{\rho_2 - d_2} \qquad \text{for} \qquad g_1^* g_2^* = 1 \quad \text{and} \quad g_1^* > 0 \tag{3.21}$$

$$D_{II} = -\frac{1}{\rho_1 - d_1} + \frac{1}{d_2} \qquad \text{for} \qquad g_1^* = 0 \tag{3.22}$$

$$D_{III} = \frac{1}{d_1} - \frac{1}{\rho_2 - d_2} \qquad \text{for} \qquad g_2^* = 0 \tag{3.23}$$

$$D_{VI} = \frac{1}{d_1} + \frac{1}{d_2} \qquad \text{for} \qquad g_1^* g_2^* = 1 \quad \text{and} \quad g_1^* < 0. \tag{3.24}$$

For the example parameters already used above, as can be seen in Figure 3.4, the four intersection points result for the following refractive powers:

$$D_I = 0\,\mathrm{m}^{-1} \qquad D_{II} = 114.6\,\mathrm{m}^{-1} \tag{3.25}$$

$$D_{III} = 785.9\,\mathrm{m}^{-1} \qquad D_{IV} = 900.5\,\mathrm{m}^{-1}. \tag{3.26}$$

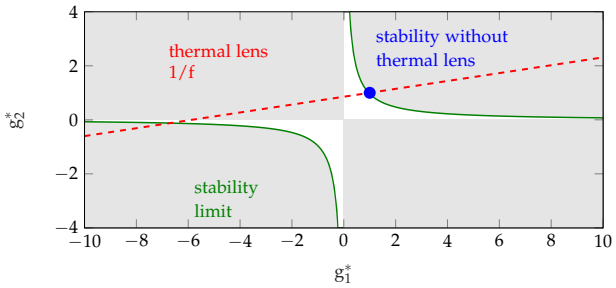

Figure 3.4: Stability diagram of the resonator parameters g_1^* and g_2^* with the stability point without thermal lens (blue dot) and the evolution of stability with increasing thermal lens (red dashed line).

For a refractive power between D_I and D_{II}, the resonator is in the stability region, while above D_{II} to D_{III} no laser operation is possible. For an even larger thermal refractive power between D_{III} and D_{IV}, a second stable region is reached, which the resonator leaves again above D_{IV}.

For the case of the **fundamental mode** with wavelength λ, the propagation in the resonator can be given by the beam radius

$$\omega_i^2 = \frac{\lambda L^*}{\pi} \sqrt{\frac{g_j^*}{g_i^*(1 - g_1^* g_2^*)}} \tag{3.27}$$

at the mirrors [82]. Here i and j, respectively, can take the values 1 and 2, where i and j must always be different from each other. The two coefficients i and j take into account that the thermal lens in the resonator, as shown in Figure 3.3, forms two-beam waists to the left and right of the thick lens. The beam waist radius ω is given by

$$\omega_{0i}^2 = \frac{\lambda L^*}{\pi} \frac{g_1^* g_2^* (1 - g_1^* g_2^*)}{g_j^* (L^*/\rho_i^2)^2 + g_i^* (1 - g_1^* g_2^*)}, \tag{3.28}$$

while the respective divergence angle is given by

$$\theta_{0i} = \frac{\lambda}{\pi \omega_{0i}}. \tag{3.29}$$

Furthermore, the beam radius at the principal planes of the thick lens can be calculated by

$$\omega_L^2 = \omega_1^2 \left[\left(1 - \frac{d_1}{\rho_1}\right)^2 \left(\frac{d_1}{L^*}\right)^2 \frac{g_1^*(1 - g_1^* g_2^*)}{g_2^*} \right]. \tag{3.30}$$

The previous Equations 3.27 to 3.30 have shown that the beam radius at the mirrors, as well as the waist radius and also the divergence angle implicitly depend on the refractive power D of the thermal lens.
For the exemplary values used before, both the beam radius and the divergence angle were calculated and the results are shown in Figure 3.5 (a) and (b) as a dashed line. In the figure legend, the abbreviation fm stands for the fundamental mode while the abbreviation mm is linked to multi-mode. As already shown in the stability diagram in Figure 3.4 there are two stable resonator zones and therefore four thermal dioptric refractive powers D_I - D_{IV} at which the resonator is crossing the stability boundary. Here, the gray area marks the area of the refractive power where the laser cannot operate under any circumstances because Equations 3.27 - 3.30 have no real solution.
The beam radius at the left mirror (green dashed line) and in the laser crystal (orange dashed line) is quite constant in the fundamental mode in the left stability zones, while the radius in the right zone is significantly different from the radius in the crystal. For both zones, it can be observed that the radius at the left OCM decreases significantly with increasing refractive power and tends towards zero. In turn, this causes the beam intensity at the left mirror to increase more and more, and consequently, laser-induced damage to the OCM or saturable absorber can be expected.

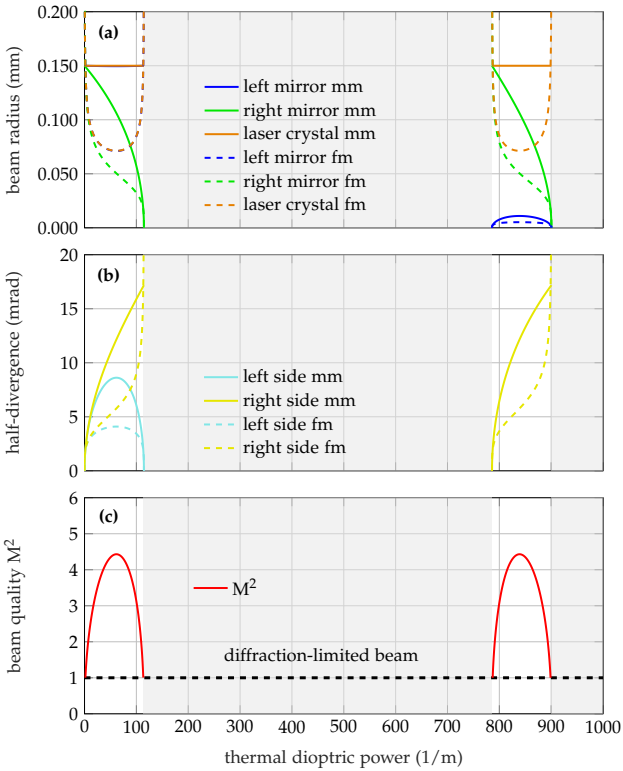

Figure 3.5: Simulation results of the ray transfer matrix stability analysis. Hereby, the beam radius in (a), the beam divergence in (b), and the beam quality factor in (c) were investigated as a function of the thermal dioptric power. For the simulations the parameters according to Table 3.3 were used. In the figure legend, the abbreviation 'fm' stands for the fundamental mode while 'mm' is linked to multi-mode.

The corresponding divergence angle is plotted in (b) against the thermal dioptric refractive power. For the left stability region, the divergence angle initially increases with increasing refractive power for both the left and the right beam waists. While the divergence angle on the right

side of the laser crystal continues to increase with increasing refractive power, the divergence angle on the left side decreases again. This behavior results from the fact that the left resonator mirror is directly applied to the laser crystal and consequently has a very small distance ($d_1 = h$) to the main plane of the thick lens. On the other hand, the right resonator mirror is much further away from the thermal lens and consequently, the increasing refractive power has a larger influence on the divergence angle. In the case of an experimental laser setup, the exemplarily chosen parameters would imply that the laser beam would be coupled out via the right resonator mirror. Consequently, only the waist and divergence angle on the right side is interesting for experiments, since the beam on the left side of the crystal does not leave the resonator anyway.

In the right stability zone from 785.9 - 900.5 m^{-1} the divergence angle of the right fundamental mode increases with increasing refractive power. Since the beam-parameter product ($\omega_0 \cdot \theta$) is constant for the fundamental diffraction-limited Gaussian mode ($\lambda / \pi = 0.291\,\mathrm{mrad}$), the beam radius from (a) and the divergence angle from (b) behave exactly opposite. Accordingly, for the small beam radius ($< 0.05\,\mathrm{mm}$) at the left mirror of the right zone, a very large divergence angle ($> 58\,\mathrm{mrad}$) is expected which is no longer in the plot area of the shown figure.

If the laser beam in the resonator is not limited by an aperture, **higher transverse multi-modes** with a radius, larger than the radius of the fundamental mode can form due to pumping of the laser crystal or beam distortion caused by the thermal lens. Here, parameter b indicates the radius in the gain crystal, over which, as a ratio to the fundamental mode radius ω_L, the beam quality factor

$$\mathrm{M}^2 = \left(\frac{b}{\omega_L} \right)^2 \tag{3.31}$$

can be determined. Illustratively, for a longitudinal pumped crystal, the parameter b can be understood as the pump spot radius. The beam radius ω_L of the fundamental mode is always smaller than the radius of transverse multi-modes and consequently the beam quality factor M^2 must always be greater than or equal to one. Since the radius in the gain crystal is a function of the pump power and consequently of the thermal refractive power, the beam radius at the principal planes of the thick lens can be substituted for ω_L, so that it follows that

$$M^2 = \omega_1^2 \left[\left(1 - \frac{d_1}{\rho_1}\right)^2 \left(\frac{d_1}{L^*}\right)^2 \frac{g_1^*(1 - g_1^* g_2^*)}{g_2^*} \right]^{-1}. \tag{3.32}$$

As the beam quality factor is the ratio of the radius of the fundamental mode to higher transverse modes, the radius and divergence angle of multi-modes can be calculated using M^2, taking into account the fundamental mode, as follows

$$\omega_{mmi} = \sqrt{M^2}\omega_{0i} \qquad \theta_{mmi} = \sqrt{M^2}\theta_{0i}. \tag{3.33}$$

Analogously to the fundamental mode, the beam radius, divergence angle and additionally the beam quality factor of the transverse multi-mode are shown in Fig. 3.5. Here, a fixed radius of 150 µm was assumed for the pump spot equivalent parameter b. At the stability boundaries, the multi-mode beam radius and divergence angle are the same as for the fundamental mode, while in the stability zone itself, a different profile is observed across the thermal refractive power due to M^2 values different to one.

Figure 3.5 (c) shows the beam quality factor M^2 versus thermal refractive power. The dashed line with $M^2 = 1$ represents the diffraction limit of the fundamental mode. For the exemplary beam quality simulations, an initial increase and then a symmetric decrease can be observed in both stability zones with increasing refractive power. Hereby, the maxi-

mum value of the beam quality factor with an M^2 of 4.4 corresponds to a multi-mode beam radius which is larger by a factor of 4.4 compared to the fundamental mode.

For the following chapters, the matrix model shown here will be used to match experimental investigations and to make predictions for a better understanding of the system.

3.4 PUMP-INDUCED HEAT AND TEMPERATURE INVESTIGATIONS

While the temperature distribution in side-pumped laser crystals is relatively homogeneously distributed, especially in end-pumped crystals high peak temperatures and strong temperature gradients can arise due to the non-homogeneous heat distribution, which ultimately reduces the maximum output power and efficiency of the laser [44]. For this reason, there have been several investigations in the past where the continuous pump-induced temperature distribution in solid-state laser crystals was theoretically investigated in the steady-state using different modeling approaches and matched with experiments [44, 90–93]. Consequently, the heat and stress distribution could be theoretically investigated for various contexts such as the influence of the pump spot, pump wavelength, or focal depth and optimized for experiments [94]. Furthermore, the boundary conditions of the theoretical investigations were improved to study the heat and stress distribution for different correlations like the influence of the pump spot, the pump wavelength, or the focal depth and to optimize them for experiments [94]. Moreover, the model was enhanced so that, in addition to water cooling by the crystal holder, convective heat transfer between the crystal and the

ambient air [95, 96] or different radial beam profiles such as top-hat [90, 97] or Gaussian profiles [91, 98, 99] were also considered. Through simulations, it was shown that compared to conventional crystals, using a composite rod crystal with undoped end caps improved thermal diffusion and significantly reduced the peak temperature in the laser crystal. The reason is that the undoped end cap has much better thermal conductivity than the air interface and also bulging of the end faces can be reduced as a result of inhomogeneous heating. This was first investigated for an end-pumped Nd^{3+}-doped YAG laser crystal [91]. On this basis, further work was carried out using Nd^{3+}:YVO_4 and simulation results based on a FEA were compared with experimental work [53, 100, 101]. Besides the time-independent steady-state approaches, an analytical model was established in 2008 by Bernhardi et al. to determine the time-dependent temperature dynamics and consequent temperature-dependent induced stress distribution in QC end-pumped operation [102].

The following steady-state model and description are based on work by [44, 53, 91, 100], where the pump-induced temperature distribution in the crystal was analyzed numerically via a finite element model in Matlab [72].

The temperature distribution can be described in a laser crystal via the three-dimensional Poisson equation

$$K_x \frac{\partial^2 T(x,y,z)}{\partial x^2} + K_y \frac{\partial^2 T(x,y,z)}{\partial y^2} + K_z \frac{\partial^2 T(x,y,z)}{\partial z^2} + q(x,y,z) = 0, \quad (3.34)$$

where x and y are the transverse and z the longitudinal crystal directions. Since YVO_4 is an anisotropic host material and therefore does not have a rotationally symmetric crystal structure, it is necessary to solve a three-dimensional model. In addition, different thermal conductivity

coefficients in the different crystal directions must be assumed. Compared to this, YAG has an isotropic crystal lattice and it is sufficient to calculate a two-dimensional solution. In Equation 3.34, K_x, K_y, and K_z are the corresponding thermal conductivity coefficients along with the different crystal directions, T is the temperature, and $q(x,y,z)$ is the thermal density, which can be expressed as

$$\begin{aligned} q(x,y,z) = &\frac{2Qa_0}{\pi\omega_p^2(z)}(1-\exp(-a_0 l_0)) \\ &\exp\left(\frac{-2(x-a/2)^2-2(y-b/2)^2}{\omega_p^2(z)}\right)\exp(-a_0 z) \end{aligned} \tag{3.35}$$

for a pump source with a Gaussian intensity distribution. This consists of a superposition of two terms. In the front part of the equation, the heat input by the pump light is considered while in the back part the spatial displacement of the pump spot in the crystal is taken into account. Hereby, Q is the generated heat, a_0 is the absorption coefficient, w_p is the approximation of the pump radius, l_0 is the length of the crystal in the longitudinal direction and a and b are the transverse displacement of the thermal density in the crystal, respectively.
The generated heat

$$Q = P_{pump}\left(1-\frac{\lambda_{pump}}{\lambda_{lase}}\right)\sin(g) \tag{3.36}$$

takes into account the quantum defect as the quotient of the pump and laser wavelengths (λ_{pump} and λ_{lase}) and the applied pump power P_{pump} as well as the small-signal gain g. A multi-mode fiber-coupled semiconductor laser was adopted as the pump source. Accordingly, in the far-field, the beam profile deviates from a Gaussian intensity distribution and is superimposed with a top-hat profile [100]. For this reason, the pump radius is given in paraxial approximation by

$$\omega_p(z) = \omega_0 + \theta_p|z-z_0|, \tag{3.37}$$

where ω_0 is the waist of the pump spot, θ_p the half far-field divergence angle, and z_0 the relative longitudinal displacement of the pump spot concerning the entrance surface.

A constant cooling water temperature of 288 K was chosen for the boundary conditions of the crystal interfaces to the holder, while a crystal-air transition with the convective heat transfer coefficient h_{tr} was chosen at the two end facets of the crystal. Thus, the boundary conditions for the six crystal facets result in

$$T\left(-\frac{a}{2}, y, z\right) = 288; \qquad T\left(\frac{a}{2}, y, z\right) = 288; \tag{3.38}$$

$$T\left(-\frac{b}{2}, y, z\right) = 288; \qquad T\left(\frac{b}{2}, y, z\right) = 288; \tag{3.39}$$

$$\frac{\partial T(x,y,z)}{\partial z}|_{z=0} = h_{tr}(T - T_{air}); \quad \frac{\partial T(x,y,z)}{\partial z}|_{z=l} = -h_{tr}(T - T_{air}). \tag{3.40}$$

Figure 3.6 (a) shows an exemplary crystal geometry with $3x3x5\,\mathrm{mm}^3$ and the corresponding facets F1 to F6. For facets F1 and F2 the crystal-air transition was assumed, while for facets F3 to F6 the constant cooling water temperature is applied.

To calculate the pump-induced temperature distribution in the laser crystal, Equation 3.34 was solved in the steady-state using FEA in Mat-

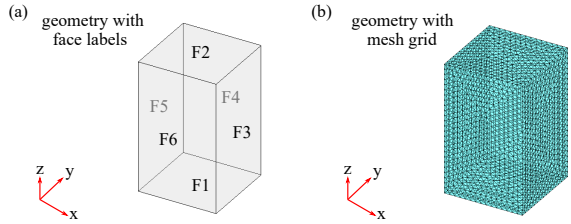

Figure 3.6: Example crystal geometry for calculation of pump-induced heat based on FEA. In (a) the different face labels are drawn, while (b) shows the geometry with the mesh grid used.

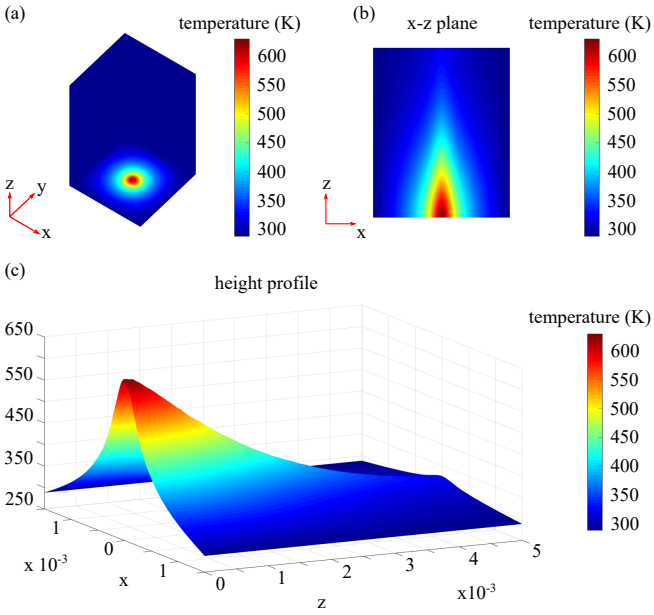

Figure 3.7: Simulation results for pump-induced heat based on FEA. In (a) the used crystal geometry with temperature profile is shown, while in (b) a section through the x-z plane can be seen. Figure (c) shows the generated temperature profile as a height profile.

lab, taking into account the different boundary conditions. A mesh structure with sufficient fineness ($m = 0.0002$) was chosen for the solution, which is shown in Figure 3.6 (b) together with the geometry of the crystal. The mesh size was reduced to such an extent that further refinement did not lead to any significant improvement of the results.

Figure 3.7 shows exemplary results of the conducted simulations. Here, a pump power of 50 W at 808 nm was used. For the absorbed pump light, a Gaussian intensity distribution with a diameter of 200 µm was assumed as the pump spot in the $3x3x5\,\mathrm{mm}^3$ Nd^{3+}:YVO_4 crystal. In

Figure 3.7 (a), the laser crystal geometry is shown with the generated temperature profile on the input facet. As the crystal is pumped centrally, a symmetric temperature gradient is formed in the transverse (x-y plane) direction towards the interfaces that are connected to the constant cooling water temperature. In Figure 3.7 (b), the central cross-section through the x-z plane of the crystal is shown with the resulting temperature distribution. Since the pump light enters the crystal facet centrally and the highest power is absorbed there, the highest temperature is located at this point. Due to the different thermal conductivity coefficients of Nd^{3+}:YVO_4 and various boundary conditions, an asymmetric temperature profile is formed along the longitudinal direction. Further, as can be seen in Figure 3.7 (c), the temperature distribution in the longitudinal z-direction decreases exponentially as the pump light is absorbed according to Beer–Lambert's law. Assuming a 5 mm long crystal, with an absorption coefficient of $5.32 \times 10^2\,\mathrm{cm}^{-1}$, a total of 93 % of the incident pump light is absorbed along the longitudinal direction. For this simulation the obtained maximum temperature in the crystal is 626 K which is equivalent to almost 353 °C. Compared to the cooling water temperature of 288 K applied to the crystal facets, this corresponds to a temperature difference of 338 K between the hottest point and the interfaces of the crystal. On the one hand, the high-temperature level in the crystal leads to a reduction of the absorption [103] and emission cross-sections [25], but also to a significant increase of the thermal occupation in the lower laser level, which leads to enhanced reabsorption and reduction of the occupation inversion. On the other hand, the strong temperature gradient at the pump facet leads to the formation of a strong thermal lens and aberrations, which degrade the beam quality. Furthermore, the temperature gradient induces mechanical stress in the crystal, which leads to bulging of the pumped end face and induces mechanical stress, which in the worst-case ends in thermal fracture of

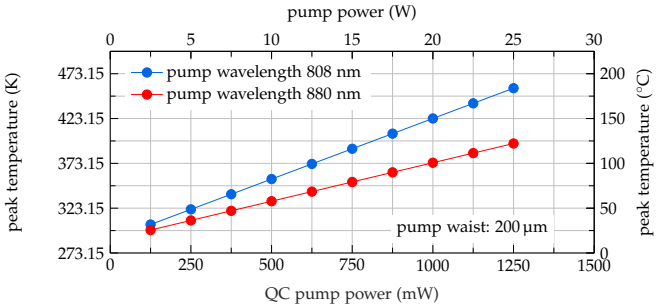

Figure 3.8: Simulation results for the calculation of the pump-induced heat as a function of the applied QC pump power for a pump wavelength of 808 nm (blue line) and 880 nm (red line).

the crystal.

In the following, basic simulations were performed using the FEA to study the pumping laser-induced heat of a Nd^{3+}:YVO_4 crystal. For this purpose, the simulation constants and parameters according to Table 3.4 were chosen and the pump wavelengths at 808 nm and 880 nm were compared. The maximum temperature as a function of pump power was investigated for 808 nm and 880 nm using the FEA and the results are shown in Figure 3.8. Here, at a constant pump waist diameter of 200 µm, the applied CW pump power was varied in a loop between 2.5 W and 25 W. At a duty cycle of 5 % (10 ms / 200 ms), this corresponds to a converted QC pump power between 125 mW and 1250 mW. With increasing pump power, a linear increase in peak temperature with different slopes was observed for both 808 nm and 880 nm. Meanwhile, the resulting peak temperature as a function of pump power was determined automatically. Whereas for low pump powers the peak temperature hardly differs (298.7 K for 880 nm and 304.9 K for 880 nm at 125 mW QC pump power, respectively), there is a significant difference at an applied QC pump power of 1250 mW. Here, the peak temperature

symbol	parameter	value	unit
P_{pump}	applied pump power	2.5 - 25	W
K_x	thermal conductivity x-direction	5.1	$\mathrm{W\,m^{-1}\,K^{-1}}$
K_y	thermal conductivity y-direction	5.1	$\mathrm{W\,m^{-1}\,K^{-1}}$
K_z	thermal conductivity z-direction	5.23	$\mathrm{W\,m^{-1}\,K^{-1}}$
λ_{pump}	pump wavelength	808 / 880	nm
λ_{lase}	laser wavelength	914	nm
a_0	absorption coefficient	5.32	$\mathrm{cm^{-1}}$
ω_0	pump waist radius	25 - 300	µm
θ_0	far-field half-angle	1.5	mrad
z_0	pump spot displacement z-direction	1	mm
a	pump spot displacement x-direction	0	mm
b	pump spot displacement y-direction	0	mm
h_{tr}	convective heat transfer coefficient	4	
T_{air}	room temperature	300	K
T_{water}	cooling water temperature	288	K

Table 3.4: Overview of simulation parameters used to calculate pump-induced heat based on FEA.

at 808 nm is 457.0 K and more than 60 K higher than the calculated value at 880 nm. The peak temperature at 880 nm increases with $85.8\,\mathrm{K\,W^{-1}}$ pump power, whereas a slope of $135.2\,\mathrm{K\,W^{-1}}$ could be calculated for 808 nm. The reason for this difference lies in the significantly smaller quantum defect of just 3.7 % for 880 nm, compared to 11.6 % for 808 nm for the laser transition at 914 nm. As a result, more than twice the pump power is converted into heat.

Besides the influence of the pump power, the dependence of the peak temperature on the pump waist diameter was investigated. The results of the simulations for 808 nm and 880 nm are shown in Fig. 3.9. for waist diameters ranging from 50 µm to 600 µm. In this case, a modualted peak pump power of 10 W was applied, which corresponds to an average QC pump power of 500 mW at a duty cycle of 5 %. With increasing pump waist, an decrease in peak temperature was observed for both 808 nm

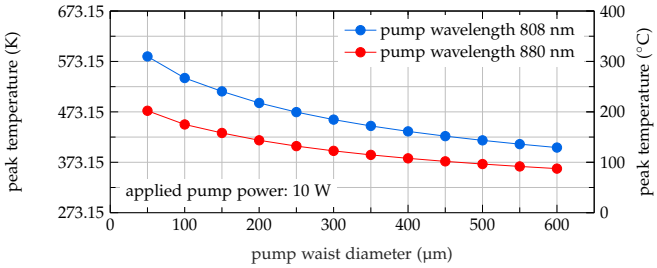

Figure 3.9: Simulation results for the calculation of pump-induced heat as a function of the pump waist diameter used for a pump wavelength of 808 nm (blue line) and 880 nm (red line).

and 880 nm. While the peak temperature at 808 nm at a pump waist of 50 µm, was more than 110 K above that of 880 nm, the peak temperatures of the two wavelengths converged more and more with increasing diameter. With increasing pump waist, an exponential decrease in peak temperature was observed for both 808 nm and 880 nm. While the peak temperature at 808 nm at a pump waist of 50 µm, was more than 110 K above that of 880 nm, the temperatures of the two wavelengths converged more and more with increasing diameter. In principle, the decrease in peak temperature with increasing pump waist at constant pump power is attributable to the decrease in power density. In addition, with a larger pump spot size, the heat input is on average closer to the boundary surfaces which are actively connected to the cooling water.

While the results from Figures 3.8 and 3.9 clearly favor using the pump wavelength of 880 nm instead of 808 nm due to the lower peak temperatures, the consideration of heat input based on the quantum defect is an important, but still not a decisive factor for the performance of a subsequently investigated laser system. In 2012, a theoretical paper by Délen et al. for Nd^{3+}:YVO_4 compared, among other things, the pump

wavelengths at 808 nm and 880 nm concerning overall system performance [104]. Here, it has been shown that counterintuitively there is no advantage using 880 nm instead of 808 nm in terms of the smaller quantum defect, but rather a strong disadvantage. The significantly smaller absorption cross-section at 880 nm basically has to be compensated by a higher doping level or a longer laser crystal length. Both changes significantly increase the reabsorption in the quasi-three-level system, which in turn leads to a decrease in the effective cross-section and consequently worsens the efficiency and threshold of the overall system. In addition, a higher dopant concentration leads to a very strong decrease in the effective upper state lifetime, since the probability for nonradiative decays increases. Consequently, for higher population inversions it is easier to achieve a large small-signal gain. For this reason, in subsequent experiments in Chapter 4 and Chapter 5, 808 nm is set as the pump wavelength compared to 880 nm.

4 Q-SWITCHED LASER EXPERIMENTS

In this Chapter, different important system relationships of a passively Q-switched solid-state laser for use in an automotive lidar sensor are investigated. In this context, the different requirements of a laser for use in an automotive lidar sensor already formulated in the Introduction (Chapter 1) will be considered. Thereby, experimental investigations are analyzed with simulations to explore limitations and to gain a better understanding of how different laser parameters influence each other and a possible lidar sensor performance.

For the various experiments, a total of three different resonator setups are used for this purpose. These different setups offer the advantage that certain relationships can be investigated decoupled from the overall system. The first resonator configuration offers the possibility to switch between CW operation and passive Q-switched operation by an insertable saturable absorber. Here, the influence of the saturable absorber on the laser operation will be investigated. In the second configuration, the absorber is directly bonded to the gain medium and the OCM is discrete, allowing, for example, the resonator length or output coupler reflectivity to be independently changed by adjusting the OCM. In the third configuration, the laser crystal and saturable absorber are separated from each other and each is coated with the resonator coatings. Consequently, the temperature dependence of the gain medium can be studied without affecting the saturable absorber.

4.1 STATE-OF-THE-ART

In the following, a brief overview of literature related to the following experimental investigations of will be given.
The **conversion and slope efficiency** of a laser is influenced by various factors such as the lifetime of the upper laser level, the quantum defect between pump and laser wavelength, the internal resonator losses, or the output coupler reflectivity. In addition to that, a smaller stimulated-emission cross-section in a quasi-three-level system compared to a classical four-level system also leads to a reduction of the maximum achievable efficiency. For example, for CW operation of Nd^{3+}:YVO_4 in the quasi-three level system at 914 nm, polarized pumping from both sides of the laser crystal achieved a maximum optical-to-optical conversion efficiency of 33.4 % [32], while in the four-level system at 1064 nm, the maximum optical-to-optical efficiency ever measured in CW operation was 60 % while a maximum slope efficiency of 66 % was recorded [105]. Additionally, in passive Q-switching, compared to CW operation, reduced conversion and slope efficiencies are still expected due to the saturable and non-saturable losses of the saturable absorber in the resonator. The direct influence of the saturable absorber on the conversion and slope efficiency has been investigated in the past for various systems [106, 107]. Here, for the Q-switching efficiency, which is defined as the ratio of passively Q-switched and CW conversion efficiency, a maximum value of nearly 85 % could be determined using a bulk saturable absorber [108]. In addition to bulk saturable absorbers, the continuous optimization and development of growth methodology in the past has made it possible to produce InGaAs quantum wells with extremely low non-saturable losses [109, 110]. These were used in a work by Huang

et al. 2007 to minimize the reduction in system efficiency due to the non-saturable losses of the saturable absorber and consequently obtain a Q-switching efficiency of 91 % [111].

While the insertion of a saturable absorber into the resonator not only introduces saturable and non-saturable losses, it also has a significant impact on the longitudinal mode structure, as well as the **mode selectivity of a passively Q-switched laser**. For low pump powers, only one longitudinal mode was observed, while more modes were added as the pump power increased [112, 113]. The etalon-like effect of a thin Cr^{4+}:YAG saturable absorber reduced the number of longitudinal modes significantly such that a spacing three times larger, compared to the theoretical mode spacing of the resonator, was observed [114, 115]. In further work, by using a thicker saturable absorber along with a Yb:YAG gain medium, the longitudinal mode spacing was only two times larger [116]. Even for relatively long resonator lengths, by introducing an additional tilted etalon [117] made of glass or by using a volume Bragg grating [107], the operation on a single longitudinal mode could be observed. Furthermore, in addition to the etalon-like reduction of the mode structure, it has been shown for passive Q-switching that the pulse buildup time of the longitudinal modes can be extended by the switching operation of the saturable absorber, which can additionally affect and reduce the number of modes [54, 118].

In passively Q-switched lasers, the **applied pump power** has a large influence on the various system quantities such as repetition rate, pulse duration, pulse energy, beam quality, or even stability properties of the laser. While in many theoretical considerations about the pump power only the repetition rate scales [58, 71], experimental studies have shown that the pump-induced heat has a significant influence on the crystal internal population densities [113], saturation properties [100], absorption properties [103] and the thermal lens [53, 119]. The thermal lens is proportional to the applied pump power which leads to the fact that

with increasing pump power both the overlap between pump and resonator mode changes but also the beam diameter and the divergence angle vary. As a result, output parameters such as conversion efficiency, pulse energy, and pulse duration change as a function of pump power [108, 113]. For a passively Q-switched laser, the maximum achievable repetition rate is typically limited by thermal effects, whereas the maximum value depends on many factors such as the laser crystal used, the pump spot diameter, or the saturable absorber. With saturable absorbers based on Cr^{4+}:YAG, maximum repetition rates of 190 kHz have been achieved in the past [112], which is close to the maximum, namely the inverse of the upper-state lifetime of ∼4 µs needed for the absorber to recover after the bleaching process. In contrast, the use of semiconductor structures with shorter upper-level lifetimes in the nanosecond range enabled passively Q-switched lasers with repetition rates in the megahertz regime [120–122]. While for lower pump powers above the threshold, the repetition rate usually scales linearly with the applied pump power [123], for higher pump powers nonlinear dynamics ranging from various period cycles to chaos have frequently been observed [114, 124–128]. Simultaneously, the occurrence of satellite pulses was frequently observed in this context [60, 129].

The **polarization of the laser emission** has an important role for many applications such as nonlinear frequency conversion [130], laser material processing [131], or certain spectroscopic techniques [132]. For this reason, the polarization properties of various solid-state laser crystals have been studied in the past. While solid-state lasers are usually linearly polarized, a distinction must be made here between different crystal materials. For isotropic laser crystals, such as Nd^{3+}:YAG, the preferred direction of laser polarization comes from resonator-internal polarization optics such as Brewster windows, or is determined by tiny differences in gain (e.g., strains in the crystal, crystal defects) or resonator losses (e.g., dielectric resonator mirrors) in the different polar-

ization directions [47]. However, small differences, in turn, lead to the problem that the linear laser polarization can rotate due to temperature [36] or it can depend on the polarization of the pump laser diode [133]. In contrast, Nd^{3+}:YVO_4 has an anisotropic crystal lattice with a strong birefringence resulting in a stable preferred direction of polarization even without any polarizing element in the cavity [134, 135]. This has been exploited in various works to realize an orthogonally linearly polarized laser [136–138] or by frequency doubling to obtain a linearly polarized green laser system [139, 140].

Moreover, the **cavity length dependencies** in passively Q-switched lasers have already been analyzed in various theoretical works based on rate equation models. It has been shown that the pulse duration depends linearly on the resonator round-trip time and consequently on the resonator length [141, 142]. In addition, the influence of the resonator length was studied experimentally in various works [143, 144]. It was found that a change of the resonator length not only changes the round-trip time and consequently the temporal pulse duration, moreover, the spot diameter in the gain medium and on the saturable absorber varies [145, 146]. In addition to this, it was found that for certain resonator lengths there is enhanced mode beating due to a coupled cavity effect, which could be assigned to different multiples of the free spectral range (FSR) of the resonator [147].

In addition to the initial transmission of the saturable absorber, the applied pump power, and the resonator length, the **output coupler reflectivity** plays an extremely important role for the output parameters of passively Q-switched lasers, both concerning the reflectivity and the radius of curvature. It has been shown in various theoretical investigations that a compromise must be made concerning the maximum achievable pulse energy, output power, peak power, and conversion efficiency, as well as the minimum achievable pulse duration and laser threshold [141, 148]. This in turn means that an optimal output coupler

reflectivity exists at which the different output parameters are fulfilled in sum in the best possible way. This relationship has been confirmed in experimental studies based on various laser crystals and saturable absorbers [58, 113, 149]. If the output coupler transmissivity is chosen to be low, a small laser threshold can be achieved, but insufficient power is outcoupled from the resonator so that the maximum intracavity power exceeds the laser-induced damage threshold, resulting in damage to optical coatings observed in several experimental studies [113, 143]. On the other hand, as the output coupler transmissivity increases, the resonator losses increase while the Q-factor decreases, leading to an increase in the pumping threshold [113, 149]. In this case, the maximum power cannot be formed in the resonator, resulting in reduced pulse energy and output power.

For applications, the laser should possess decent **stability of the output parameters**. Studies on the stability of the pulse build-up time, the pulse energy, the pulse duration, and the peak powers have shown that instabilities in passively Q-switched lasers can be significantly reduced by reducing mechanical vibrations [150]. Here, variations in the low single-digit percent range were found in both pulse energy, pulse duration, and peak power [106, 151]. In addition, it was shown that the reduction of the longitudinal mode number, e.g. by introducing an etalon into the resonator, may not lead to a general improvement of stability, but may also lead to degradation. It was shown that the gradual reduction of the mode number from four to two modes led to enhanced intensity fluctuations, due to an increase in mode competition and coupling of the modes [150]. In contrast, when the laser is operated on a single longitudinal mode, it was shown for an Er:YAG laser at 1645 nm in a measurement over 40 minutes that excellent stability can be achieved in terms of both average output power and wavelength stability [152]. As for the pulse-to-pulse amplitude fluctuations, very different stability values were measured for passively Q-switched systems, especially as

a function of the pump power. While for low and medium pump powers standard deviations in the mid-single-digit percentage range was obtained in different works [111, 153–155], for higher pump powers a significant increase of the pulse-to-pulse fluctuations with modulations of up to 20 % could be observed [106, 30].

Studies of the **temperature-dependency of output parameters** on quasi-three level systems based on Tm:YAG and Nd^{3+}:YAG have shown that with increasing temperature at the laser crystal, the pump threshold increases due to increasing thermal occupancy of the lower laser level [156, 157]. Furthermore, in a passively Q-switched Nd^{3+}:YAG laser at 1064 nm, the pulse energy could be increased by nearly 50 % over a range of 90 °C, which simultaneously brought a significant decrease in pulse duration due to the exponential build-up of the electric field in the cavity. In 2015, the temperature dependence in a passively Q-switched Nd^{3+}:YVO_4 at a repetition rate of 100 Hz was investigated by Nie et al. [158]. Here, an increase in pulse energy by a factor of 4.5 and a simultaneous decrease in pulse duration by a factor of 2.4 was observed, while the boundary temperature was increased from 26 °C to 113 °C. The temperature effect for a passively Q-switched Cr:Nd^{3+}:GSGG was investigated by Bass et al. using an analytical model and subsequently validated experimentally [159]. Hereby, an increase in pulse energy was also observed with increasing temperature and thus the temperature dependence of the stimulated emission cross-section was back-calculated. In a work by Xue et al. in 2017, the temperature effect of the saturable absorber and the laser crystal was studied separately over a temperature range from 0 °C to 170 °C [160]. With the increasing temperature at the Nd^{3+}:YVO_4 gain crystal, a decrease in average output power and concurrent efficiency was observed due to the decrease in stimulated emission cross-section at 1064 nm. For the same reason, a significant increase in pulse energy, as well as a simultaneous decrease in pulse duration, was observed. Separate temperature variation on the saturable

absorber based on Cr^{4+}:YAG resulted in an increase in initial transmission with increasing temperature and consequently an increase in pulse duration, as well as a decrease in pulse energy. In further studies on Nd^{3+}:YVO_4, an increase of the pulse energy and a simultaneous decrease of the pulse duration could also be recorded. The comparison with a theoretical model based on rate equations showed that, depending on the temperature, both a reduction of the emission cross-section and the appearance of higher modes must be taken into account to obtain agreement between experiment and theory [161]. The excitation of higher transverse modes with increasing temperature was based on an increase of the thermal lens and was also confirmed experimentally by the increase of the beam quality factor M^2.

The **temperature-dependent wavelength shift** has been studied in several papers in the past. In a work by Xing et al. the thermal shift of the $^4F_{3/2}$ to $^4I_{11/2}$ transition around 1064 nm was investigated in Nd^{3+}:YAG. Here, a redshift between 3.4 pm/K and 7.9 pm/K was measured for the different splittings of the Stark manifold [162]. In another publication, a thermal wavelength shift of 4 pm/K could be determined for a passively Q-switched ceramic Nd^{3+}:YAG/Cr^{4+}:YAG laser over a temperature range from 50 °C to 200 °C [163]. This value could be confirmed in a rough estimation by investigations on a passively Q-switched Nd^{3+}:YAG laser by Kimmelma et al. in 2008 [164]. Thereby, a redshift of 4.6 pm/K in the range of 40-300 K was found. Similarly, Nd^{3+}:YVO_4 was examined by Deélen et al. and an average shift of 3 pm/K in the range 15-80 °C for a 1064 nm CW laser was found [165]. Furthermore, this was also theoretically justified using a phonon-ion interaction model based on the Debye model. In contrast, a smaller average shift of 1.9 pm/K was measured by Sardar et al. in 2000 between 10-300 K [166], while a much larger value of 5.3 pm/K was determined for a microchip laser between 0 °C and 100 °C [167].

4.2 EXPERIMENTAL SETUP I - INSERTABLE SATURABLE ABSORBER

The first experimental investigations were performed using a resonator configuration in which it was possible to switch between CW operation and passive Q-switched operation by the insertion of a saturable absorber. Using this configuration, the influence of the saturable absorber on the overall efficiency and longitudinal mode selectivity was investigated. The schematic experimental setup is shown in Fig. 4.1. The employed pump laser (BWT Beijing Ltd - K808DA5FN-35.00W) was a 808 nm fiber-coupled semiconductor diode array with a fiber core diameter of 105 µm and a maximum output power of 35 W in continuous wave laser operation. The pump module has been fully characterized and the associated measurements are shown in Appendix 7.3. For the laser driver, a pulsed current source (Ostech ds11-la14v14) with a maximum output current of 14 A was used in QC mode at a duty cycle of 5 % (10 ms on time and a period of 200 ms). A Peltier element

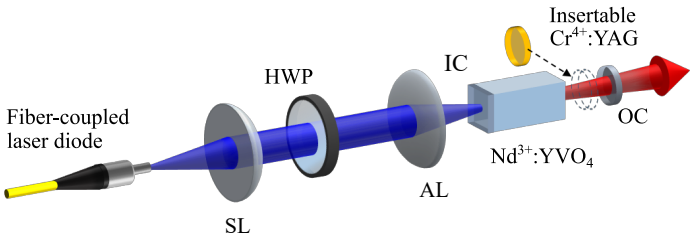

Figure 4.1: Experimental setup of the Nd^{3+}:YVO_4 laser with insertable Cr^{4+}:YAG saturable absorber to switch between CW and passively Q-switched operation. SL: spherical lens, HWP: half-wave plate, AL: aspherical lens, IC: input coupler, OC: output coupler.

(LAIRD Supercool PE-071-14-15) sandwiched between the package and a water-cooled heat sink was used to temperature control the laser. Consequently, the central wavelength of the laser could be tuned to the main absorption band of Nd^{3+}:YVO_4 at 808 nm and the system could be optimized during laser operation. The divergent pump light emerging from the fiber was collimated using a spherical lens (f = 20 mm) and then imaged to a spot diameter of 200 µm ($\sim 1/e^2$) in the gain medium with an aspherical lens (f = 37.5 mm). Because the pump fiber was not long enough, complete depolarization of the pump light did not occur. Therefore, a half-wave plate was placed between the two lenses and the preferred direction of polarization in the laser mode could be rotated to an optimum. For the gain medium, an a-cut 0.15 % at. Nd^{3+}-doped YVO_4 crystal ($3x3\,mm^2$ aperture, Casix) with a length of 5 mm was used. The crystal was thermally bonded to a water-cooled copper heat sink using 0.15 mm thick indium foil. The copper holder was custom-designed and fabricated to mount the crystal free of distortion while maintaining degrees of freedom for system optimization by combining it with a modified kinematic two-axis mount (Thorlabs KM100PM). With the help of this copper holder, the gain crystal could be tilted in both x and y directions to align the resonator. Figure 4.2 shows a schematic drawing of the custom-designed crystal holder based on a modified kinematic 2 axis holder. Further, the holder was temperature-controlled via the connections of the cooling water tubes.

The incoupling facet of the Nd^{3+}:YVO_4 crystal formed one of the two end mirrors of the linear resonator and was coated with a dielectric coating. In addition to high reflectivity at 914 nm (R>99 %), the coating was specified for high transmission at the pump wavelength (T>96 %, 808 nm) and low reflectivity at the parasitic lasing wavelengths (R<3 %, 1064 nm and 1342 nm). The second side was coated with an anti-reflection (AR) coating (R<0.6 %) for 914 nm, 1064 nm and 1342 nm. With a partial reflectivity of 92 % at the laser wavelength and an AR coating (R<0.6 %)

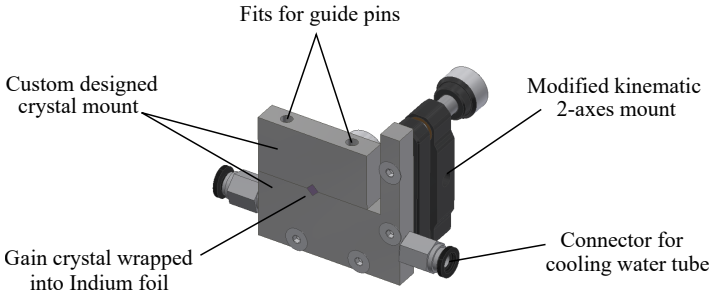

Figure 4.2: Schematic drawing of the custom-designed crystal holder based on a modified kinematic 2 axis holder. The holder is temperature-controlled via the connections of the cooling water tubes.

at 1064 nm and 1342 nm, the output coupler formed a linear planar resonator approximately 17 mm long. To switch between CW and passively Q-switched laser operation, a Cr^{4+}:YAG saturable absorber (AR coating R<0.6 % on both sides for 914 nm, 1064 nm, and 1342 nm) could be inserted into the resonator between the gain medium and the OCM. The absorber was glued along its edge to a thin copper disk and could also be tilted with a kinematic holder via an adapter plate to minimize the optical losses of the AR coating. In the subsequent experiments, an AR-coated saturable absorber with a specified initial transmission of 96 % at 914 nm was used. For all subsequent measurements, a duty cycle of 5 % (10 ms on time with a period of 200 ms) was used. Due to simplicity, all QC pump and output powers given were measured as average power and are given as such in this work. For conversion to the actual peak power in the QC pulse train, the specified values must be multiplied by a factor of 20.

4.2.1 Conversion and slope efficiency

The conversion efficiency of a CW laser is mainly determined by the internal resonator losses, the overlap between pump and resonator modes, the transmissivity of the OCM, and the quantum defect between pump photon and laser photon. In the case of a passively Q-switched laser, additional saturable and non-saturable losses of the absorber and possibly losses due to a non-ideal AR coating on the absorber surface are added. In this subsection, the influence of the saturable absorber on the laser performance is investigated. For this purpose, the average output power was investigated first without and subsequently with the saturable absorber at increasing pump power levels to investigate the direct influence of the absorber on the conversion and slope efficiency.
Figure 4.3 (a) shows the average output power as a function of the applied pump power for both CW and passive Q-switched operation. For the passive Q-switching, a Cr^{4+}:YAG saturable absorber with an initial transmission of 96 % at 914 nm was inserted into the resonator. First, the output power in CW mode was investigated as a function of pump power, where the measured values are represented by green dots. Therefore, the system was optimized at the beginning by iteratively adjusting the components to minimize the pumping threshold to a value of 175 mW. A slope efficiency of 47.7 % was determined by a linear fit (green dashed line) in the low pump power region. As the pump power increased, the output power first increased linearly and flattened somewhat from about 650 mW. This saturation behavior comes on the one hand from a thermal rollover effect, where the peak temperature in the crystal increases due to the increasing pump power. On the other hand, as the pump power increases, the thermal lens strength increases, and longitudinal mode competition occurs. At a pump power of 1000 mW,

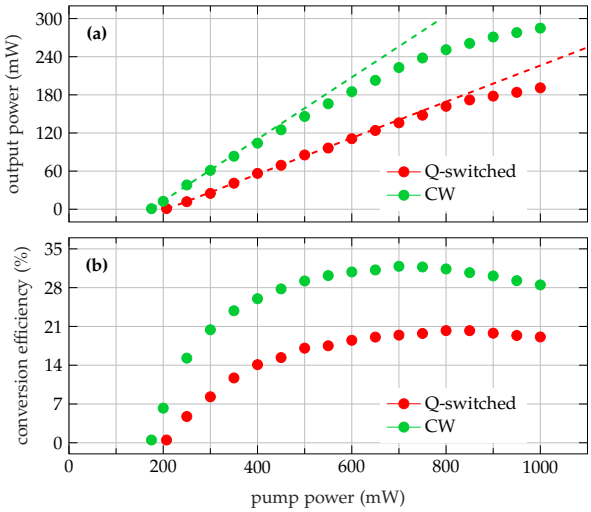

Figure 4.3: Comparison between the CW- and passively Q-switched operation concerning output power (a) and associated conversion efficiency (b). The experimental data is depicted as dots, whereas the linear fits to determine the slope efficiencies are shown as dashed lines.

the maximum output power of 285 mW was achieved, which corresponds to a conversion efficiency of 28.5 %. However, the maximum conversion efficiency of 31.8 % was achieved for a pump power of 700 mW, due to the before-mentioned effects. Compared to the literature, this is the second-highest conversion efficiency ever measured for a quasi-three level laser based on Nd^{3+}:YVO_4. The highest literature conversion efficiency of 33.4 % was obtained in 2016 by Jiang et al. for a double-end polarized pumped crystal setup [32]. Double-end pumping can significantly reduce the thermal load compared to single-end pumping. However, the small difference of just 1.6 % between single-side pumping and double-end pumping can probably also be attributed to the QC pumping process with a low duty cycle of only 5 %, which significantly

reduces the thermal load compared to continuous pumping.

As a next step, the saturable absorber was inserted into the gap between the gain crystal and the OCM. The corresponding experimental measured values for the output power and conversion efficiency are shown as red dots in Fig. 4.3. Compared to CW operation, a higher pump threshold of 207 mW was obtained for the passively Q-switched mode. In addition, the fitted slope efficiency decreased to 29.2 % and the maximum measured output power was only 191 mW. Analogous to CW operation, the output power increases linearly initially and then finally bends slightly for pump powers above 800 mW. The maximum conversion efficiency is reached for a pump power of around 800 mW and is 20.3 %. Both the higher pump threshold and the lower slope efficiency along with the conversion efficiency are due to the properties of the saturable absorber. On the one hand, a saturation of a spectral transition is necessary for the saturable absorber to switch through, but likewise, ESA reduces the efficiency. On the other hand, the absorber has an AR coating on both sides, which is specified by the manufacturer with R<0.3 % and introduces additional losses into the resonator. For homogeneously broadened crystals, such as Nd^{3+}:YVO_4, the maximum achievable slope efficiency is given by

$$\eta_s = \frac{T}{T+L}\frac{\lambda_p}{\lambda_l}\eta_c, \tag{4.1}$$

with the output coupler transmissivity T, the internal resonator losses L, and the respective pump and laser wavelengths λ_p and λ_l [168, 169]. In addition to this, the geometric coupling efficiency between the pump and resonator modes, as well as the saturation parameter of the gain crystal is considered by η_c. For a output coupler transmissivity of $T =$ 8 % (R 92 %), a pump and laser wavelength of 808 nm and 914 nm, assuming an ideal coupling efficiency and internal resonator losses of

3.5 %, a maximum slope efficiency of ∼61.5 % is obtained for CW operation. This value is significantly greater than the slope efficiency determined in the experiment, indicating that the mode coupling efficiency is far from ideal and the system still has great potential for improvement.
For a passively Q-switched laser, additional losses due to the saturable and non-saturable absorption of the absorber, as well as losses due to the AR coating, have to be considered. For this purpose, internal resonator losses of 9 % are assumed in a theoretical estimation, resulting in a theoretical slope efficiency of ∼ 41.6 % for an ideal mode coupling efficiency. Not surprisingly, the maximum possible slope efficiency is also significantly higher than the value achieved in the experiment, since the coupling efficiency has not changed due to the introduction of the saturable absorber.
For future experiments, both in CW and passively Q-switched operation, the coupling efficiency can be further improved and consequently, the slope efficiency can be increased.

4.2.2 Mode selection in passively Q-switched lasers

Depending on the application of the laser, single longitudinal or multi longitudinal mode operation is preferred. As a rough estimate of the longitudinal mode number, the gain bandwidth Δ_{ν_0} of the gain medium can be divided by the longitudinal mode spacing. Consequently, for a plane-parallel resonator of length L, the number of modes is given by

$$m = \Delta\nu_0 \left(\frac{c}{2nL}\right)^{-1}, \tag{4.2}$$

where c is the vacuum speed of light and n is the effective refractive index of the resonator. The longitudinal mode spacing is mainly de-

termined by the optical resonator length, although parasitic reflections from optical elements in the resonator can also strongly influence the selectivity of the longitudinal modes.

From Equation 4.2 it becomes clear that single longitudinal mode operation is technically possible only if the gain bandwidth of the crystal is quite narrow and the induced mode spacing is sufficiently large. The additive influence of an optical intracavity element is shown in Fig. 4.4. In Subfigure (a) the gain bandwidth is depicted as a red line, which for Nd^{3+}:YVO_4 typically has an FWHM of around 1 mm. Additionally, the resonant modes of a cavity with an exemplary length of 5 mm are shown as a blue line. Further, the transmission of a 0.5 mm thick intracavity element with different AR coating reflectances between 0.2 % and 0.05 % is shown in Figure 4.4 (b). Typically, such an element with an AR coating can be either the laser crystal or a saturable absorber in passive Q-switching. Depending on the reflection of the AR coating, there are different transmission amplitudes, which have a larger periodicity than the resonator modes due to the smaller thickness of the optical element. The superposition of both effects of subfigure (a) and (b) in combination with the limited gain bandwidth is shown in Figure 4.4 (c) as a red line. Thereby, the periodic transmission curve of the intracavity element in subfigure (b) causes additional losses for some of the longitudinal resonator modes from subfigure (a), so that these modes are unable to oscillate in the subsequent laser operation due to insufficient gain. In addition, the spectrally limited envelope of the gain bandwidth causes the amplitudes of the remaining modes to drop from the maxima to the outside. As a result, the number of longitudinal modes compared to the free-running laser is reduced. In the following, CW operation is directly compared with passively Q-switched operation by inserting a saturable absorber of a certain thickness to investigate mode selectivity and to estimate the potential of a single-frequency laser. Similar to the last experiment a pump duty-cycle of 5 % was used to reduce overall heat

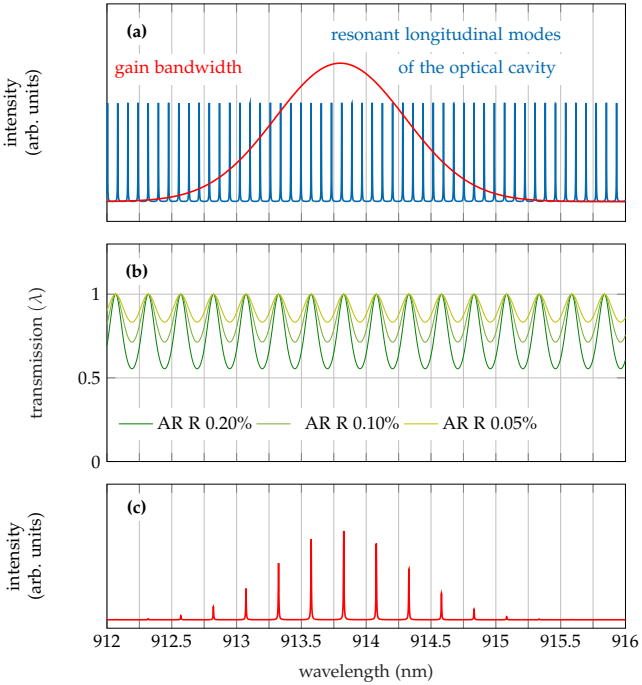

Figure 4.4: Theoretical consideration of the longitudinal mode selectivity of a fictitious laser with a gain bandwidth of approximately 1 nm. The gain bandwidth of the laser crystal (red line) and the resonant longitudinal modes of the cavity (blue line) are shown in (a). In (b) the transmission of an optical element with different AR coatings is shown, while in (c) the resulting spectrum of the laser is shown as a superposition of (a) and (b). The illustration is adapted from [115].

load and to make the measurement transferable to later applications. The spectrum was analyzed using an optical spectrum analyzer with a resolution of 2 pm (LightMachinery Hyperfine HF-8991-3). Figure 4.5 (a) shows the output spectrum of CW operation at a pump power of 540 mW which equals 3 $\times$ the threshold pump power. The laser was oscillating on a variety of longitudinal modes with an average mode

separation $\Delta\lambda$ of $\sim$35.4 pm. Further, due to the logarithmic scaling of the y-axis even small spectral features were observable. A split of the spectrum into several separated parts was obtained whereas most longitudinal modes contributed to the main part at around 913.9 nm and few longitudinal modes to the side wing at around 913.5 nm, 914.4 nm, and 914.6 nm. The missing longitudinal modes between the main part and side wings suggest a separation due to further parasitic intracavity reflections. With a spacing of roughly 1.3 nm free spectral range (FSR) this might be linked to an optical resonator length of around 320 µm. The asymmetric distribution of modes indicates the shape of emission bandwidth. A similar asymmetry has been observed for Yb:YAG due to an asymmetrical emission band around 1032 nm [114].

According to Equation 4.2, a mode separation of 42.5 pm and 34.8 pm is expected due to a 5 mm long Nd^{3+}:YVO_4 crystal ($n = 1.9647$ [89]) and the 12 mm air spacing between the Nd^{3+}:YVO_4 crystal and output coupler mirror, respectively. Furthermore, the plane-parallel composite cavity (5 mm Nd^{3+}:YVO_4 and 12 mm air gap) induces theoretically a mode spacing of 19.1 pm. Comparison between experimental measurements and theoretical investigations suggests that the longitudinal modes are mainly determined by superimposition effects of the Nd^{3+}:YVO_4 crystal and air gap inside the resonator. A mode spacing due to the composite cavity was not observed directly. Post analysis of the spectrum using Matlab revealed two different kinds of spectral linewidths (FWHM) of around 3.0 pm and 5.5 pm. The large variation probably arises from higher transversal modes or non-linear mode coupling between single modes.

To investigate the passively Q-switched spectrum a Cr^{4+}:YAG saturable absorber (Casix) with an initial transmission of 96 % was inserted in the cavity similarly to the experimental setup in Figure 4.1 without adjusting the pump lenses or the cavity length. Analogously to the previous investigation of conversion and slope efficiency in Subsection 4.2.1, a

kinematic mounting of the absorber enabled optimization concerning the Q-switched operation threshold. The absorber had a thickness of 0.19 mm and a refractive index of $n = 1.8180$ [170] which induces a theoretical mode spacing of 1209.3 pm.

Figure 4.5 (b) illustrates the spectrum of passively Q-switched operation at a pump power of 625 mW which equaled $3\times$ the passively Q-switched threshold power. Compared to CW operation, a clear reduction in the number of longitudinal modes was observed in passive Q-switched operation and the laser was oscillating stable on only three longitudinal modes.

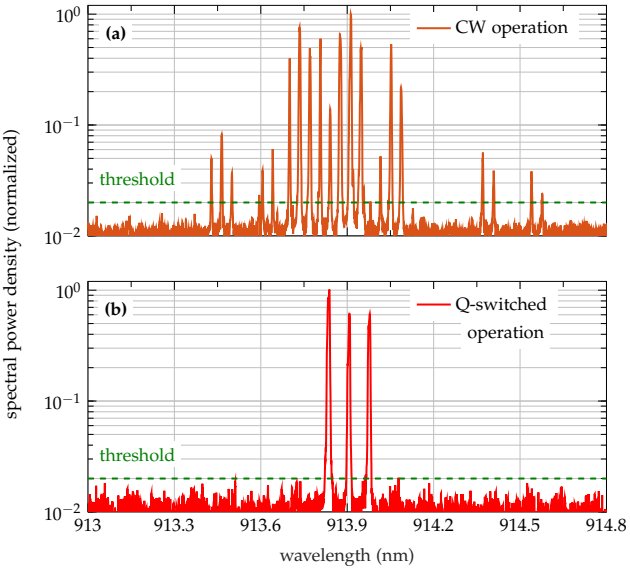

Figure 4.5: Comparison of the longitudinal mode number between CW-operation in (a) and passively Q-switched operation in (b) by insertion of a saturable absorber into the resonator.

The longitudinal modes were evenly spaced with a calculated distance of around 113 pm. This mode spacing can not be explained with the thickness of the saturable absorber rather it is linked to an etalon with an optical thickness of 3.7 mm. Closer observation of the optical setup and its spacing led to the assumption that this might correspond to the distance between the crystal and the output coupler mirror. This would imply that the AR coating of the saturable absorber is not sufficiently good to suppress the etalon-like effect of the output coupler mirror and absorber coating.

Previous measurements showed clearly that the selectivity of longitudinal modes is significantly enhanced by the insertion of a saturable absorber inside the cavity. Although the physical cavity length was approximately 20 mm the passively Q-switched laser was oscillating on only a few longitudinal modes. In comparison, for CW-operation, a variety of longitudinal modes with similar amplitudes was observed. The selectivity of modes occurred due to an etalon effect of different optical interfaces.

Subsequent investigations of a microchip laser in Chapter 5 emphasize this assumption as single longitudinal mode operation was observed easily.

4.3 EXPERIMENTAL SETUP II - BONDED CRYSTALS

The second resonator configuration has the gain medium bonded directly to the saturable absorber. With this configuration, the influence of the applied pump power was investigated. In addition, the polarization of the generated laser light was analyzed and the effects of the resonator length, as well as the influence of the reflectivity of the OCM, were determined. Furthermore, a long-term stability measurement of the output parameters over 60 minutes was performed.

Figure 4.6 shows a schematic view of the experimental setup in the second resonator configuration. Compared to Experimental Setup I, the only changes are that the gain medium and the saturable absorber are no longer discrete, while the pump laser and the pump optics used remained the same. The Cr^{4+}:YAG saturable absorber is now directly bonded to the Nd^{3+}:YVO_4 gain crystal in this setup, however, the specifications remained the same. This configuration not only simplifies the alignment in the experiments but also eliminates the need for two AR coatings between the two crystals. The specifications of the resonator

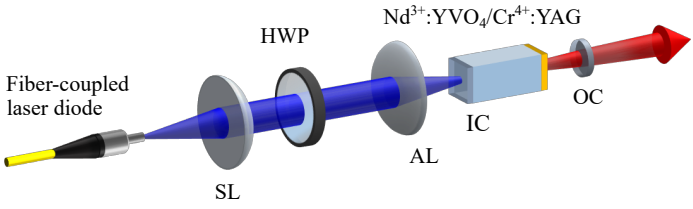

Figure 4.6: Experimental setup of the passively Q-switched laser with the Nd^{3+}:YVO_4 crystal bonded to the Cr^{4+}:YAG saturable absorber. SL: spherical lens, HWP: half-wave plate, AL: aspherical lens, IC: input coupler, OC: output coupler.

coating on the input side and the OCM have also not changed. Since a QC pulse mode was used for all subsequent measurements, all associated powers were measured as continuous values and are reported as such in the subsequent experiments. This means that the displayed values include the pause between the QC pulse trains in which the laser was running. Taking into account the duty cycle, the actual power applied in the pulse train can be calculated. For all subsequent measurements a duty cycle of 5 % (10 ms on time with a period of 200 ms) was used. Due to simplicity, all QC pump and output powers given were measured as average power and are given as such in this work. For conversion to the actual peak power in the QC pulse train, the specified values must be multiplied by a factor of 20.

4.3.1 Pump power investigations and instabilities

The applied pump power is an important control parameter for passively Q-switched lasers since it determines how fast the necessary occupation inversion builds up for switching the saturable absorber and consequently determines the repetition rate. In addition to the time required to build up the population inversion, the absorbed pump light leads to a thermal loading in the gain crystal, resulting in a thermal lens due to the temperature-dependent refractive index. This thermal lens is an important parameter, especially for plane-parallel resonators, because it contributes to the stabilization of the resonator.In the following, simulations of the pump power influence on the thermal lens are carried out and subsequently compared with experimental data. Further, the influence of the pump power on the longitudinal mode number and the resulting effects on the laser system are considered.

Simulations for the pump induced thermal lens

Based on the matrix formalism-based stability simulations from Chapter 3, the influence of the thermal lens induced by the pump power was investigated. Figure 4.7 (a) shows the stability diagram of a plane-parallel resonator. Hereby, the green lines represent the edge of the stability zones, while the blue dot corresponds to a plane-parallel resonator without a thermal lens. A thermal lens shifts the stability point of the plane-parallel resonator along the red dashed line. Consequently, the thermal lens in the resonator can be stabilizing (white area), but can also make the system unstable (gray area). Figure 4.7 (b) shows the thermally induced dioptric power and focal length as a function of pump power based on Equation 2.14. For the calculation, the constants from Section 3.4 and a pump waist diameter of 200 µm were chosen.
An incident average pump power in the range between 0 and 1200 mW was applied which equaled a recalculated peak power between 0 and 24 W at a duty cycle of 5 %. With increasing pump power, the refractive power increases strongly at the beginning and approaches the x-axis asymptotically.

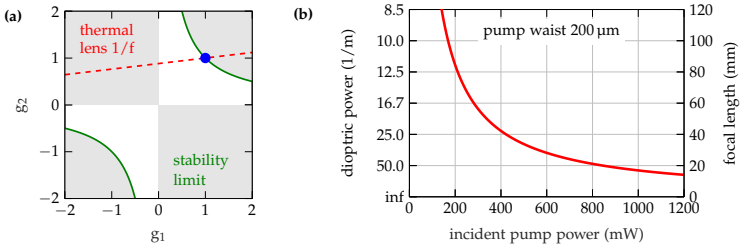

Figure 4.7: Simulations of resonator stability and thermal lensing. (a) Resonator stability diagram and stability limit (green line) without the effect of the thermal lens (blue dot) and with shift due to the influence of thermally induced lens (red dashed line). (b) Dioptric power and focal length of the thermal lens which is induced due to the applied pump power.

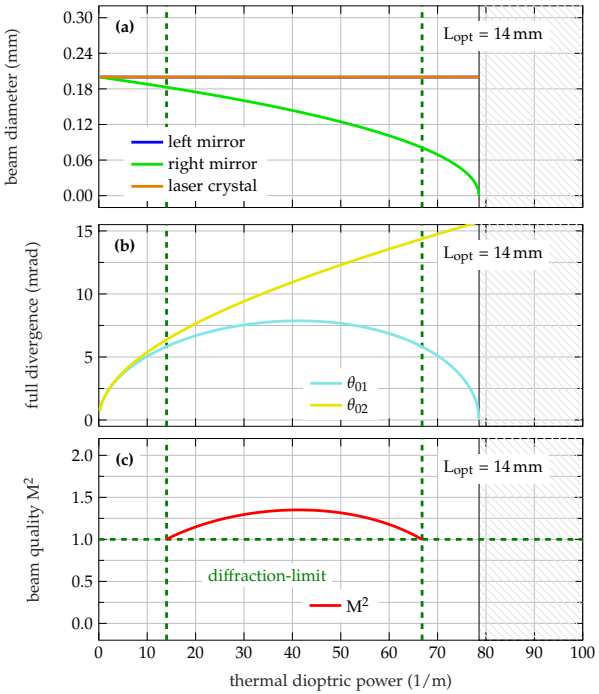

Figure 4.8: Simulation results of resonator stability as a function of thermal refractive power based on the matrix formalism. For the simulations, a cavity length of 14 mm was chosen, while the gray shaded area represents the zone outside of stability. (a) shows the beam diameter at the left and right mirrors, as well as the laser crystal. Hereby, the orange and blue lines are directly above each other and thus the blue line is hardly visible. The full divergence angle is shown for the two regions left and right of the thermal lens in (b). Figure (c) shows the beam quality including the diffraction limit for Gaussian beams as a dashed green line.

The simulation results of the resonator stability as a function of the thermal lens are shown for a resonator length of 14 mm and a pump spot diameter b of 200 µm in Figure 4.8 (a)-(c). For a crystal length of 5 mm, the distance of each principal plane from the rod end is $h \approx 1.27$ mm

(see 3.16 in Section 3.3). Since it can be concluded from Figure 4.7 (b) that the dioptric power of the thermal lens for pump powers ranging from around 200 mW (threshold power) up to 1200 mW will be in the range of approximately $12\,m^{-1}$ and $71\,m^{-1}$ (equivalent to a thermal focal length of around 84 mm to 14 mm), only the left part of the two stability ranges (see Section 3.3) will be discussed here. In the graphs, the gray shaded area marks the area outside the region of stability. The green dashed line further restricts the possible range of the thermal lens, since an M^2 below 1 makes no sense from a physical point of view (see Figure 4.8 (c)). The beam diameter at the left and right mirrors, respectively, as well as the laser crystal, is shown as a function of the thermal refractive power in (a). Hereby, the orange and blue lines are directly above each other and thus the blue line is hardly visible. For a thermal refractive power between $14.0\,m^{-1}$ and $66.8\,m^{-1}$, the beam diameter at the left mirror and in the laser crystal remains constant at 200 µm because the thermal lens is formed at this point. In contrast, the beam diameter at the OCM (right mirror) decreases with increasing dioptric refractive power. This means that the spot diameter on the saturable absorber also changes with increasing pump power.

The divergence angle of the two simulated beam tallies on the left (θ_{01}) and right (θ_{02}) of the thermal lens is shown in (b). Since the laser beam is coupled out of the resonator to the right of the laser crystal, the angle θ_{02} corresponds to the full divergence angle of the outcoupled laser light. As the refractive power of the thermal lens increases, within the physically reasonable range (green dashed lines), the full divergence angle increases from 6.4 mrad at $14\,m^{-1}$ to 14.4 mrad at $66.8\,m^{-1}$.
The simulated multimode beam quality as a function of thermal refractive power is shown in (c). As mentioned earlier, the green horizontal dashed line marks an M^2 of 1 which corresponds to a diffraction-limited Gaussian beam. Although theoretically, a thermal lens between $0\,m^{-1}$

to 78.5 m^{-1} leads to a stable resonator the only physically meaningful range is the one with an $M^2 \geq 1$. Thus, the range in which the thermal lens can extend is limited by the green lines from 14 m^{-1} to 66.8 m^{-1}. In this range, M^2 initially increases slightly to a value of 1.35 and then decreases to 1 again with increasing refractive power. The beam quality remains very good throughout the range and changes only slightly because the decreasing beam diameter at the output coupler in (a) and the increasing divergence angle in (b) almost compensate each other.

Experimental results and comparison with simulations

In the following, experimental investigations were carried out and compared with the previous simulations. Figure 4.9 shows the experimental measurement of the full divergence angle (a) and the beam quality (b). The measurements were performed with a beam quality analyzer (Ophir BeamSquared SP920) and the recorded beam in x- and y-direction is shown as red and blue dots, respectively. Like already shown in the simulations, the divergence angle increased from about 5.4 mrad to 13.0 mrad with rising pump power. This increase results from the increasing refractive power of the thermal lens. Equation 2.14 was used to convert the thermal dioptric power from the simulations into pump power and the associated angle θ_{02} from Figure 4.8 (b) is shown dashed in gray. The experimental measurements and their behavior agree very well with the simulations, indicating that the modeled thermal lens replicates the experiments quite well. The experimentally measured beam quality is shown in (b) and deteriorates with increasing pump power from a diffraction-limited beam to an M^2 of 1.7. Considering the requirements defined in Chapter 1 Introduction, this value is quite sufficient to realize a lidar sensor with high lateral resolution. Up to about 600 mW QC pump power, the simulation (gray dashed line) agrees very well with the experiments, while above this pump power a

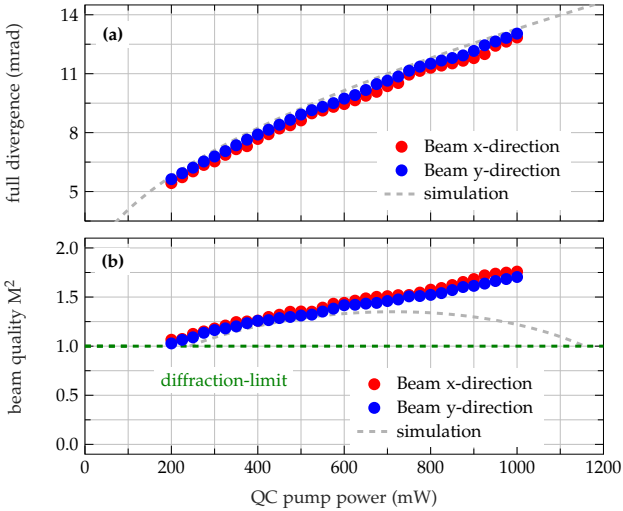

Figure 4.9: Experimental investigation of the divergence angle and beam quality factor M^2 in x- and y-direction (red and blue dots), as well as the respective comparison with the simulations based on the matrix formalism for resonator stability analysis (gray dashed line).

discrepancy arises. This difference may be due to the increase of longitudinal modes for higher pump powers, which is shown in Figure 4.16 and will be discussed later.

The experimental output parameters of the passively Q-switched laser concerning pump power, as well as simulations using the rate equation model from Section 3.1 of Chapter 3 are shown in Fig. 4.10. The constants used in the simulations are listed in Tabular 3.1.

In Figure 4.10 (a) the average output power (yellow dots) and the conversion efficiency (green dots) are plotted. Starting at a pump threshold of 195 mW, the output power initially increased almost linearly, reaching a maximum value of 146 mW at an applied pump power of 1000 mW. In addition, a value of 42.8 % was determined for the experi-

mental slope efficiency.

For a output coupler transmissivity of 8 % (92 % OCM) and 3 % intrinsic resonator losses, a maximum slope efficiency of 47.2 % is theoretically possible according to Equation 4.1. Thereby, additional losses of 4 % due to the saturable absorber (T_0 = 96 %) and an ideal geometric coupling efficiency were assumed. The comparison between the mea-

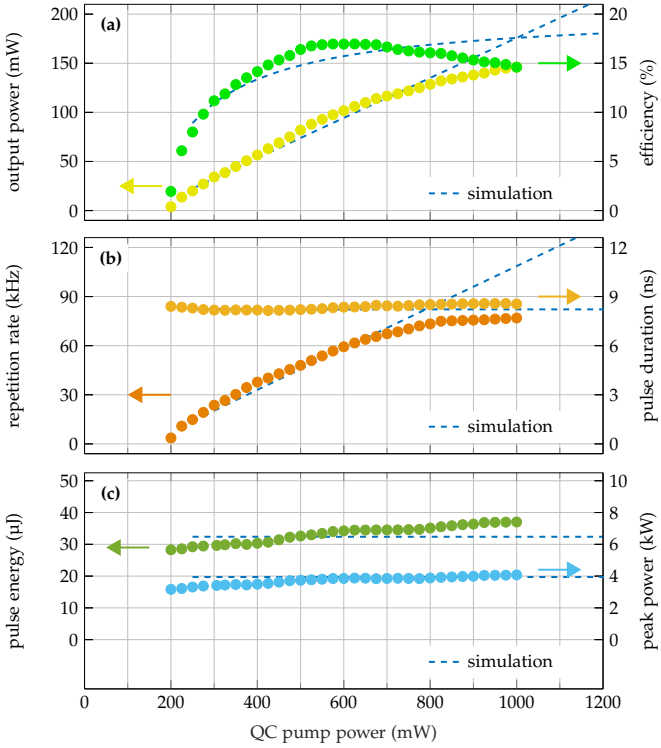

Figure 4.10: Experimental investigation of laser output parameters as a function of applied QC pump power. (a) shows the output power and conversion efficiency. The repetition rate and pulse duration are depicted in (b), while (c) shows the pulse energy and calculated peak power.

sured and the maximum calculated slope efficiency reveals that the coupling efficiency was actually around 90.7 %.
The simulation results (blue dashed line) reproduce the behavior of the average output power very well with an obtained threshold value of 190 mW. Above the threshold, a linear increase with increasing pump power was calculated for the average output power.

In the experiment, the conversion efficiency (green dots) initially increased rapidly, reaching a maximum of 17 % at an applied pump power of 575 mW. For larger pump powers, a saturation and subsequently a renewed drop in efficiency to 14.6 % was noted. On the one hand, this behavior can be explained by thermal over-rolling, in which the gain medium heats up due to the applied pump power. Finite element simulations in Section 3.4 have shown that the peak temperature in the gain medium heats up from about 42 °C at 200 mW to 150 °C at 1000 mW. This reduces the stimulated-emission cross-section and shortens the lifetime of the upper excited state. In addition, for quasi-three level lasers, the thermal population increases, leading to a reduction of ions participating in the laser operation and increasing the reabsorption of laser photons. On the other hand, the reduction of the optical-optical efficiency could additionally result from a complete depletion of the ground state population of Nd^{3+}:YVO_4 due to the reduced thermal occupation of the ground state and the high pump intensity. Later on, it is shown that for higher pump intensity, longitudinal mode competition and satellite pulses also play a crucial role, which may also affect the conversion efficiency.
Furthermore, as already shown in Figure 4.9 the beam quality factor M^2 deteriorates with increasing pump power, which is associated with the occurrence of higher transverse modes and also reduces the overlap between the pump mode and resonator mode. Overall, however, the maximum conversion efficiency of 17 % is a comparatively good value for

a passively Q-switched laser and by considering the quasi-three level system.
For the investigation of repetition rate, pulse duration, pulse energy, and peak power, which are shown in Figures 4.10 (b) and (c), the pulse train analysis according to Appendix 7.2 was used. With the help of this method, important insights into longitudinal mode competition and satellite pulses could be found.

The repetition rate as a function of the applied QC pump power is shown in Figure 4.10, where the dark orange dots correspond to the mean repetition rates determined with the pulse train analysis. Starting from the laser threshold, the repetition rate increased almost linearly to 63.9 kHz at a pump power of 650 mW. This corresponds to an approximate increase of 14.1 kHz/100 mW. Above 650 mW, first, a smaller slope to 73 kHz at 800 mW and then a transition to saturation could be observed. At 1000 mW the maximum value of 76.9 kHz could be determined. From threshold to about 650 mW, the simulations (blue dashed line) reproduced the experimental findings well with a slope of 12.6 kHz/100 mW. Above 650 mW, however, an increasing deviation between the simulations and experimentally determined values could be observed.
A closer look at the pulse train revealed an increasing occurrence of satellite pulses above a pump power of 650 mW. An exemplary recording of a satellite pulse can be seen in Figure 4.11 for an applied pump power of 900 mW. In this case, the time axis was shifted by 5 ms to display clearer values from 0 ns to 300 ns. The main pulse showed a duration of 7.53 ns (FWHM), while the satellite pulse exhibited 24.69 ns with a separation of approximately 69 ns from the main pulse.
It is important to note that the experimentally obtained repetition rate shown in Figure 4.10 does not include the satellite pulses in the post-processing analysis of the pulse train, and only the main pulses are

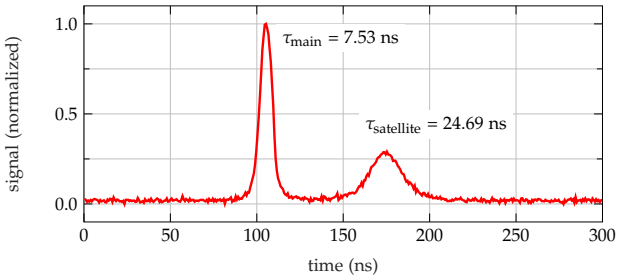

Figure 4.11: Exemplary recording of a main and satellite pulse for an applied pump power of 900 mW. In this case, the time axis was shifted by 5 ms to display clearer values from 0 ns to 300 ns. The main pulse has a pulse duration of 7.53 ns (FWHM), while the satellite pulse possesses a duration of 24.69 ns (FWHM).

represented. For a more accurate analysis of the satellite pulses, the post-processing analysis method was modified and the threshold for detection of pulses was reduced to additionally monitor the satellite pulses.

For a more detailed analysis for the occurrence of satellite pulses, the recorded pulse trains at 400 mW and 1000 mW pump power were analyzed using the adapted post-processing method with a reduced threshold value.

Figure 4.12 shows the repetition rate analysis of the pulse trains at 400 mW (red dots) and 1000 mW (blue dots) QC pump power. The occurrence of satellite pulses can be made visible with the aid of a post-processing pulse train analysis. Hereby, the temporal pulse spacing is determined and inverted. The resulting frequencies allow a proper distinction between main and satellite pulses. While repetition rates between a few Hz up to the order of several 100 kHz are typically achievable for passive Q-switching [47], the occurring frequencies for satellite pulses are significantly higher. Satellite pulses are typically spaced from the main pulse in the low two-digit to mid-triple-digit nanosecond range, resulting in a frequency in the MHz range.

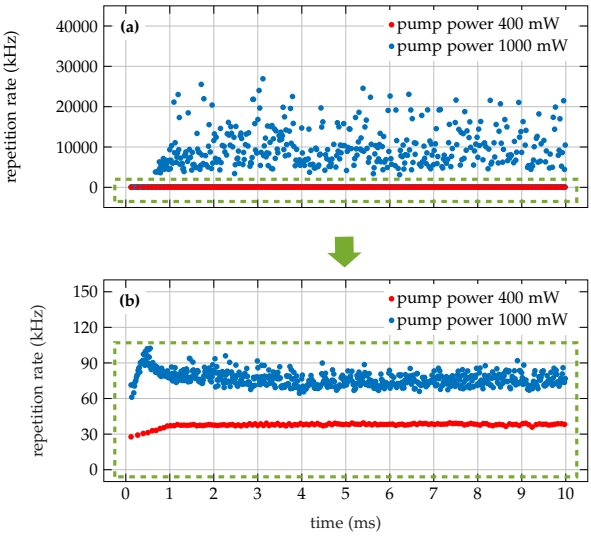

Figure 4.12: Comparison of the repetition rates of two pulse trains at an applied pump power of 400 mW and 1000 mW. The complete frequency range of the repetition rate is shown in the megahertz regime in (a), while (b) gives a zoom-in on the green dashed box into the sub-megahertz range.

In (a), an overview of the two pulse trains overall detected repetition rates up to 45 MHz is shown. For an applied pump power of 400 mW, no satellite pulses could be observed in the post-processing and the successive pulses were well below the megahertz regime. Consequently, in this view, kilohertz repetition rates seem to be located directly on the x-axis. In contrast, for a pump power of 1000 mW, a clear splitting of the repetition rate into two regions could be observed. First, in analogy to the lower pump power, there is a portion in the sub-megahertz range, but also a large smeared portion in the double-digit megahertz regime. The smallest observed distance between the satellite pulses and the main pulse was 37 ns, which corresponds to a repetition rate of 26.92 MHz. On the other hand, the largest distance was evaluated to be

320 ns linked to a repetition rate of 3.13 MHz. The majority of the satellite pulses showed a spacing between about 80 ns and 300 ns equivalent to repetition rates between 12.5 MHz and 3.3 MHz, respectively.

To get a more detailed overview of the kilohertz regime, the area indicated by the green dashed box is shown enlarged in Figure 4.12 (b). For the pulse train with a pump power of 400 mW, it was observed that the laser is in a steady-state after a short transient period of about 1 ms. In this steady-state regime the pulses exhibited a very stable repetition rate of 38 kHz with a standard deviation of 0.64 kHz (= 1.68 %). For a pump power of 1000 mW, a kind of steady-state operation was also observed after one millisecond. However, the average repetition rate was calculated to be 3.91 MHz as the satellite center pulses were taken into account. In addition, a significantly larger standard deviation of 5.76 MHz was obtained, which corresponded to a deviation of 147 %. By only considering the fundamental kHz range of the split regime, the mean repetition rate was measured to be 76.9 kHz with a standard deviation of 6.3 kHz (8.2 %).
As already mentioned at the beginning, for a better overview of the development of the repetition rate, only the fundamental kilohertz repetition rate is shown in Figure 4.10 when neglecting the satellite pulses. Interestingly, satellite pulses did not occur immediately with the transient of the pulsed laser, but only after about 50 pulses, which is equivalent to a time duration of about 0.7 ms. In addition, similar to the lower pump power, an increase in repetition rate was observed initially up to a time of about 0.5 ms. Unlike at 400 mW pump power, however, no equilibrium was reached after the increase, but rather the repetition rate decreased after the maximum of about 110 kHz and then reached a kind of equilibrium at nearly 80 kHz with additionally occurring satellite pulses. The initial increase after the pump power is turned on is a common process in passively Q-switched lasers, since equilibrium in

the laser dynamics is reached only after a few pulses. Here, the pumping power, which leads to an increase of the occupation inversion in the laser crystal, competes with the switching through of the saturable absorber and the subsequent reduction of the inversion by the build-up of a laser pulse. The sudden decrease of the repetition rate after reaching the maximum suggests a significant temperature rise in the gain medium due to the applied pump power. Consequently, this temperature rise leads to a reduction in the lifetime of the upper laser level, the reduction in the stimulated emission cross-section, and the increase in thermal occupancy in the lower laser level of the quasi-three level system. This makes the system more inefficient and reduces the repetition rate until thermal equilibrium is reached.

A possible reason for the occurrence of satellite pulses could be explained by a too high remaining gain in the gain medium after the build-up of the laser pulse (see possibility ① in Subsection 2.3.2) combined with the limiting upper-state lifetime of the Cr^{4+}:YAG saturable absorber. Due to the high pump power applied, a population inversion is reached very quickly in the gain medium, which ultimately leads to the switching of the saturable absorber. As the gain is very high due to the high population inversion, a second adjacent mode can still be built up by the remaining gain after reduction by the first longitudinal mode. However, this is only possible if the remaining gain is above the threshold and the difference in the build-up time of the two modes is not too big.

Due to the high applied pump power, the population inversion required to switch the saturable absorber is reached faster than it can recover through the fluorescence of the upper-state lifetime. Consequently, the subsequent pulse has an effectively reduced initial transmission and only a lower population inversion could be established in the gain medium compared to the previous situation. Thus, this time the remaining gain is not sufficient for an adjacent longitudinal mode to build up.

However, in the subsequent cycle, the saturable absorber is fully recovered again because of the lower initial transmission, and consequently, a higher occupation inversion can be achieved in the gain medium. Thus, the whole process repeats itself all over again.

Furthermore, it was evaluated in Figure 4.12 for a pump power of 1000 mW that after reaching steady-state operation above one millisecond, the number of satellite pulses was found to be 412, while at the fundamental repetition rate 646 pulses were generated in the pulse train. Closer examination of the sequences of pulses for this and other pumping rates with satellite pulses showed that the passively Q-switched laser sometimes possesses chaotic dynamics. Each fundamental pulse is followed by a satellite pulse, which corresponded to a period-doubling process (P2 cycle), since for attractors in the phase space a closed trajectory arises after two revolutions and the system is again in the initial state [171]. Analogously, various forms of limit cycles were observed, where a periodic number of pulses led back to the initial state.
Figure 4.13 (a) and (b) depict two exemplary recorded pulse trains where a P2 cycle and P3 cycle have been observed within a certain time interval. The sequence of a pulse train shown in (a) was recorded at a QC pump power of 750 mW and shows a P2 Cycle, where each pulse with a larger amplitude is followed by a pulse with a smaller amplitude. After two consecutive pulses, the system returned to the initial state and the process was repeated. In comparison, an exemplary sequence of a pulse train is shown in (b), where the system is back in the initial state after three consecutive pulses (P3 cycle). This pulse train was recorded at a pump power of 775 mW. In this case, a laser pulse with a small amplitude is followed in each case by two pulses with almost identical amplitudes, whereby that of the second pulse is always slightly higher than that of the first. Both the P2 and P3 cycles were stable in time and could be observed on the oscilloscope for successive pulse trains. The

attractors of the system in this case are the population inversion in the gain medium and the population of electrons in the excited state of the saturable absorber. Similarly, for other passively Q-switched lasers, chaotic systems and different PN and limit cycles have been observed [128, 172, 173].

Besides the repetition rate, Figure 4.10 (b) shows the pulse duration for different QC pump power levels. Analogous to the repetition rate, only the main pulses are displayed here, neglecting the satellite pulses. For the main pulses at the fundamental repetition rate, pulse durations (FWHM) between 8.15 ns and 8.57 ns were found by evaluating the post-processing pulse train analysis. The simulations, based on the rate equations, show good agreement with the experimentally deter-

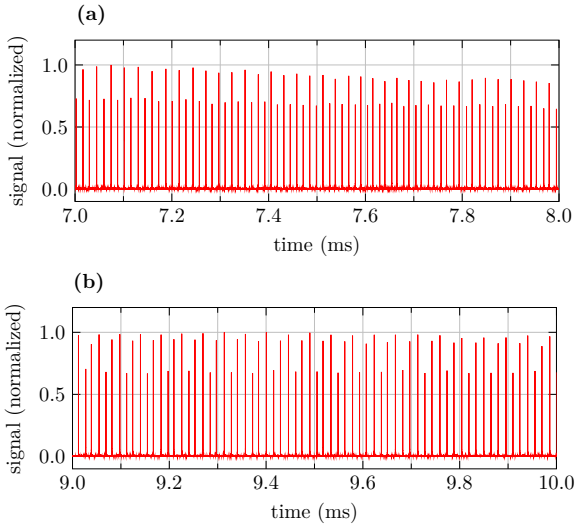

Figure 4.13: Chaotic dynamics of the passively Q-switched laser using exemplary pulse trains. Figure (a) shows period-doubling (P2 cycle) at an applied pump power of 750 mW, while (b) shows a P3 cycle at 775 mW.

mined values with a constant calculated pulse duration of 8.22 ns. Since in the rate equations the saturable absorber always switches through in an idealized manner, it is to be expected that the pulse duration does not depend on the applied pump power. For a more detailed analysis of the pulse duration of the main and satellite pulses, the pulse train was subsequently examined using the adapted post-processing algorithm. Figure 4.14 shows the evaluation of the pulse trains at a pump power of 400 mW (red dots) and 1000 mW (blue dots). At the lower pump power, no satellite pulses were observed and the mean calculated pulse duration was 8.17 ns with a standard deviation of 0.08 ns (1.04 %). In contrast, at 1000 mW, two pulse duration regimes can be clearly distinguished. Investigations showed that the lower branch could be assigned to the main pulses and the upper part to the satellite pulses. Considering the satellite pulses, the mean total pulse duration was found to be 11.89 ns with a standard deviation of 6.80 ns (57.19 %). Neglecting the satellite pulses, the mean value of the main pulse duration was calculated to be 8.54 ns at 1.07 ns std. (12.54 %). While the pulse duration of the main pulses varies only slightly, the large variations of the satellite pulses might be explained by the high variation of the remaining gain after the main pulse was extracted. If the remaining gain is above the thresh-

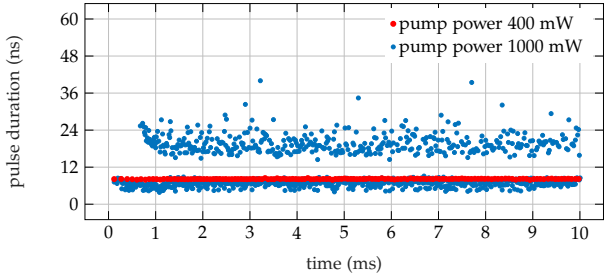

Figure 4.14: Comparison of the pulse duration of two pulse trains at a pump power of 400 mW and 1000 mW.

old, theoretically a pulse with larger energy follows, which in turn is expected to result in a shorter pulse duration. On the other hand, if the remaining gain is smaller and above the threshold, a satellite pulse with smaller energy and consequently a longer pulse duration is likely to follow. Whether a satellite pulse occurs and how large its pulse energy and pulse duration is, ultimately depends on the dynamics of the system.

The investigation of the pulse energy and the calculated peak power is shown in Figure 4.10 (c). In the graph, only the main pulse energies are shown and the satellite pulses are not considered. As the pump power increases, the pulse energy of the main pulses increases from an initial value of 28.28 µJ to 37.02 µJ. A possible reason for this increase could be the excitation of higher transverse modes, which results in an extension of the beam diameter. Due to the higher transverse modes, the beam quality factor M^2 in Figure 4.9 deteriorates. The simulation results based on the rate equations give a constant pulse energy of 32.38 µJ for all pump powers and thus agree well with the average of the experimentally determined values. However, the simulations do not account for the excitation of higher transverse modes and beam quality.

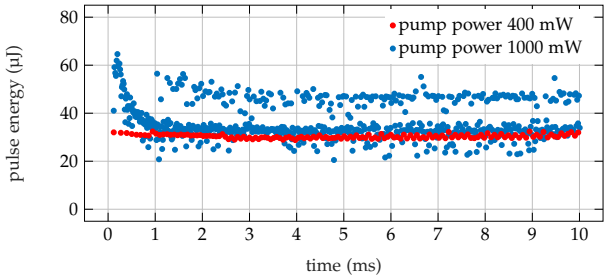

Figure 4.15: Comparison of the pulse energy of two pulse trains at a pump power of 400 mW and 1000 mW.

Analogous to the repetition rate and pulse duration, the pulse energy was investigated using the adapted post-processing method for a pulse train at 400 mW and 1000 mW QC pump power. The results are shown in Figure 4.15 as red and blue dots. For the low pump power level, no satellite pulses have been obtained and the mean pulse energy was 30.35 µJ with a standard deviation of 0.79 µJ (2.61 %). In contrast, at a pump power of 1000 mW, a clear split into two regions and a mean total pulse energy (main and satellite pulses) of 36.85 µJ was determined. Thereby the standard deviation was 5.01 µJ which is equivalent to 13.60 %. A closer look at the post-processing pulse train analysis also shows that the satellite pulses (upper branch) are clearly separated from the main pulses (lower branch). If only the main pulses are considered, a mean value of 31.99 µJ with a standard deviation of 3.11 µJ (9.79 %) was determined.

Figure 4.10 (c) shows the calculated peak power in addition to the pulse energy. Under the assumption of Gaussian pulses (correction factor 0.94 [47]), the peak power was calculated from the main pulse energy from (c) and the main pulse duration from (b), whereby the satellite pulses were completely neglected. For the peak power, increasing values between 3.17 kW and 4.04 kW were obtained with increasing pump power values. The reason for the increasing peak power is the growing pulse energy with an almost constant pulse duration.

Besides the output parameters (beam quality, divergence angle, pulse duration, and pulse energy), the spectrum of the passively Q-switched laser was recorded for all pump power levels. Figure 4.16 shows various characteristic spectra recorded for different pump powers between 200 mW and 975 mW. Up to a pump power of 500 mW, only a longitudinal mode was observed although the resonator was still relatively long with a physical length of about 14 mm. A Gaussian fit resulted in a center wavelength of 913.848 nm and a spectral width of just 2.2 pm (FWHM). At a QC pump power of 525 mW, the excitation of a second

longitudinal mode was observed, which was blue-shifted compared to the first mode. Beginning at 650 mW, a larger number of longitudinal modes was observed with increasing pump powers. Finally, at a pump power of 975 mW, ten longitudinal modes with different amplitudes were recorded. In addition, a significant spectral broadening was ob-

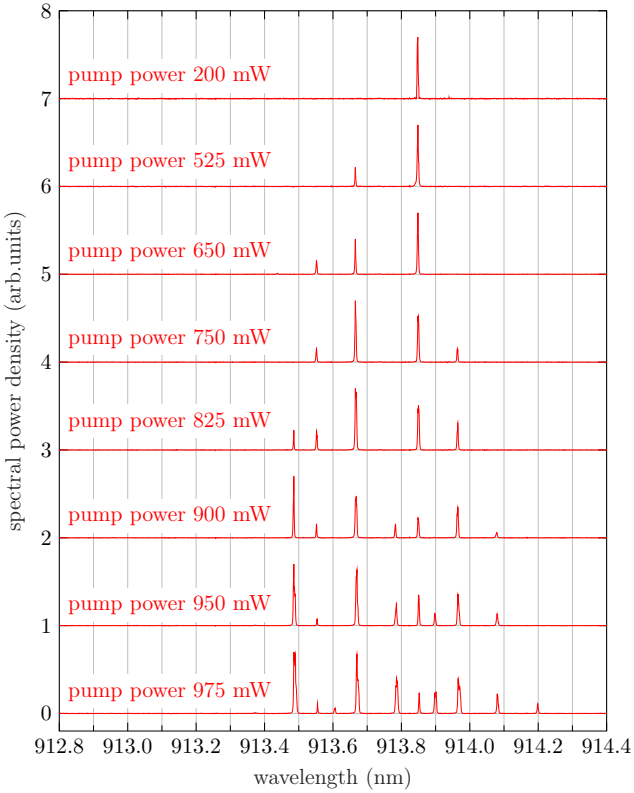

Figure 4.16: Experimental investigation of the spectral mode structure of the passively Q-switched laser as a function of pump power between 200 mW and 975 mW.

served for the longitudinal modes which resulted from the excitation of higher transversal modes. The reason for this is that the transverse fundamental mode (TEM_{00}) experiences a Gouy phase shift of $-\pi$ in the resonator when the Gaussian beam passes through the focus [47]. For higher-order transverse modes, the is a similar but slightliy but stronger phase shift. Consequently, the frequencies of higher transverse modes are slightly higher, compared to the fundamental mode. The excitation of higher transverse modes with increasing pump power can likewise be observed in Figure 4.9 as the beam quality factor deteriorates with increasing pump power.

At a pump power of 750 mW, two different spactral spacings of approximately 0.12 nm and 0.18 nm were determined between 913.5 nm and 914.0 nm. This is equivalent to an optical cavity of roughly 3.5 mm and 2.3 mm, respectively and cannot be properly assigned to any of the experimental cavity elements. The gain medium with a lenght of 5 mm ($n = 1.9647$ [89]) and the saturable absorber with a thickness of approximately 0.22 mm ($n = 1.8180$ [170]) have optical path lengths of 9.82 mm and 0.36 mm, respectively. On the other hand, an optical path length of 10 mm ($n = 1$) was estimated for the air gap between the saturable absorber and the output coupler mirror.

A possible reason for the determined spectral spacings of 0.12 nm and 0.18 nm could be the superposition of different parasitic reflecting elements with the gain bandwidth of the laser crystal. This may eventually cause the spectrum to have irregular gaps in the longitudinal modes. It is also possible that spatial hole burning in the linear cavity can lead to a shift of the longitudinal mode spacing. The missing mode at about 913.75 nm can possibly be explained by parasitic reflections at various optical elements in the resonator. As already shown in Figure 4.5 for a simplified resonator, the insertion of an absorber with a non-perfect AR coating leads to an additional reduction of the longitudinal mode number.

As mentioned before, from a QC pump power of about 650 mW, satellite pulses could be observed in the pulse train. The corresponding spectrum in Figure 4.16 shows at this pump power the appearance of a third longitudinal mode at about 913.55 nm, while the second longitudinal mode at about 913.68 nm has a non-negligible amplitude compared to the first one. The fact that satellite pulses appear with the establishment of a second and the growth of a third longitudinal mode suggests that the main and satellite pulses do not share the same mode. This reinforces the previous assumption that the remaining gain in the gain crystal, after the main pulse builds up, is still sufficient for a satellite pulse to build up.
For further measurements, it would be interesting to determine whether the main and satellite pulses have the same or a different longitudinal mode. For this purpose, no pulse train but single pulse excitation (see Chapter 5) should be used to be able to assign the spectrum exactly to the single pulse when satellite pulses occur. With a pulse train and a spectrometer integration time of 10 ms, the spectrum is averaged over all main and satellite pulses, so that individual longitudinal modes can no longer be precisely assigned. With the externally triggered spectrometer operation, the spectrum can be assigned exactly to the time period, and thus it can be identified whether the main and satellite pulses are the same or consist of two different modes.

4.3.2 Polarization of laser emission

Compared to the commonly used Yttrium Aluminum garnet (YAG), YVO_4 is a host material with an anisotropic crystal structure. Here, the tetragonal symmetry (space group D_{4th}^{19}) leads to a large positive birefringence where the Y^{+3} site symmetry D_{2d} is responsible for the polarized transition in Nd^{3+} [174]. Since for many applications the polariza-

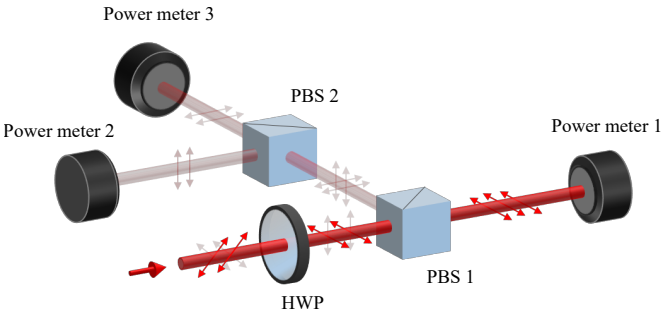

Figure 4.17: Experimental setup for the investigation of the polarization properties of laser emission. HWP: half-wave plate, PBS: polarizing beam splitter.

tion properties of the laser light is important, they will be considered in the following for different pump power levels. Figure 4.17 shows the experimental setup for the investigation of the polarization properties of the laser light. Here, the input beam to be investigated is indicated by the red arrow. The half-wave plate (HWP) (Thorlabs WPH10M-915) enables the polarization components of the incoming light to be rotated by an arbitrary angle theta. In combination with the subsequent polarizing beamsplitter cube PBS 1 (Thorlabs PBS202 - extinction ratio T_p:T_S > 1000:1), the transmitted component can thus be maximized or minimized and evaluated on the Power Meter 1. Since the extinction ratio of the PBS in reflection (R_P:R_S) is only about 50:1 according to the manufacturer, a second polarizing beamsplitter PBS 2 (also Thorlabs PBS202) was used and the light reflected at PBS 1 was additionally analyzed via two further power meters (2 and 3). This combination of two beamsplitters allows the polarization of the laser to be fully investigated. Figure 4.18 shows the power measured at Power meter 1 as a function of the half-wave plate rotation angle. For this purpose, a pump power corresponding to 1.5 times (red) and 3 times (blue) the Q-switched pump threshold of 195 mW was applied. Over a rotation of 360°, a total of four maxima and four minima of the transmitted power could be deter-

mined at the power meter.

The four-fold symmetry originates from the properties of the half-wave plate, which rotates the light polarization vector by twice the angle of rotation of the retardation plate itself. Consequently, over a rotation of 360°, the light polarization is rotated two full revolutions, resulting in four transmission maxima through the subsequent polarizing beam splitter. For the 1.5-fold threshold, the maximum transmitted power was determined to be 34.2 mW, while for the 3-fold threshold, 88.5 mW was measured. Simultaneously with the rotation of the HWP, the power was observed at Power meter 2 and Power meter 3. Here, it was found that for the angles 0°, 90°, 180°, and 270°, the light parasitically reflected at PBS 1 was exclusively p-polarized, as no light could be ob-

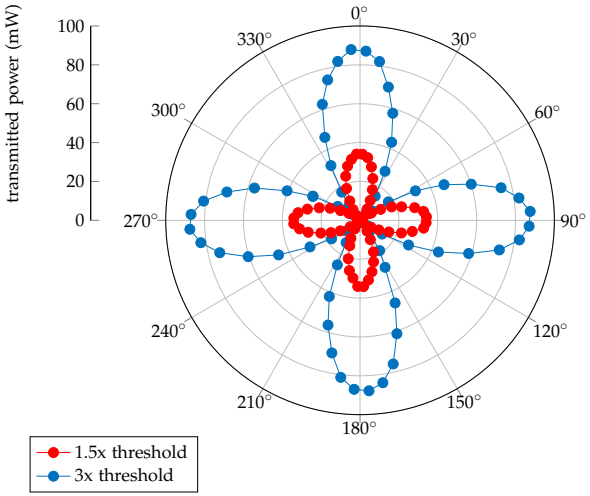

Figure 4.18: Polar diagram of the experimental investigation of the polarization properties of the laser emission. Here, the transmission through a PBS is shown for 1.5 times (red) and 3 times (blue) the pump threshold as a function of the polarization angle.

served at Power meter 3 for these positions. In conclusion, a pure linear light polarization of the laser light generated by the Nd^{3+}:YVO_4 crystal was observed during these measurements.
In addition, the polarization of the solid-state laser was observed as a function of the polarization of the pump laser. For this purpose, the wave plate in the characterization setup in Figure 4.17 was set once in such a way that no light could be observed in the transmission of the PBS 2. The light reflected at PBS 1 was then reflected again at PBS 2 and could only be detected at power meter 2. Therefore, it could be assigned to the p-polarization of the solid-state laser. Subsequently, the pump laser half-wave plate was rotated to rotate the pump light polarization in front of the solid-state laser (see the setup in Figure 4.6) and at the same time, the transmission behind the PBS 2 was observed. For different rotation positions of the pump laser half-wave plate, no transmission behind the PBS 2 could be observed, which indicates that the preferred direction of the pump laser polarization does not influence the solid-state laser polarization. A possible reason for this could be the large birefringence of YVO_4 as a host material. In comparison, the host material YAG has an isotropic crystal lattice, and accordingly, experiments by Liu et al. in 1997 showed that the output polarization of a Cr^{4+}-Nd^{3+}:YAG laser strongly depended on the polarization of the pump laser diode [133].

4.3.3 Cavity length dependencies

To investigate the influence of the resonator length, the experimental setup II (4.6) was modified and the external output coupler mirror was mounted on a linear piezo stage (SmarAct SLC-2475) and controlled by an external controller (SmarAct MCS2). Using the stepper motor mode of the piezo stage, the resonator length was moved in 2 mm steps be-

tween 0 mm and 28 mm, thus varying the resonator length. Although the stepper motor of the Piezo Stage allows significantly smaller relative step sizes, a step size of 2 mm was adequate to map the entire measuring range with sufficiently accurate resolution. For analysis, the relative resonator length was converted into the correct physical resonator length. Here, the physical resonator length corresponds to the simple mirror spacing without considering the refractive indices of optical elements. Since the saturable absorber was directly bonded to the laser crystal by the setup depicted in Figure 4.6, the movement of the OCM only changed the resonator length, but not the position of the absorber inside the cavity. In the following graphs, the gray shaded area symbolizes the 5 mm long laser crystal and thus represents the lower limit of the resonator length. For investigation of the output parameters considering the resonator length, the characterization setup from Appendix 7.1 was utilized.

The pump threshold of the passively Q-switched laser is shown as a function of resonator length in Figure 4.19 (a). Here, the experimentally measured values are shown as blue dots, while simulations based on a previous publication by Brenier et al. [175] are indicated with a gray dashed line. The constants and parameters from Table 3.2 were chosen for the simulations. The experimentally measured threshold initially increases linearly from 250 mW (resonator length 7.5 mm) to 312 mW at 25.5 mm and then changes nonlinearly for longer resonator lengths to a maximum value of 465 mW at a physical resonator length of 35.5 mm. A reason for the general increase of the threshold value becomes clear from the anticipatory change of the beam radius in Figure 4.20 (a), where it was observed that the beam radius increases with increasing resonator length. The increase in beam radius worsens the (transverse) overlap between the focus of the pump mode ($\sim$ 100 µm radius) and the resonator mode, thus raising the pump threshold. The nonlinear increase for longer resonators is probably because in addi-

tion to the transverse beam overlap, the position of the resonator focus also shifts with increasing resonator length and consequently the longitudinal overlap between both beams is reduced as well. Although the resonator alignment was optimized at each approached cavity length, the pump lens was readjusted only in the transverse directions and not shifted longitudinally (forth or back) for better comparability between

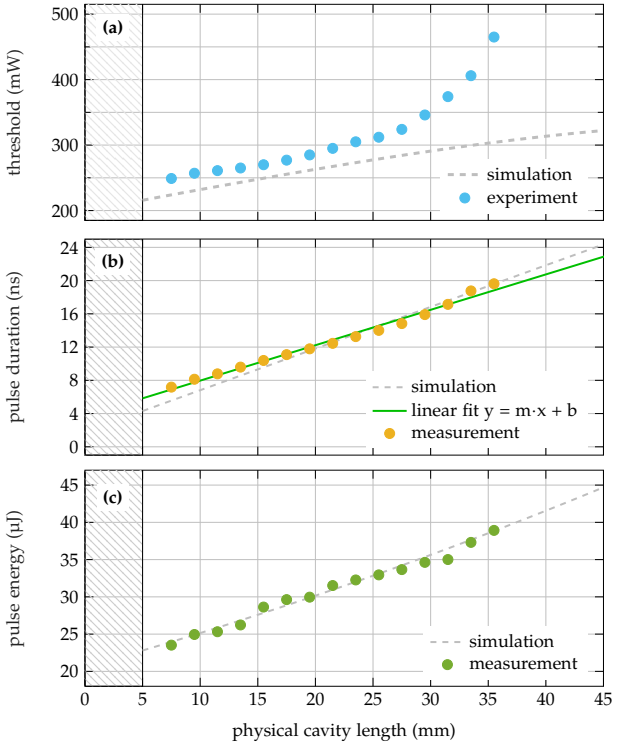

Figure 4.19: Output parameters of the laser as a function of the physical cavity length. The pulse duration including linear fit is shown in (a). In (b) is the pulse energy, while (c) shows the pump threshold. Results of numerical simulations based on the rate equation model are shown as a gray dashed line.

measurements. According to Figure 4.20 (a), the increasing radius of the resonator mode is already taken into account in the simulations for the pumping threshold, which is the reason why there is a good agreement between the simulations and the experiment for shorter resonator lengths. From about 25.5 mm onwards, the deviation between experiments and simulations rises, which may be due to the longitudinal overlap between pump and resonator mode, which was not taken into account for the simulations.

Figure 4.19 (b) and (c) show the pulse duration and pulse energy as a function of the resonator length. For the pump power, the respective 1.5-fold pump threshold value from (a) was used. A linear increase from 7.2 ns to 19.6 ns with increasing resonator length was observed for the pulse duration. The obtained pulse duration results from two superposition effects. On the one hand, for longer resonators, the round-trip time in the resonator increases, and consequently more time elapses until a pulse has built up leading to an increase in pulse duration. On the other hand, the increase of the beam radius (Fig. 4.20 (a)) causes the spot size on the saturable absorber to increase (see (c)), and accordingly, a higher occupation inversion will build up in the gain crystal until the saturable absorber becomes transparent at a certain fluence. Since the pulse builds up exponentially in the resonator, a higher occupation inversion accordingly leads to a faster build-up of the pulse and consequently to a shorter pulse duration. As can be seen by the experimentally observed linear increase in pulse duration, the effect of longer pulse build-up time dominates over the increase in laser radius. A linear fit (green solid line) of the pulse duration, neglecting the thickness of the saturable absorber, yields a minimum pulse duration of 6.9 ns for a 5 mm long gain crystal. The pulse duration grows on average by $0.41\,\mathrm{ns\,mm^{-1}}$ with an increase in resonator length. For the pulse energy, a linear increase from 23.5 µJ to 38.9 µJ was observed with an extension of the resonator length, which is illustrated in (c). The gray dashed line

in Figures (b) and (c) corresponds to simulations based on the rate equation model from Chapter 3 (Equation 3.1 - 3.3). For the simulation, the constants from Table 3.1 were chosen, where for the pump power in each case the 1.5 times threshold value from Figure 4.19 (a) and for the beam radius the corresponding values from Figure 4.20 (c) were used. The simulations based on the rate equations reproduce the experiments very well for both the pulse duration and the pulse energy. For each resonator position approached, the passively Q-switched laser beam was coupled into a beam analyzer (Ophir SP920) using a flip mirror (see the setup in Appendix 7.1). This allowed the beam radius, divergence angle, and beam parameter to be studied as a function of physical resonator length, which is shown in Fig. 4.20 (a)-(c). The experimental measurements are shown as red and blue dots for the x- and y-direction, respectively, while the gray dashed lines are simulations of the resonator stability based on the matrix formalism (see Section 3.3). To perform the simulations, a loop was used to vary the resonator length, and for each loop pass, the increase in pump power and the resulting thermal lensing was already taken into account by calculating the thermal dioptric refractive power according to Eq. 2.14. Subsequently, the beam radius and divergence angle at the associated thermal refractive power could be determined for each loop pass. The beam radius in (a) increases in both directions as a function of resonator length from about 100 µm um to 141 µm. This increase is partly due to the geometric change in the length of the resonator but also arises from the growing thermal lens. The good agreement between simulation and experiment shows that both effects have to be taken into account. Inversely to the beam radius, the divergence angle in (b) decreases equally in both directions from about 4.5 mrad to 3.4 mrad. The associated beam parameter product is shown in (c) and is calculated from (a) and (b). For all resonator lengths, this product remains relatively constant between 0.4 mm mrad and 0.5 mm mrad which corresponds to a converted M^2 between 1.37

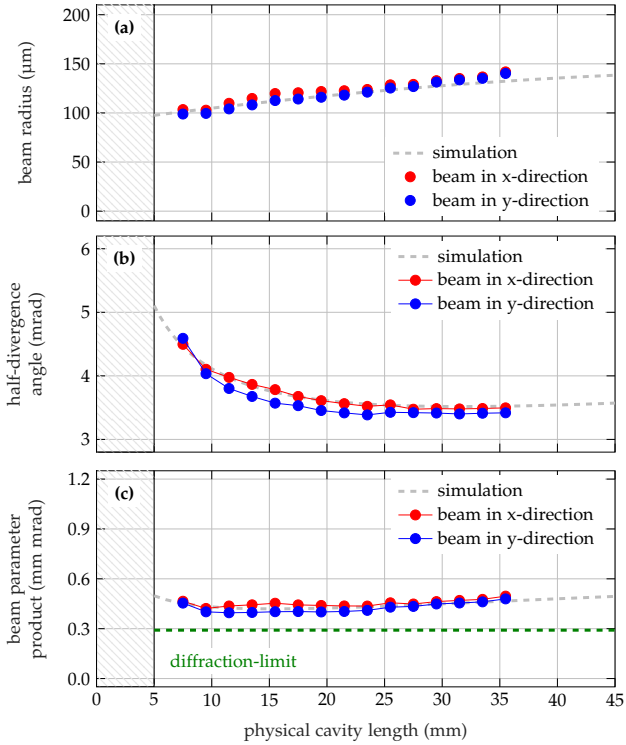

Figure 4.20: Dependence of the laser radius in (a), the divergence angle in (b), and the beam parameter product in (c) on the resonator length. The measurement results in x- and y-direction are shown as red and blue dots, respectively, while simulations based on the matrix formalism are shown as a gray dashed lines. The gray shaded area from 0 mm to 5 mm represents the gain crystal.

and 1.72 at 914 nm. In addition, the green dashed line represents the diffraction limit, which is 0.291 mm mrad for a laser beam with a wavelength of 914 nm.

Due to the very good match between simulation and experiment in Figures 4.19 (a) and (b), the simulations based on the rate equations were

subsequently used to gain a better understanding of the system relationships and to obtain important information for a future system design. For this purpose, it is generally important that the pulse duration and pulse energy can be adjusted independently of each other by a proper choice of the system components and parameters. Since both the pulse duration and the pulse energy are functions of the resonator length and the initial transmission of the saturable absorber, these two quantities were varied in a parameter sweep to cover a certain parameter space in which the pulse duration or pulse energy changes while the other quantity remains constant. Based on the simulations depicted in Figures 4.19 (b) and (c), where only the resonator length was changed in the interval between 5 mm and 45 mm, the initial transmission of the saturable absorber was now additionally added as a possible design parameter. Both Figures 4.21 and 4.22 show the simulation results for which the initial transmission and resonator length were varied simultaneously. Similarly, the constants from Table 3.1 were chosen, where for the pump power in each case the 1.5 times threshold value from Figure 4.19 (a) and for the beam radius the corresponding values from Figure 4.20 (c) were used. For the initial transmission of the saturable absorber, 800 positions were swept between 90 % and 99 %, while the resonator length was varied over 900 positions between 5 mm and 45 mm. This resulted in a total of 720 000 individual simulation runs, providing sufficient resolution to visualize lines on which one of the two quantities remains constant while the other one changes. Figure 4.21 shows the pulse duration for which values between 5.5 ns and 82.4 ns were calculated by varying the initial transmission and the resonator length. The minimum pulse duration is obtained for the shortest possible resonator (5 mm) in combination with a saturable absorber with an initial transmission of about 95.5 %. For short resonators, the effect of resonator length dominates (see discussion on Fig. 4.19 (a)) and the choice of saturable absorber does not have such a large influence on the pulse duration. In

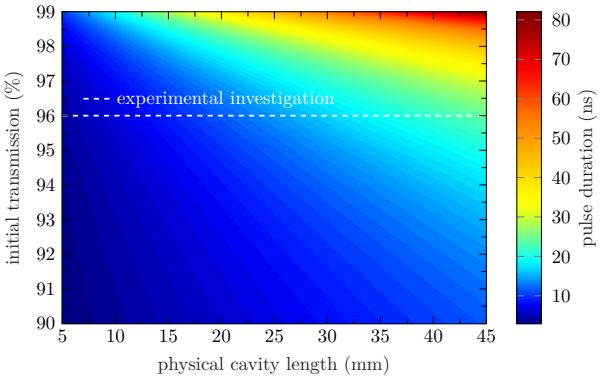

Figure 4.21: Simulated pulse duration based on the rate equation model as a function of the initial transmission of the saturable absorber and the physical resonator length. The white dashed line indicates the experimental investigation.

comparison, it can be observed that for long resonators, the choice of initial transmission has a very large effect on the expected pulse duration and large changes in pulse duration occur for small changes. The maximum pulse duration is obtained for a resonator length of 45 mm and the largest possible chosen initial transmission (99 %). However, it should be noted that in the limit value for T_0 against 1 the passively Q-switched laser changes into a CW laser, which purely in terms of illustration has an infinitely long pulse duration. Due to the parameter sweep with the sufficiently high resolution, it becomes clear that the pulse duration moves constantly on lines from the lower right to the upper left and that different combinations of resonator length and initial transmission can lead to the same pulse duration. The white dashed line additionally represents the simulations from Figure 4.19, which were matched with the experimentally measured values and calculated for a constant initial transmission. Analogous to the pulse duration, the simulated pulse energy is investigated in Figure 4.22 as a function of the initial transmission and the resonator length. In this case, the pulse

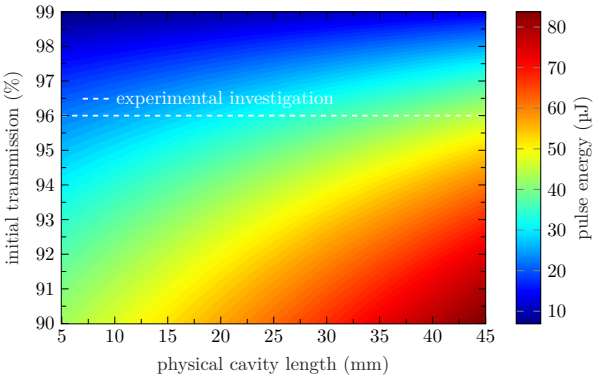

Figure 4.22: Simulated pulse energy as a function of the initial transmission of the saturable absorber and the physical resonator length. The white dashed line indicates the experimental investigation.

energy approaches values between 8.5 µJ and 83 µJ for different combinations, whereby the minimum value is reached for a 5 mm short resonator and the largest possible initial transmission (99 %). Likewise, this can be accounted for the transition to CW operation in the limit of initial transmission set to one. On the other hand, the maximum pulse energy is achieved for a long resonator (45 mm) and the lowest adjusted initial transmission of 90 %. While in Figure 4.21 for constant pulse duration there is a linear relationship between the initial transmission and resonator length, constant pulse energies follow a circular relationship from the lower left to the upper right. This is an important finding, as the combination of Figure 4.21 and 4.22 can be used to design a system in which the pulse duration and pulse energy can be determined to some extent independently of each other by a proper choice of initial transmission and resonator length. In general, for a system layout, it is desirable to have a large and stable range in which small changes do not lead to a large variation of the output parameters.

output coupler reflectivity	supplier
98 %	Layertec
97 %	Layertec
95 %	Layertec
92 %	Layertec
90 %	Layertec
85 %	Casix

Table 4.1: Overview of the output coupler mirrors used in the experimental investigations with specification of the reflectivity and the supplier.

4.3.4 Output coupler reflectivity

The OCM is a key component in the laser system and accordingly, the choice of reflectivity has a large impact on the performance and output parameters. Through the choice of output coupler reflectivity, the fraction of intracavity power that is coupled out of the resonator is determined. Therefore a high output power can in principle be expected with a high degree of output coupling. However, this also increases the resonator losses and as a consequence, the lifetime of the resonator is reduced. In turn this leads to a lower photon density in the resonator and affects the dynamics of the laser. This ultimately affects the repetition rate, pulse duration, pulse energy, and peak power. On the other hand, choosing an output coupling reflectivity that is too low in combination with a pump power that is too high can lead to high intracavity power and consequently a strongly pronounced thermal lens, which in extreme cases can cause instabilities of the laser or damage to intracavity coatings.

To investigate the output coupler reflectivity, different plane output coupler mirrors with reflectivities between 85 % and 98 % at 914 nm

were used in the passively Q-switched laser setup of Figure 4.6. Their influence on the laser performance was investigated. Since all output coupler mirrors had the same substrate thickness, the linear piezo stage from Subsection 4.3.3 (resonator length investigations) was used to enable comparable resonator length by repeatedly moving to the same position of the output coupler mirror. For the various output couplers, fused silica with a thickness of 6.35 mm was used as substrate. Table 4.1 gives an overview of the used output couplers with information about the reflectivity and the manufacturer from which the mirrors were supplied. In addition to the partially reflective coatings of 85 %, 90 %, 92 %, 95 %, 97 %, and 98 % at 914 nm, the output couplers were specified with AR coatings for 1064 nm (R<0.25 %) and 1342 nm (R<0.25 %) to suppress parasitic laser operation at these wavelengths.

The experimental measurements of the pump threshold and pulse energy with the corresponding simulations as a function of the output coupler reflectivity are shown in Fig. 4.23. For these measurements, a relatively short resonator length of about 15 mm was chosen to keep the threshold as low as possible, since for the later investigations of the pulse energy, 1.5 times the threshold value was chosen as pump power. The pump threshold as a function of the output coupler reflectivity is plotted in Figure (a), where the red dots indicate the experimentally measured pump thresholds for the different output couplers, while simulations based on a theoretical threshold equation according to previous work by Brenier et al. [175] are shown as blue lines.

In the graph, only the results for output coupler reflectivities between 85 % and 97 % are shown, since the passively Q-switched laser could not be operated stable at an output coupler reflectivity of 98 % as defects were observed on the AR coating of the Cr^{4+}:YAG saturable absorber. A possible reason may be the low output coupler efficiency of just 2 %, whereby the intracavity power in combination with the small laser radius results in intensities above the laser-induced damage threshold

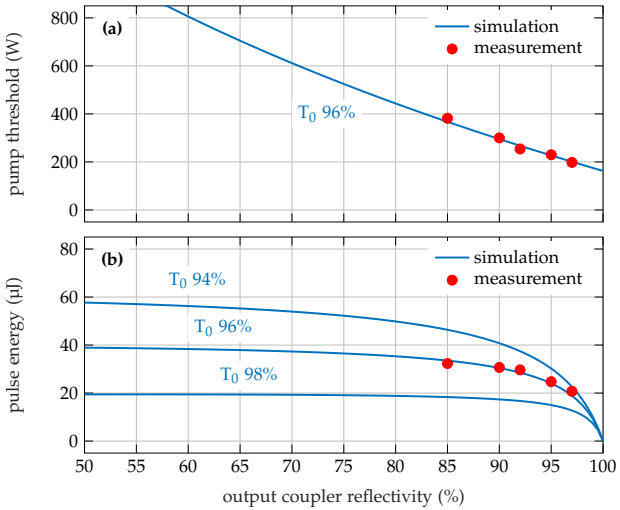

Figure 4.23: Investigation of laser pump threshold and pulse energy as a function of output coupler reflectivity. The red dots represent experimentally measured values, while corresponding simulations are shown in blue.

of the AR coating, and consequently, damage occurs. For each of the subsequent output couplers, the system was iteratively optimized and a pump laser threshold of 198 mW at 97 %, 230 mW at 95 %, 254 mW at 92 %, 300 mW at 90 %, and 382 mW at 85 % reflectivity could be determined. Furthermore, no damage to the AR coating of the saturable absorber was observed.

For the simulations, the material constants and parameters from Table 3.1 of Chapter 3 were used and only the output coupler reflectivity was varied. The theoretically calculated threshold values coincide very well with the experimentally observed results and they rise as the output coupler reflectivity increases. This rise is due to the growing resonator losses with decreasing output coupler reflectivity. For a purely theoretical reflectivity of 100 %, the calculated threshold just compensates

for the internal resonator losses and the reabsorption effect of the laser crystal in the quasi-three level system.
The investigation of the pulse energy is shown in Figure 4.23 (b), where simulations based on the rate equation model (see Section 3.1) were used in addition to the experimental measurements. In addition to the experimentally used initial transmission of the saturable absorber of 96 %, simulations for initial transmissions of 94 % and 98 % were also performed to get a sense of how the choice of the absorber affects the pulse energy. In Section 4.3.1 (Pump power investigation and instabilities) it was already shown that the pulse energy varies slightly with the applied pump power. Consequently, the 1.5 times threshold value from Figure 4.23 was applied to each of the OCMs for the experiments to establish comparability between the individual output coupling levels. Similar to the previous investigations, the QC pulse train analysis (Appendix 7.2) was performed for the experimental determination of the pulse energy. In the experiments, with decreasing output coupler reflectivity, an increase in pulse energy was observed from 20.7 µJ at 97 % to 32.3 µJ at 85 %. For the simulations, the parameters and constants were chosen according to Tab. 4.1 The conducted simulations for a saturable absorber of 96 % reproduce well the experimental studies. The initial transmission of the saturable absorber ultimately determines how high the occupation inversion in the gain medium is at the time the absorber is switched through and thus has a significant influence on the pulse energy. This relationship is made clear by the simulations with the different initial transmissions of 94 %, 96 %, and 98 % since a decrease in the initial transmission leads to a significantly increased pulse energy for the same output coupler reflectivity. Thus, in theory, pulse energies of just about 60 µJ are possible for an initial transmission of 94 % combined with an output coupler reflectivity of 50 %.
Similar to the resonator length studies, the simulations based on the rate equation model were used to perform a parameter sweep of the

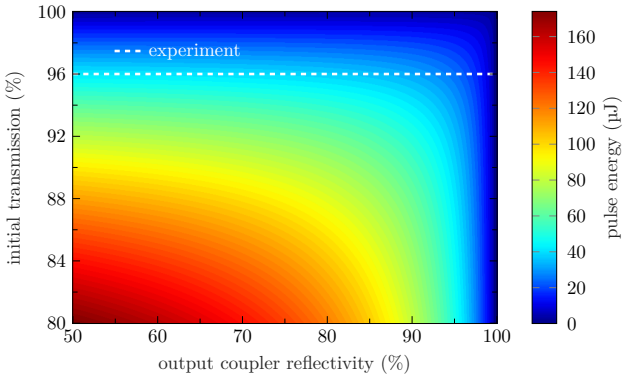

Figure 4.24: Simulated parameter sweep of the pulse energy as a function of the initial transmission of the saturable absorber and the reflectivity of the OCM. The white dashed line indicates the associated experimental studies for a fixed initial transmission of 96 %.

initial transmission of the saturable absorber and the output coupler reflectivity. Since a good agreement was observed between the experimentally measured values and the calculations given in Figure 4.23 (b), these simulations provide a good basis for evaluating the system limits in terms of pulse energy. For the parameter sweep, the rate equations were solved numerically in two loops and the initial transmission was varied between 80 % and 100 % over 490 positions, while the output coupler reflectivity was changed between 50 % and 100 % over 1000 positions. In total, the variation of initial transmission and output coupler reflectivity thus resulted in 490 000 individual simulation loops. The resulting estimation for the pulse energy is shown in Figure 4.24 Varying the initial transmission and output coupler reflectivity yields pulse energies between 0 µJ and 174 µJ. Constant pulse energies are visible as lines of the same color in the figure and can be achieved by varying the initial transmission and output coupler reflectivity in opposite directions. For large initial transmissions and output coupler reflectivities, a

small variation of the parameters has a rather small effect on the pulse energy, while for lower initial transmissions and output coupler reflectivities, the pulse energy can be changed strongly by small changes of the parameters. The maximum pulse energy is achieved for an output coupler reflectivity of 50 % and an initial transmission of 80 %, while the minimum pulse energy of 0 µJ represents a theoretical limit. This is reached on the one hand for a vanishing output coupler reflectivity or for an initial transmission towards 100 %, which corresponds to a transition to a CW laser. The white dashed line represents the experimental investigations from Figure 4.23 (b), where the initial transmission was kept constant at 96 %.

The simulations agreement with the experiments show that the pulse energy can be determined purely by the choice of the initial transmission or output coupler reflectivity. By comparison with the investigations on the influence of the resonator length (Subsection 4.3.3), a system can be developed in which both the pulse duration and the pulse energy can be determined within a certain range by the proper choice of the system components.

For further investigations, it would be interesting to use a significantly low initial transmission and output coupler reflectivity in the experiments to establish a better correlation to the parameter sweep of the rate equations. Furthermore, similar parameter variations could be performed to determine pulse duration, repetition rate or, even system conversion efficiency to create a complete picture for possible applications.

4.3.5 Long-term stability

For the long-term study of the output parameters, the characterization setup shown in Figure 7.1 (Appendix 7.1) was used and the spectrum, repetition rate, pulse duration, and pulse energy were recorded simultaneously for a total duration of 60 minutes.
For this measurement, the laser was thermally equilibrated for 10 minutes after the switch-on before the measurement was started. For this experiment, a physical resonator length of about 14 mm was chosen, analogous to the investigation of the pump power (Subsection 4.3.1). To operate the system in saturation, a pump power of 700 mW was used, which corresponded approximately to 3.5 times the pump threshold of 195 mW. Figure 4.25 (a) shows the aligned output spectra recorded with the high-resolution spectrometer (Lightmachinery HF-8991-3). To operate the spectrometer in externally triggered mode, QC operation was generated at the pump laser driver (Ostech ds11-la14v14) using a Digital Delay Pulse Generator (Quantum Composers 9520 Series). The spectra were recorded at a sampling rate of 1 sample/second and were consequently averaged over 5 pulse trains as the laser was operated at 5 Hz (10 ms/200 ms QC operation). Using a post-processing script, the 3600 recorded spectra were subsequently normalized and aligned to result in Fig. 4.25 (a). Similar to the pump power studies (see Subsection4.3.1), it was observed that the laser runs on several longitudinal modes at a pump power corresponding to 3.5 times the threshold.
Over one hour, the number of modes fluctuated between three, four, and five modes about the centroid wavelength at approximately 913.8 nm. Analogous to the previous investigations (see Figure 4.16), two different spectral mode spacings of about 0.12 nm and 0.18 nm could be identified. As described before, neither of these distances can be attributed

to the etalon effect of the optical resonator elements alone. Instead, it is assumed that the mode spacings result from a superposition of different parasitic reflecting elements with the gain bandwidth of the laser crystal. In addition, spatial hole burning of the linear resonator could also lead to a shift of the longitudinal mode spacing.

In Figure 4.25 (a) it is noticeable that the laser does not run stably on the different longitudinal modes, but rather repeatedly jumps back and forth between different combinations of longitudinal modes over one hour. A possible reason could be attributed to mechanical vibrations or small temperature fluctuations of the cooling water supply by the chiller or the room temperature. These fluctuations lead to a slight change of the optical resonator length but also a shift of the gain bandwidth of the laser crystal due to the thermal expansion of the components. As a result, different modes experience different gain and loss.

As will be shown later in Chapter 5 for a monolithic microchip laser crystal, the shorter cavity leads to a larger FSR and thus a stable single-longitudinal mode operation. The time evolution of repetition rate and pulse duration was recorded using an InGaAs photodiode (Thorlabs, 5 GHz bandwidth) coupled to a 6 GHz bandwidth oscilloscope (LeCroy WavePro 804HD). At a sampling rate of 5 samples per second (5 Hz $\widehat{=}$ 1/200 ms duty cycle period), each 10 ms pulse train could be completely captured and analyzed by the oscilloscope with a sufficiently high temporal resolution. In this process, the average repetition rate and pulse duration were determined automatically from each pulse train. The repetition rate evolution determined in this way is shown in orange in Figure 4.25 (b) and had an average value of 69.31 kHz over 60 min. At 1.28 kHz, the calculated standard deviation was 2.45 %, which is considered a reasonable value in the low single-digit percentage range for passively Q-switched lasers [150, 30].

To determine the pulse duration (subframe (c)), the average FWHM of each pulse of the pulse train was determined and a mean value

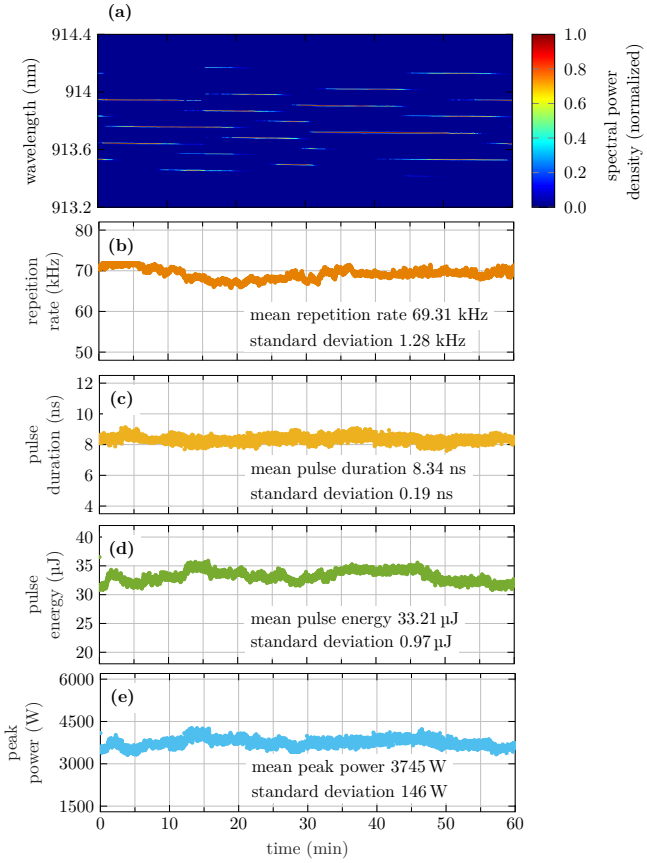

Figure 4.25: Long-term investigation of the output parameters of the passively Q-switched laser. Over 60 minutes, the spectrum (a), repetition rate (b), pulse duration (c), and pulse energy (d) were recorded simultaneously. The peak power (d) was subsequently calculated from the pulse energy and pulse duration.

of 8.34 ns was obtained over one hour. With a standard deviation of 0.19 ns, this corresponds to a deviation of 2.28 %. The stability of the pulse energy is shown in green in Figure 4.25 (d) and was recorded

with a pyroelectric energy sensor (Ophir PE9-C). At a sampling rate of 5 samples/second, each pulse train was acquired and the pulse energy averaged over an entire pulse train. Over one hour, a mean pulse energy of 33.21 µJ was determined with a standard deviation of 0.97 µJ (2.94 %). The corresponding peak power is shown in (e) and was calculated from the pulse energy and pulse duration using

$$P_p = 0.94 \cdot \frac{E_p}{\tau_p} \tag{4.3}$$

under the assumption of a Gaussian pulse shape [47]. Here, E_p is the pulse energy, τ_p is the pulse duration, and 0.94 is a correction factor that accounts for a Gaussian pulse shape. The mean value of the peak power was found to be 3745 W, whereas the standard deviation was accounted to 3.90 %, which corresponds to 146 W. Since the peak power was calculated from the pulse energy and pulse duration, it is not surprising that the variation of the peak power was much more pronounced than that of the pulse energy.

By comparing the individual measurements in Figure 4.25 (a) to (e) a correlation between the variations of the output parameters and the longitudinal mode structure can be established at certain points in time. This is not surprising and emphasizes the close correlation between the dynamics of the laser spectrum and the output parameters. For example, if the resonator length is changed due to small temperature variations, the longitudinal modes in the resonator are spectrally shifted and their position below the gain bandwidth of the laser crystal is modified. On the other hand, vibrations of the resonator components or a slight fluctuation of the pump power can lead to undesired disturbances of the laser dynamics. Due to the discrete mode character, this often leads to a redistribution of the longitudinal mode structure, which directly affects the output parameters. If the laser runs on a single longitudinal mode, a sudden jump of the mode to an adjacent one may occur, which

is called mode hopping. In contrast, the longitudinal multi-mode operation often results in a continuous transition between different sets of modes, where the optical power is gradually redistributed between a set of modes [47]. Thus, when looking at the laser spectrum in (a), a continuous transition between different mode combinations can be seen several times. Here, one mode gradually disappears, while at another spectral position the appearance of a new mode can be observed. For instance, the impact on the output parameters of the passively Q-switched laser can be seen at the pulse energy between about 35 minutes and 47 minutes. During this period, a fairly stable plateau in the pulse energy has been observed, which agrees well with the stable operation of the laser on three longitudinal modes. As a result, a change in pulse energy was observed at approximately 47 minutes during the continuous mode transition.

4.4 EXPERIMENTAL SETUP III - DISCRETE CRYSTALS

In the third resonator configuration, a discrete gain medium and saturable absorber were employed to study the temperature effect of the gain medium decoupled from the saturable absorber. Besides the investigation of the temperature dependence of the laser output parameters, the temperature-dependent central wavelength shift was analyzed.
Figure 4.26 shows the schematic structure of the third resonator configuration. Compared to the first configuration, only the discrete OCM was removed and replaced by a dielectric coating directly applied to the saturable absorber. The coating was specified with a partial reflectivity of 95 % at 914 nm and high transmission (R<0.6 %) at the parasitic wavelengths (1064 nm and 1342 nm).
Since a QC pulse mode was used for all subsequent measurements, all associated powers were measured as continuous values and are reported as such in the subsequent experiments. This means that the displayed values include the pause between the QC pulse trains in which the laser was running. Taking into account the duty cycle, the actual power applied in the pulse train can be calculated. For all subsequent measurements a duty cycle of 5 % (10 ms on time with a period of 200 ms) was used. Due to simplicity, all QC pump and output powers given were measured as average power and are given as such in this work. For conversion to the actual peak power in the QC pulse train, the specified values must be multiplied by a factor of 20.

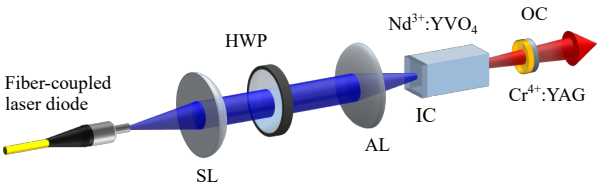

Figure 4.26: Experimental setup of the passively Q-switched laser with a discrete Nd^{3+}:YVO_4 crystal and Cr^{4+}:YAG saturable absorber. SL: spherical lens, HWP: half-wave plate, AL: aspherical lens, IC: input coupler, OC: output coupler.

4.4.1 Temperature-dependency of output parameters

To study the temperature dependence of the passively Q-switched output parameters, the cooling water temperature of the Nd^{3+}:YVO_4 crystal mount was varied between 10 °C and 80 °C and measurements were taken every 5 °C. The saturable absorber (initial transmission of T_0 = 96 % at 914 nm) was kept at a constant temperature of 20 °C using an additional water-cooled holder. A physical cavity length of 14 mm was used for all measurements, and the system was readjusted and optimized at each temperature. For all following measurements, the temperature-dependent determination of the pump threshold allowed to establish certain comparability by using a pump power corresponding to twice the threshold value in each case. The pump threshold of the passively Q-switched solid-state laser is shown in Figure 4.27. as a function of the crystal mounting temperature. For the experimentally determined threshold (light blue dots) a nonlinear increase from 185 mW at 10 °C to 392 mW at 80 °C was observed, which is the consequence of temperature-dependent crystal properties. On the one hand, for increasing temperatures the fluorescence lifetime of the upper laser level decreases, resulting in a decrease of the population inversion. On

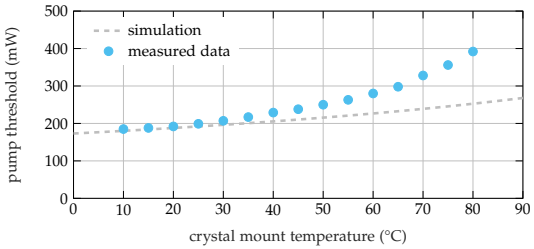

Figure 4.27: Pump threshold of the laser as a function of the crystal mount temperature. The light blue dots indicate experimentally measured values, while the gray dashed line is the simulated threshold.

the other hand, the stimulated-emission cross-section depends on the temperature (see Fig. 4.29), and thermal occupation in the lower laser level increases due to the temperature, which in turn also decreases the population inversion, reduces the number of active ions in the laser process, and also causes emitted laser photons to be reabsorbed. The gray dashed line shows the simulated laser threshold based on an equation of previous work by Brenier et al. [175] considering a temperature-dependent stimulated-emission cross-section $\sigma(T)$ and a reabsorption effect due to the quasi-three level character. However, the temperature-dependent reduction of the fluorescence lifetime and the temperature-dependent increase of the occupation inversion in the lower laser level, which makes the reabsorption temperature-dependent, are not taken into account. For the simulation, a temperature-dependent stimulated-emission cross-section based on the linear approximation from Figure 4.29, while the constants and variables were taken according to Table 3.1. For lower temperatures, the simulated curve agrees well with the experimentally determined values. However, a deviation was observed at higher temperatures, which can probably be attributed to the lack of temperature-dependent occupation density of the lower laser level.
The pulse energy was measured at the respective temperatures for an

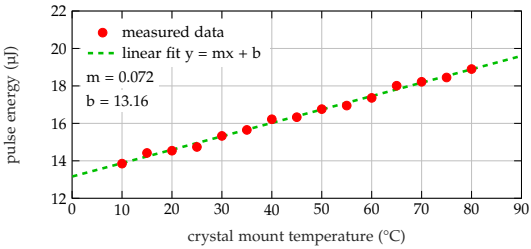

Figure 4.28: Pulse energy of the passively Q-switched laser as a function of crystal mount temperature. The experimental values (red dots) were measured for temperatures between 10 °C and 80 °C, whilst the green dashed line is a linear fit to determine the slope.

applied pump power of twice the pump threshold value in each case. To determine the respective pulse energy, the QC pulse train was analyzed with the post-processing method (see Appendix 7.2) and the average value of three successively recorded measurements was calculated to achieve higher accuracy. Figure 4.28 shows the mean value of the pulse energy measured in the experiment as red dots, while the green dashed line represents a linear fit to determine the temperature dependency. At a crystal holder temperature of 10 °C, a mean pulse energy of 13.85 µJ was measured, which increased almost linearly to 18.90 µJ to a temperature of 80 °C. The linear fit results in a temperature-dependent pulse energy increase of 7.2 µJ/10 °C. From the measurement of the temperature-dependent pulse energy, an estimation of the temperature dependence of the stimulated-emission cross-section for passively Q-switched lasers is possible [159]. Based on the analytical expression for the pulse energy of a passively Q-switched laser

$$E_p = \frac{h\nu A}{2\gamma} \ln\left(\frac{1}{R}\right) \ln\left(\frac{n_i}{n_f}\right) \frac{1}{\sigma(T)} \tag{4.4}$$

a temperature dependence of the stimulated-emission cross-section $\sigma(T)$ can be considered [57]. Here A is the spot area in the gain medium, γ is the inversion reduction factor ($\gamma = 2$ for a three-level system), R is the reflectivity of the OCM, and n_i and n_f are the initial and final occupancy inversion, respectively. By deriving and transforming Equation 4.4, the change of pulse energy versus temperature for an ideal Q-switched laser (assuming negligible ESA of the saturable absorber) is given by

$$\frac{dE_p}{dT} = E_p \left(-\frac{1}{\sigma_0} \frac{d\sigma(T)}{dT} \right) \tag{4.5}$$

where σ_0 corresponds to the stimulated-emission cross-section at room temperature. Reshaping this equation leads to an expression describing the temperature dependency of the stimulated-emission cross-section as a function of the temperature-dependent pulse energy

$$\sigma(T) = \frac{E_0 \sigma_0}{\frac{dE_p}{dT} T + E_0}. \tag{4.6}$$

Figure 4.29 plots Equation 4.6. as an orange line for the fit results obtained in Figure 4.28 and a reference value at room temperature for the stimulated-emission cross-section at 914 nm ($4.8 \times 10^{-20}\,\mathrm{cm}^2$ [34]). For further simplification, a linear fit (green dashed line) was used in the interval between 0 °C and 90 °C, which led to a linear approximation of the stimulated-emission cross-section of $-1.85 \times 10^{-22}\,\mathrm{cm}^2\,^\circ\mathrm{C}^{-1}$ as a function of temperature. Hence, the overall temperature-dependent stimulated-emission cross-section is approximated to be

$$\sigma(T) = 4.7 \times 10^{-20} - 1.85 \times 10^{-22} \cdot T. \tag{4.7}$$

Considering this expression for the temperature dependence of the stimulated-emission cross-section, the pumping threshold in Figure 4.27 was calculated. To estimate the maximum crystal temperature and draw conclusions about the thermal lens, simulations were performed based

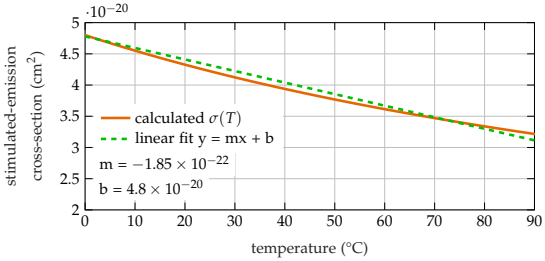

Figure 4.29: Calculated stimulated-emission cross-section as a function of temperature. The orange curve is the predicted stimulated-emission cross-section which is determined by the temperature dependence of the pulse energy. The green dashed curve is an approximated linear fit.

on the FEA from Chapter 3. Figure 4.30 shows the calculated peak temperature as a function of the applied crystal holder temperatures in the equilibrium state. Here, a pump power equal to two times the threshold value from Figure 4.27 was used for the different temperatures between 10 °C and 80 °C respectively. Furthermore, a pump spot diameter of 200 µm and a pump wavelength of 808 nm were selected for the calculation. The simulated results show a significant increase in peak temperature of about 126 °C for crystal mount temperatures between 10 °C and 80 °C. On one hand, the temperature increase is based on the increased crystal holding temperature, which results in a smaller temperature gradient and consequently poorer heat dissipation. On the other hand, the threshold value also increases for higher temperatures, which is why there is a higher thermal load at twice the threshold pumping power.

Measurements for beam characterization were likewise carried out at twice the threshold pump power at each temperature. Here, in addition to the previous measurements, the beam was coupled into a beam quality instrument (Ophir BeamSquared BS920) via a flip mount mirror. Figure 4.31 shows the measurement results of the full divergence angle (a) and the beam quality factor M^2 (b) as a function of the crystal holder

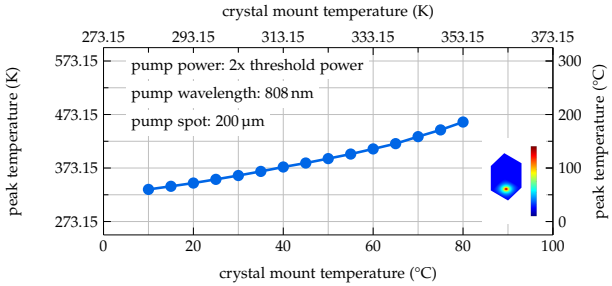

Figure 4.30: Simulation results based on the FEA to determine the pump light-induced peak temperature in the laser crystal. The inset in the lower-right corner exemplifies the model used and shows the induced heat. The corresponding color scaling shows a temperature range of 10 - 210 °C.

temperature. The x-and y-direction are indicated by red and blue dots, respectively. The full divergence angle increases almost linearly from about 8.6 mrad to 10 mrad for temperatures between 10 °C and 80 °C. The main reason for the observed increase of the divergence is the increasing refractive power of the thermal lens, which arises primarily from the increasing pump power. Another but minor influence represents the poorer heat dissipation of the crystal due to the lower temperature gradient. In addition, no significant change in the back-calculated laser beam waist diameter could be detected for any of the temperature ranges investigated. For the beam quality factor M^2 in (b), an increase from 1.5 mrad to 1.8 mrad in the x-direction and from 1.7 mrad to 1.9 mrad in the y-direction was observed. Here, the dashed green line represents the diffraction limit for a Gaussian beam.

The experimentally determined optical-to-optical conversion efficiency and the corresponding pulse duration are shown in (a) and (b) of Figure 4.32, respectively. Analogously to the measurement of pulse energy and beam characterization, the conversion efficiency was determined by measuring the average output power at an applied pump power equal to twice the threshold power. At a crystal holder temperature of

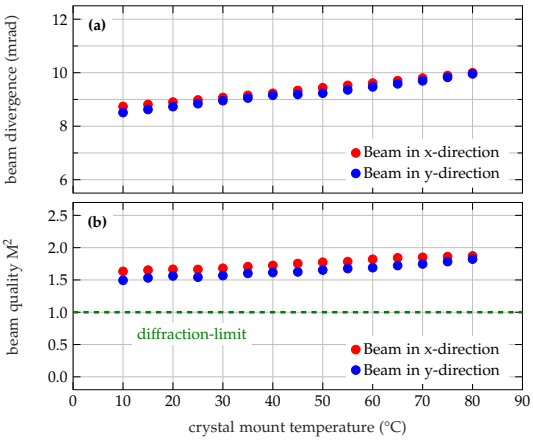

Figure 4.31: Full beam divergence coefficient (a) and beam quality (b) of the solid-state laser in x (red) and y (blue) directions for different crystal holder temperatures between 10 °C and 80 °C.

10 °C, the optical-to-optical efficiency was 15.6 % and decreased with increasing temperature, more than half to a value of 7.6 % at 80 °C. The decreasing efficiency is the result of multiple factors: First, the increasing crystal holder temperature leads to a smaller temperature gradient in the laser crystal and consequently to poorer heat dissipation, resulting in a higher temperature distribution in the laser crystal. As a result of the larger overall temperature in the crystal, a smaller stimulated-emission cross-section, shorter fluorescence lifetime, and increasing reabsorption due to the quasi-three level character follow. In addition, the increasing threshold leads to an increasing pump power, which in turn additionally increases the thermal load, which can then be observed as an approximate parabolic decrease of the efficiency. Measurements of pulse duration shown in Figure 4.32 (b) were also conducted using the post-processing method of the recorded QC pulse trains from the pulse energy measurement. With increasing temperature, the average pulse

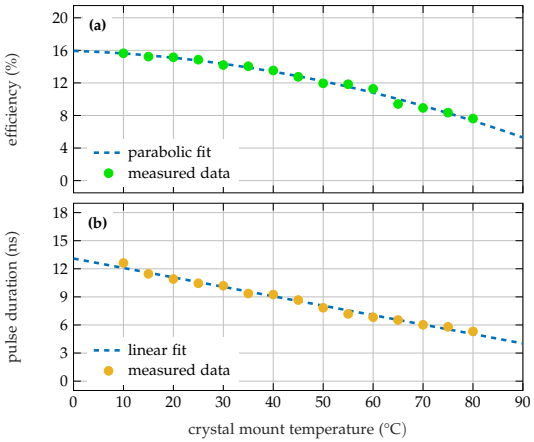

Figure 4.32: Conversion efficiency (a) and pulse duration (b) of the passively Q-switched laser as a function of crystal mount temperature. The green and yellow dots are experimentally measured values, whereas the blue dashed line is a parabolic and linear fit, respectively.

duration decreased from 12.6 ns to 5.3 ns (FWHM). The main reason for this is that after switching through the saturable absorber, the electric field in the resonator builds up exponentially for passively Q-switched lasers. An increase of the pulse energy (see Figure 4.28) for increasing temperatures is a result of a larger population inversion in the gain medium, which follows from the decreasing stimulated-emission cross-section. Due to the exponential buildup, a larger population inversion in the laser crystal causes a faster buildup of the laser mode and consequently a smaller pulse duration with increasing pulse energies. The linear fit to the experimentally determined pulse duration is shown in dashed blue and resulted in a decrease in pulse duration of 1.01 ns per 10 K.

4.4.2 Temperature-dependent wavelength shift

To investigate the temperature-dependent wavelength shift, the gain medium was temperature-controlled between 10 °C and 80 °C using cooling water, and the center-of-mass wavelength of the laser emission spectrum was determined in each case. For this purpose, the experimental setup III (4.26) was modified and the saturable absorber including the output coupler coating was mounted on a linear piezoelectric stage (SmarAct SLC-2475) and driven by an external controller (SmarAct MCS2). Employing this configuration, the resonator length could be varied by changing the resonance condition and thus the oscillation wavelength of the laser was modified. In this way, the resonator wavelength could be tuned at each temperature so that the entire gain bandwidth was exploited while capturing the respective spectra.
The reason for choosing this method was that the longitudinal mode composition changed at different temperatures due to thermal expansion of the gain medium. Therefore no meaningful statement about the central wavelength was possible. For the measurements, four times the pump threshold value taken from Figure (4.27) was used at each temperature to excite several longitudinal modes and to map the gain bandwidth by varying the resonator length using the piezo stage. By changing the resonator length by a distance that corresponds to one FSR, the entire mode comb induced by the resonator is shifted one tooth further, and consequently, the spectrum is congruent with the initial configuration.

The FSR corresponds to the distance between two adjacent resonant wavelengths and is defined by

$$\Delta\lambda = \frac{\lambda^2}{nL}, \tag{4.8}$$

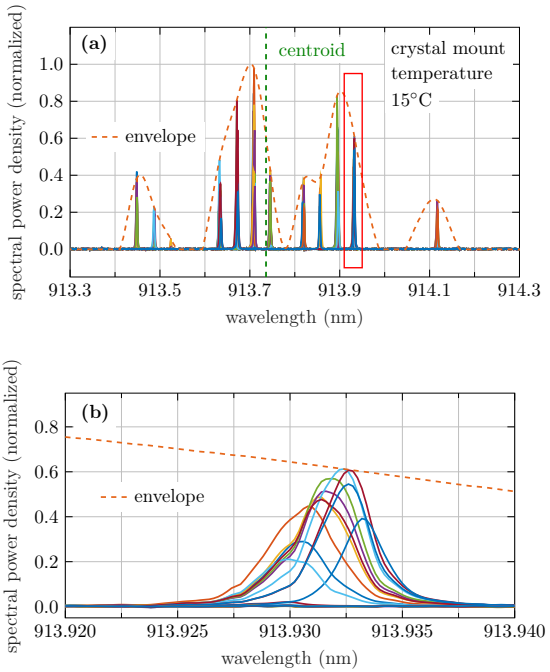

Figure 4.33: Laser spectra for different relative piezo scan positions at a crystal holder temperature of 15 °C (a) and a magnified view of the area indicated by the red box (b). The orange dashed line indicates the envelope used to calculate the centroid wavelength.

where λ is the vacuum wavelength of light, n is the group index of the medium in the resonator, and L is the physical distance which light travels for one cavity round trip. Using this formula a FSR of 25.8 pm is obtained for a vacuum wavelength of 914 nm, a resonator consisting of a 5 mm Nd^{3+}:YVO_4 gain crystal ($n = 1.9647$ [89]), a 6 mm air gap ($n = 1$) and a 0.2 mm Cr^{4+}:YAG saturable absorber ($n = 1.8180$ [170]). Figure 4.33 (a) shows an example of the superimposed laser spectra for different relative piezo scan positions at a preset crystal temperature of

15 °C. In this case, the spectrum was tuned over 14 relative piezo positions until it was congruent with the original spectrum again. For the calculated FSR of 25.8 pm, this corresponds to a resonator length change of about 1.84 pm per relative piezo step. The 14 recorded spectra were normalized to the maximum of the highest peak and plotted in different colors, though they could hardly be distinguished from each other spectrally due to the small tuning range. A Matlab post-processing script was used to calculate an envelope function, which is shown as an orange dashed line. The centroid of this envelope is indicated by the vertical green dashed line and was later used to investigate the temperature-dependent wavelength shift. The recorded spectra in the exemplary Figure 4.33 (a) do not continuously reproduce the complete gain bandwidth of the Nd^{3+}:YVO_4 crystal but instead are discrete due to the superposition of two parasitic cavity effects. Hereby, the coarse envelope (orange dashed line) leads to four different resonant regions, which show an average spacing of 0.215 nm (center of mass) to each other. In theory, this equals the spacing through a cavity with an optical mirror distance of 1.94 pm. From the fine envelope, eleven resonant regions are evident in Figure 4.33 which show an average spacing of 36.9 pm, corresponding to the resonances of a cavity with an optical spacing of 11.32 mm. Figure 4.33 (b) shows a magnified view of the entire spectrum shown in (a) (area marked by a red rectangle) and gives a good indication of the individual spectra. Further, this detailed view clearly shows that the longitudinal modes are completely limited to a certain spectral range.

Figure 4.34 shows the calculated centroidal wavelength of the envelopes (red dots) for various crystal holder temperatures between 10 °C and 80 °C. A linear fit (blue dashed line) results in an average wavelength shift of 1.7 pm $°C^{-1}$ and an intercept wavelength of 913.707 nm at 0 °C. Finally, a phonon-ion interaction model was used to compare the ex-

perimentally determined values and theory under the assumption of a Debye phonon distribution in the host crystal, which leads to phonon relaxation processes [166, 176]. Accordingly, the simplified temperature-dependent line shift can be expressed by

$$\delta\nu(T) = \delta\nu_0 + \alpha \left(\frac{T}{\theta_D}\right)^4 \int_0^{\theta_D/T} \frac{x^3}{e^x - 1} \mathrm{d}x, \tag{4.9}$$

where $\delta\nu_0$ is the line shift for low temperatures, α is the coupling coefficient of the phonon-ion interaction, and θ_D is the Debye temperature. The theoretical line shift from equation 4.9 was fitted to the experimentally measured points and the best result was obtained for θ_D = 425 K, α = 29 cm^{-1} and $\delta\nu_0$ = 0.02 cm^{-1} (see orange dashed line in Fig. 4.34). Figure 4.35 shows the temperature-dependent line shift over a larger temperature range from −250 °C to 200 °C including the theoretically fitted model and the experimentally determined values of the centroid wavelength. In the low-temperature range ($T << \theta_D$) the wavelength shift follows the typical T^3 dependence of the heat capacity in the solid, whereas for higher temperatures ($T >> \theta_D$) the high-

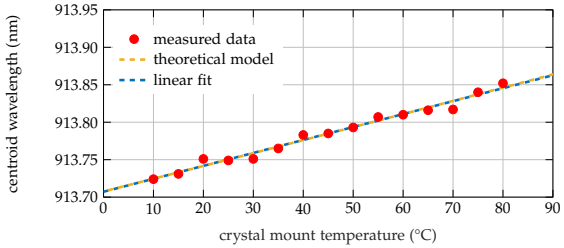

Figure 4.34: Central wavelength of the passively Q-switched laser as a function of crystal holder temperature. The red dots result from the centroid determination of various experimentally recorded spectra between 10 °C and 80 °C. The orange dashed line describes the temperature evolution according to the phonon-ion interaction model, while the blue dashed line corresponds to a linear fit.

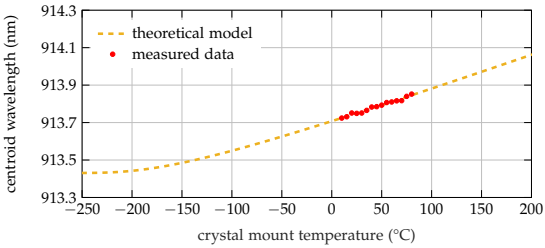

Figure 4.35: Evolution of the central wavelength according to the phonon-ion interaction model over a temperature range of 450 °C. The experimentally determined centroid wavelengths are plotted as red dots for comparison.

temperature regime with a wavelength shift proportional to T applies. While by determining the centroid wavelength of the envelope the linear relationship between central wavelength and temperature can be visualized well, no thermal broadening of the spectral emission line of the laser crystal could be detected with this method. A possible reason for this could be the coupling of the gain bandwidth with the FSR of different resonator components, which cause parasitic reflections and thus additional resonance conditions due to a non-ideal coating. This could be observed in the exemplary Figure 4.34, where the continuous emission spectrum is split into discrete regions.

4.5 SUMMARY AND OUTLOOK

In this Chapter, important system relationships and properties of the passively Q-switched solid-state laser were investigated concerning its application in an automotive lidar sensor. For this purpose, three different resonator configurations were used to enable the study of various

laser parameters as decoupled as possible from the overall system.

In the first experimental setup, a saturable absorber was inserted into the resonator and thus the influence on the spectral characteristics and efficiency of the system was investigated. Compared to CW operation, the saturable absorber significantly reduced the number of longitudinal modes. For shorter resonator lengths, for example, by using a short monolithic cavity design, operation on a single longitudinal mode can thus be expected. Since stability measurements over 60 minutes have shown that longitudinal modes competition is a possible cause of instabilities in the output parameters, a lidar system based on such a laser could exhibit promising overall stability.
In another resonator configuration, the influence of the applied pump power was considered and it was observed that the repetition rate scaled almost linearly with the applied pump power up to a frequency of about 60 kHz. At the same time, the pulse energy, pulse duration, and calculated peak power hardly changed over different pump powers, providing a high degree of flexibility concerning the repetition rate for different lidar approaches. Further experimental and numerical investigations of the resonator length, reflectivity of the output coupler mirror, and initial transmission of the saturable absorber showed that by a careful choice of parameters, short pulse durations in the low single-digit nanosecond range and pulse energies well above 100 µJ are in principle feasible. While good pulse-to-pulse stability of repetition rate, pulse duration, and pulse energy was observed for lower QC pump powers, satellite pulses and reduced stability increasingly occurred for pump powers above 650 mW.
For the temperature observation of the gain crystal, a third resonator configuration was used in which the gain medium was considered thermally isolated from the saturable absorber in the range of 10 to 80 °C. While an average central wavelength shift of just 1.7 pm was measured

for the different temperatures, a reduction in the stimulated-emission cross-section and consequently a nonlinear increase in the pump threshold could be determined with increasing temperature. At the same time, an increase in pulse energy, as well as a decrease in system efficiency and pulse duration, indicated that the use of active or passive temperature control of the passively Q-switched laser system is appropriate for application in a lidar sensor. Otherwise, for larger temperature changes, the output parameters of the laser and consequently the performance of the sensor can be expected to change significantly with temperature. On the other hand, very good beam quality with an M^2 better than two could be determined under a wide variety of conditions. Consequently, excellent lateral resolution can be achieved in the field for potential lidar applications, depending on the system approach.

In further measurements, it would be interesting to investigate the influence of the pump spot diameter in the gain crystal. Besides the initial transmission of the saturable absorber and the output coupler reflectivity, this quantity has a decisive influence on the output quantities of the system. Here, optimization of the pump spot at different pump powers could improve the spatial overlap and thus lead to increased system efficiency.
Furthermore, it would be useful to determine the detailed reasons for the occurrence of satellite pulses with increasing pumping rates, which vice versa could lead to a higher repetition rate. On the one hand, the gain difference between the longitudinal main mode and the competing mode could be increased. One possibility would be a shorter resonator cavity and consequently a larger FSR. On the other hand, alternative saturable absorber materials with shorter upper-state lifetimes could be examined.
In addition to that, the system could be optimized for the doping concentration of the gain crystal and the resulting thermal lensing at dif-

ferent pump powers. In this context, a consideration in dependence of the applied duty cycle would also be interesting. Also, apart from the investigated Nd^{3+}-doped YVO_4, $GdVO_4$ is another host material with promising properties. Herein, the equivalent quasi-three-level transition ($^4F_{3/2} \rightarrow {}^4I_{9/2}$) of Nd^{3+}:$GdVO_4$ is at 912 nm. A direct comparison of the two host materials could show how good $GdVO_4$ performs compared to YVO_4 for passive Q-switching and in an automotive lidar application.

5 PASSIVELY Q-SWITCHED MICROCHIP LASER FOR LIDAR SYSTEMS

In addition to the previous investigations of various resonator configurations in the previous chapter, another setup will be investigated in this chapter, where in contrast to the previous investigations, a free-beam single-emitter pump laser diode is used instead of a fiber-coupled pump laser to make the overall system even more compact. In addition, a monolithic microchip resonator is now used, where the saturable absorber was directly bonded to the gain crystal, analogous to Experimental Setup II. Together with the dielectric coated resonator mirrors of the Experimental Setup III, a compact and robust cavity can be created, for which short pulse durations are expected. With the help of this setup, the enormous potential for lidar applications in a single pulse operation will be demonstrated in the following.

5.1 EXPERIMENTAL SETUP

The experimental setup of the passively Q-switched microchip laser is shown in Figure 5.1. A single emitter pump diode with a central wavelength of 808 nm and maximum output power of 15 W was used (Sheaumann CL-808-015W-430). The characterization of this laser diode with associated measurements is shown in the Appendix 7.4. Initially, the pump laser was thermally coupled to a cooling water circuit, through

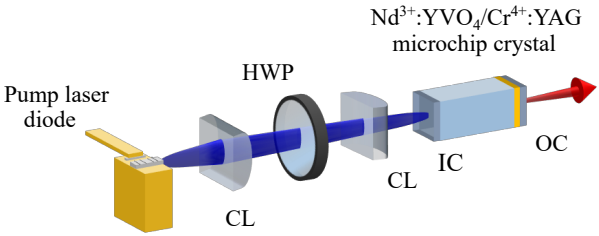

Figure 5.1: Experimental setup of the passively Q-switched Nd^{3+}:YVO_4/Cr^{4+}:YAG microchip laser. CL: cylindrical lens, HWP: half-wave plate, IC: input coupler, OC: output coupler.

which the laser temperature and consequently the central wavelength could be adjusted. In later measurements, the temperature control of the pump laser was used to test at which ambient temperatures the temperature influence on the pump laser and consequently on the passively Q-switched laser can be compensated by adjusting the pump laser current only. Compared to a fiber-coupled pump laser, the single emitter pump laser is much more compact, cheaper, and has a narrower spectral bandwidth.

Two cylindrical lenses with focal lengths of 15 mm and 35 mm were used to image the rectangular pump laser aperture onto a square pump spot of approximately 220 µm ($\sim 1/e^2$). Using a half-wave plate, the preferred direction of pump polarization could be adjusted to optimize the system during subsequent laser operation. For later applications, the half-wave plate can be omitted and the laser crystal can be rotated instead. The microchip resonator consisted of a 3 mm long and 0.15 %at. doped Nd^{3+}:YVO_4 crystal (a-cut, Casix Inc.) which was bonded to a Cr^{4+}:YAG saturable absorber with an initial transmission of 98 %. For the length and doping of the gain medium, a trade-off was made between absorption of the pump light, reabsorption of the laser light and pulse duration.

Basically, the gain medium should be selected with a length and dop-

ing concentration such that the incident pump power is completely absorbed. On one hand, by choosing a longer gain crystal the complete pump power is absorbed but the non-pumped end of the crystal leads to reabsorption of the laser light while comparatively little pump light is absorbed. Also, a longer gain medium extends the resonator length and thus increases the pulse duration, which is proportional to the resonator round-trip time of the photons. If, on the other hand, the doping concentration is increased, the reabsorption also increases, and, in the case of too high doping, quenching effects occur that reduce the fluorescence lifetime and consequently the pulse energy. According to Lambert's law, for the selected gain crystal length of 3 mm and doping concentration of 0.15 %at., about 93 % of the pump power is absorbed in the crystal, while the pulse duration remains quite short and the reabsorption comparatively small.
The microchip crystal was wrapped with indium foil and mounted in a copper holder along with the kinematic two-axis mount which was already used for the laser experiments of Chapter 4. The dielectric coupling coating of the gain medium was transparent to pump light and highly reflective for 914 nm while the output coupler mirror had a transmissivity of 7 % at the laser wavelength. To suppress parasitic laser oscillations, the dielectric resonator mirrors were specified with an AR coating (R$<$0.5 %) at 1064 nm and 1342 nm.

Consistent with the literature, the value for the stimulated-emission cross-section ($^4F_{3/2} \rightarrow {}^4I_{9/2}$ transition) was calculated to 4.8×10^{-20} cm^2 [34] while an upper laser level lifetime of 100 µs at 293 K [177] was obtained. Furthermore, a thermal fractional population of 0.406 and 0.048 were calculated at room temperature (293 K) for the lower and upper Stark splittings of the ground state ($^4I_{9/2}$), respectively. The upper splitting is simultaneously the lower laser level in the quasi-three-level system.

5.2 EXPERIMENTAL INVESTIGATIONS

To demonstrate the potential for lidar systems, the passive Q-switched microchip laser was operated at a repetition rate of 200 Hz and investigated for stability properties that are important for various applications in the lidar context. Hereby, the repetition rate of 200 Hz was not the upper stability limit of the system in terms of repetition rate, but a deliberately chosen parameter since further measurements are planned in a proof-of-principle lidar application.

While passively Q-switched solid-state lasers usually have repetition rates in the kilohertz range during continuous pumping, a QC pumping scheme was used in this work to set a pulse repetition rate of 200 Hz with the single-pulse operation. Figure 5.2 shows the time evolution

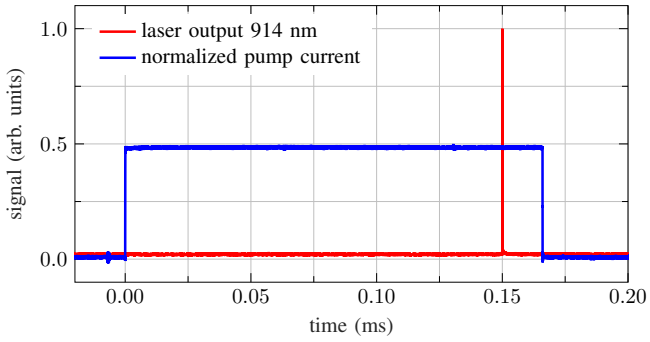

Figure 5.2: QC pumping scheme for generating single laser pulses with a repetition rate of 200 Hz and a low duty cycle of about 3.4 %. The current applied to the pump laser is displayed in blue, while the pulsed laser output is shown in red.

of the pump current applied by the laser driver (Ostech ds11-la14v14) in blue, while pumping was performed for a time duration of 170 µs. Shown in red is the generated laser signal at 914 nm which was separated from the remaining pump signal behind the microchip laser by a bandpass interference filter (Edmund Optics 900 nm x 25 nm) and recorded with a fast InGaAs detector (5 GHz bandwidth, Thorlabs) in combination with an 6 GHz oscilloscope (LeCroy WavePro 804HD). QC pumping with a period of 5 ms (200 Hz) resulted in a low duty cycle of only 3.4 % which minimized the thermal load in the crystal and prevented the need for active cooling of the monolithic crystal. The amplitude of the current was chosen such that the laser pulse was generated with respect to the rising current edge after a delay time of 150 µs. The required current amplitude to generate a laser pulse with a delay time of 150 µs is strongly dependent on the pump laser temperature. Since the pump laser in use is an edge emitter, a temperature-dependent wavelength shift of 0.3 nm K^{-1} is expected while the output power and efficiency additionally decreases for increasing temperatures [178]. Consequently, a change in ambient temperature has a large impact on the overall solid-state laser performance if the pump laser is not actively temperature stabilized. Since in this work an active temperature control was not intended, it was investigated to what extent the temperature influence of the pump laser could be compensated by a current adjustment to keep the generated laser pulse at a constant delay of 150 µs.

Figure 5.3 shows the experimental investigations in this context. Here, the current required at the pump laser is plotted against the temperature of the pump laser. In this measurement, the pump laser was temperature-controlled in one degree Celsius steps using a cooling water circuit to temperatures between 20 °C and 50 °C. Subsequently, the pump current at the laser driver was adjusted to maintain a constant pulse delay of 150 µs from the rising pump edge to the generated laser

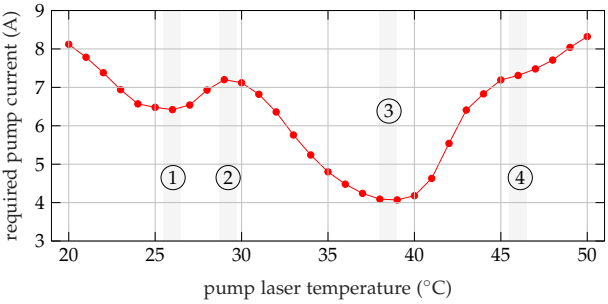

Figure 5.3: Required pump laser current as a function of pump laser temperature to generate laser pulses with a constant delay of 150 µs with respect to the switch-on of the pump laser. The numbers 1 to 4 mark distinctive positions at which different effects dominate in the interaction between the pump laser and the properties of the laser crystal.

pulse. The numbers from ① to ④ mark distinctive points at which different effects in the interaction between the pump laser and the properties of the laser crystal dominate. The shape of the measured curve results from the superposition of the intrinsic Nd^{3+}:YVO_4 absorption spectrum and the temperature dependence of the pump laser in terms of wavelength and output power.

In the following discussion different features in the absorption spectrum of Nd^{3+}:YVO_4 are mentioned which have been studied by McDonagh and Wallenstein in detail for c-cut and a-cut crystals [179].

The lowest pumping current and thus the global minimum was reached in our experiment for a pumping temperature of 39 °C and is marked by position ③. This minimum results from the good spectral overlap between the narrowband pump lasers with the maximum absorption peak of Nd^{3+}:YVO_4 at 808 nm. Starting from this point, if the cooling water temperature was reduced, the applied pump power increased slightly but the overlap between the narrowband absorption peak and the single emitter became worse. Consequently, the required pumping

current increased. At position ②, the pump power was greater than at point ③ for the identical current, but due to the blue shift of the pump wavelength, a larger current was required for delay compensation of the laser pulse. With decreasing temperature, a local minimum of 6.42 A was again reached in ① at 26 °C. This was a result due to a side-wing peak of the absorption spectrum in combination with the increasing output power of the pump laser for lower temperatures. A further lowering of the temperature finally led to a significant reduction of the spectral overlap, which could no longer be compensated by the slightly increasing pump power due to a lower temperature.
From the global minimum in ③, a larger pump laser current was also required with increasing temperature to maintain the laser pulse at a constant level due to spectral shifting. In region ④, a slight correction of the rising current slope could be observed, which probably also arises from a lateral absorption peak next to the main maximum at 808 nm (see the spectrum in [179]). For increasing temperatures, the semiconductor laser spectrum shifted to a larger wavelength and the overlap with the absorption band of Nd^{3+}:YVO_4 deteriorated. Additionally, the output power of the pump laser decreased for increasing temperatures while no adaptation of the electric current was made.
In addition to the temperature effects of the pump laser, another experiment was conducted to investigate the temperature effects of the microchip laser crystal on the pulse delay time. By adjusting the cooling water temperature of the crystal holder in the range of 20 °C to 50 °C, only a small influence on the delay time of the solid-state laser pulse was observed. This effect could be compensated easily by a slight adjustment of the pump laser current in the range of several 0.05 A.
In total the experiment revealed that the overall laser system can be operated stably without active temperature control in the range 20-50 °C simply by adjustment of the pump laser current.

5.2.1 Output characteristics

In the following, the output parameters such as pulse duration, spectral width, and beam quality are examined. Moreover, the stability of the pulse energy, pulse duration, and the resulting peak power, as well as the stability of the wavelength were measured.
All subsequent measurements were performed with a pump laser current of 7.91 A corresponding to an average pump power of 269 mW. With the applied duty cycle of 3.4 % (170 µs / 200 ms), this resulted in a peak pump power of 7.9 W.
For lidar sensors, the pulse duration is an important parameter, since it has a considerable influence on the longitudinal resolution of the system. For that reason, an estimate of the pulse duration is performed in the beginning. In the case of passively Q-switched lasers, the exponentially growing photon field typically requires several resonator cycles until the majority of the stored energy in the gain medium is extracted. As a rough estimate, in the case of passive Q-switching with strong saturation, the pulse duration τ_p can be estimated by

$$\tau_p \approx 4.60 \, \frac{T_\mathrm{r}}{q_0}. \tag{5.1}$$

Here, T_r is the photon resonator round trip time and $q_0 \sim$ (1 - T_0) are the saturable losses considering an initial transmission T_0 and no non-saturable losses of the saturable absorber.
For the microchip laser used here, we obtain an estimated pulse duration of 9.64 ns, taking into account the refractive index of Nd^{3+}:YVO_4 and the initial transmission of 98 %. It was expected that a short pulse duration is possible due to the short resonator length of the microchip laser and thus the short signal round-trip time. Likewise, lower initial transmissions lead to a larger population inversion in the laser crystal

and thus to a faster buildup of the electric field in the cavity.

The experimental measurement of the pulse duration is shown in Figure 5.4 and is an enlargement of the pump scheme from Figure 5.2 around the range of the generated laser pulse. Assuming a Gaussian pulse shape, fitting results in a pulse duration of 7.47 ns (FWHM) which is in reasonable agreement with the estimated value of 9.64 ns.
The long-term stability of pulse energy, pulse duration, and the resulting peak power is shown in Figure 5.5 and was measured simultaneously for 60 minutes. For this purpose, both the pump laser and the microchip crystal were disconnected from the cooling water supply and the system was operated at room temperature (20.5 °C according to the laboratory thermometer). The laser was warmed up for 10 minutes to reach thermal equilibrium before the measurement was started. For the stability measurement, a pump current of 7.91 A was required at the laser driver, in agreement with Figure 5.3, to generate laser pulses with a delay time of 150 µs. A pyroelectric energy sensor (Ophir PE9-C) was used to measure the pulse energy. In the upper part of Figure 5.5, the measurement of the pulse energy is depicted in green. Over 60 minutes,

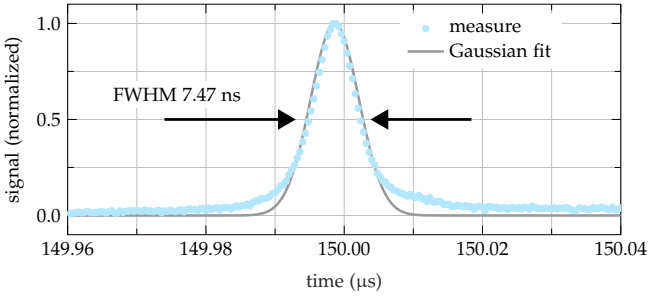

Figure 5.4: Oscilloscope trace of a laser pulse (light blue) with a pulse duration of 7.47 ns (FWHM). The pulse duration was determined by a fit (gray) assuming a Gaussian pulse shape.

an average pulse energy of 4.83 µJ was determined with a standard deviation of 0.03 µJ. This corresponds to a fluctuation of just 0.62 % which is a remarkable value considering the absence of active temperature control [180]. The obtained pulse energy was comparatively small but for future experiments, it should in principle be possible to increase this significantly. For this purpose, on one hand, the pump spot can be enlarged, thus increasing the effective area on the saturable absorber. On the other hand, a smaller value for the initial transmission of the saturable absorber and a larger output coupler transmissivity could be

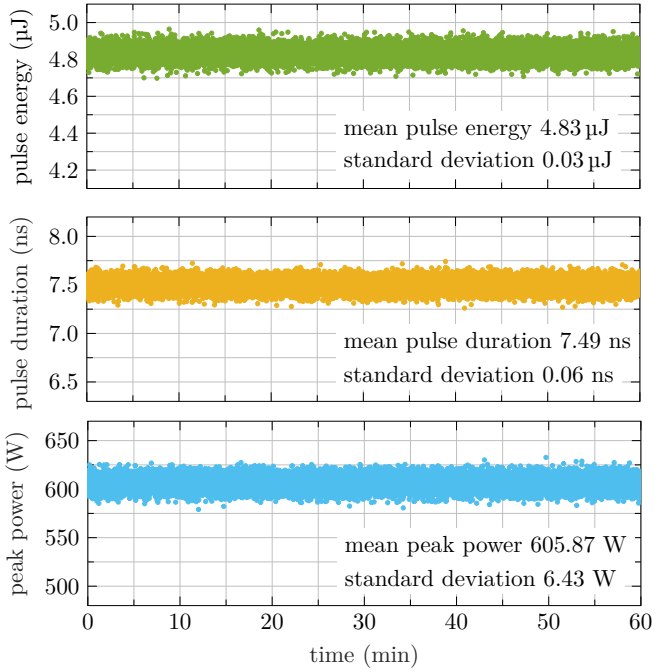

Figure 5.5: Pulse energy (top), pulse duration (middle), and the calculated peak power (bottom) recorded over 60 minutes.

chosen. In this way, pulse energies in the 10-100 mJ regime have already been generated for other passively Q-switched lasers [21, 22, 181].
The stability measurement of the pulse duration is shown in yellow in the center of Figure 5.5 and was recorded analogously to Figure 5.4 using the fast InGaAs detector with a bandwidth of 5 GHz. A mean pulse duration of 7.49 ns and a standard deviation of 0.06 ns ($\widehat{=}$ 0.80 %) were measured over one hour.
Further, for a given pulse energy and pulse duration, the peak power can be determined assuming a Gaussian pulse shape, by using [47]

$$P_p \approx 0.94 \, \frac{E_p}{T_p}. \tag{5.2}$$

Here, E_p is the pulse energy, T_p is the pulse duration and 0.94 is a correction factor taking into account a Gaussian pulse shape. Since the pulse energy and pulse duration were measured simultaneously, equation 5.2 can be used to calculate the corresponding peak power, which is shown in light blue in the lower part of Figure 5.5. The mean calculated peak power is 605.87 W, which corresponds to a peak power stability with a standard deviation of 6.43 W corresponding to 1.06 %. The high stability of pulse duration, pulse energy, and peak power results from the short monolithic resonator configuration, which allows the laser to run stably in a longitudinal mode for more than 60 minutes.

Next, the spectral properties were investigated. In general, if the resonator of solid-state lasers with a narrow bandwidth gain medium is kept very short, it can operate on a single longitudinal mode with a spectral width of only a few picometers [182, 70]. Additionally, passive Q-switching, compared to CW operation, causes the laser to further reduce the number of modes. In theory, the mode that bleaches the saturable absorber has some advantage in terms of photon number over competing longitudinal modes in the race for the laser gain. Thus, this

single-mode already reduces almost the complete population inversion in the gain crystal by its exponential growth, while other modes are additionally suppressed by the missing gain [118, 183]. Previous measurements in Section 4.2.2 have shown that the insertion of a saturable absorber, compared to CW operation, greatly reduces the number of longitudinal modes.

For applications, the combination of a single longitudinal mode along with the small temperature-dependent wavelength shift of solid-state lasers (a few picometers per degree Kelvin [25]) allows the use of extremely narrowband spectral filters and thus an excellent signal-to-noise ratio at the detector.

In this work, the spectrum of the passively Q-switched microchip laser was recorded with a high-resolution hyperfine spectrometer (Lightmachinery HF-8991-3, 1.5 pm minimum resolution according to manufacturer). The resulting spectrum is shown in Figure 5.6 and indicates that the laser operates in a single longitudinal mode. The calculated central wavelength of this mode was 913.986 nm, while a spectral width (FWHM) of 3.3 pm was observed.

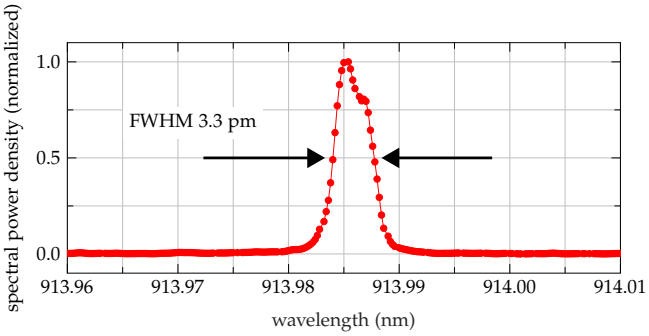

Figure 5.6: Spectrum of a single-longitudinal mode with a spectral bandwidth of 3.3 pm (FWHM) at a center wavelength of approximately 914 nm.

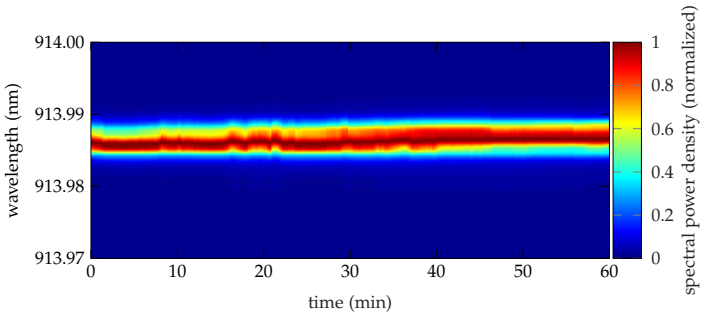

Figure 5.7: Stability measurement of the laser spectrum recorded over 60 min at a sampling rate of 1 Hz without active cooling of the pump laser and the monolithic crystal.

Similar to the previous stability study of the pulse energy, pulse duration, and peak power, the spectral stability of the longitudinal mode was investigated for 60 minutes. Figure 5.7 shows the temporal stability of the spectrum, where individual spectra were recorded at a sampling rate of 1 sample/second and then lined up to an intensity map in a post-processing using Matlab. The post-processing of the individual spectra was performed with a Gaussian fit and yielded a standard deviation of 1.5 pm around the central wavelength of 913.986 nm with a spectral bandwidth mean value of 3.4 pm. The high stability of the central wavelength and spectral width most likely results from the short monolithic resonator configuration, which greatly increases the spacing of longitudinal modes.

Finally, for the beam quality measurements, the pulsed laser light was coupled into a beam propagation analyzer (Ophir BSQ-SP920) after the bandpass filter which blocked the residual pump light. Beam analysis was performed using a 400 mm lens in triggered operation mode to determine the beam quality, divergence angle, and back-calculated res-

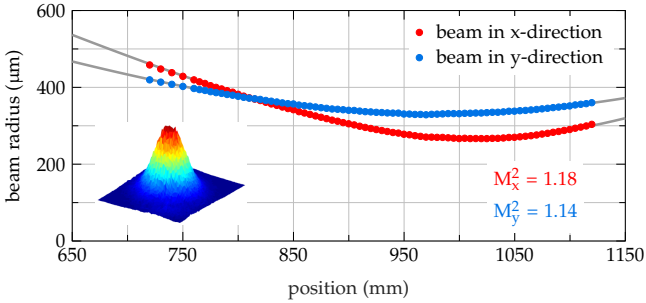

Figure 5.8: Beam quality measurement with associated beam radii in x- and y-direction as a function of position z. The inset shows the transverse near Gaussian beam profile at a position of 900 mm.

onator foci.

Figure 5.8 shows the measured beam radius in the x and y-axis as a function of propagation position. The inset is taken at a position of 900 mm and shows the transverse beam profile with a nearly Gaussian intensity distribution. In both directions, the beam was nearly diffraction-limited with an M^2 of 1.18 and 1.14 and a full divergence angle of 2.03 mrad and 1.64 mrad in the x and y directions, respectively. The back-calculated waist diameters at the foci of the laser were 168.8 µm and 202.6 µm (x- and y-direction), which is approximately a factor of 1.69 or 2.3 greater than the original predefined pump spot radius of about 100 µm. Using this information, in future experiments the pump optics can be adjusted and optimized, presumably reducing the asymmetry between the two beam directions. For lidar applications the excellent near Gaussian beam quality can be used to obtain high-resolution images as the beam could be focused to almost the minimum spot size in both respective directions.

5.3 FUTURE LIDAR SYSTEM DESIGN

To demonstrate the potential for a possible lidar application, a proof of principle single pulse lidar system based on the monolithic laser is planned to be realized in the future. For this purpose, Figure 5.9 shows a possible extended schematic laser setup, where the original setup from Figure 5.1 has been extended by a bandpass filter, a photodiode, an aspherical lens, and a cylindrical lens after the monolithic laser crystal. The goal of these extensions is on the one hand the detection of the laser pulse in time to perform a time-of-flight lidar measurement and on the other hand beam shaping of a laser line with a specific horizontal field of view (FoV).
Compared to actively Q-switched lasers or pulsed semiconductor lasers, passively Q-switched lasers have a non-negligible temporal jitter in the laser pulse, which is on the order of a few nanoseconds to several microseconds [62, 150]. To determine the object distance as accurately as possible with a lidar system using a time-of-flight measurement, the temporal jitter must be very small ($\ll 1\,\mathrm{ns}$) or monitored and factored out. To minimize this temporal jitter, different approaches such as self-injection seeding [63], direct bleaching of the saturable absorber [64, 184], modulation of the pump signal [62], or a coupled cavity [185] have been successfully applied in the past.

For this future proof-of-principle lidar system, the temporal jitter needs not be reduced but should be recorded by a parasitic reflex with a photodiode and used as starting time for the subsequent time-of-flight measurement. First tests with the bandpass filter interference filter (Edmund Optics 900 nm x 25 nm) behind the monolithic laser crystal have

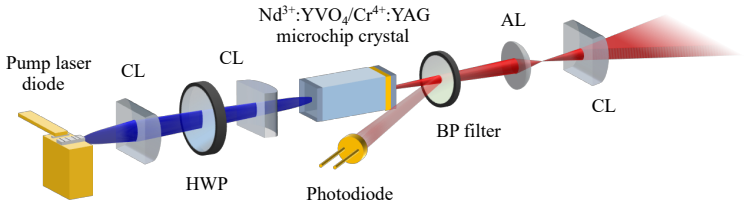

Figure 5.9: Experimental setup of the passively Q-switched Nd^{3+}:YVO_4/Cr^{4+}:YAG microchip laser for application as a line-flash lidar system. CL: cylindrical lens, HWP: half-wave plate, BP: bandpass, AL: aspheric lens.

shown that it not only separates the remaining pump light from the laser wavelength but additionally a weak parasitic reflection of the laser signal can be generated by slightly tilting it. Subsequently, this weak reflection could be detected with a fast photodiode (Thorlabs DET08CL).

For beam shaping of a laser line, an aspherical lens and a subsequent cylindrical lens were used. Hereby, the aspherical lens (f=4.5 mm, Thorlabs 350350-B) focused the beam strongly and generated a full divergence angle of about 19° in both directions behind the focus. Subsequently, a plano-convex cylindrical lens (Thorlabs LJ1477L1) with a focal length of 70 mm was used to collimate the beam in the vertical direction. Calculations based on the ray transfer matrices have shown that with this lens combination, assuming an M^2 of 1.2, a laser line with a horizontal FoV of 19° and a vertical collimated beam with a divergence angle of only 0.005° can be generated. Furthermore, the combination of an aspherical and a cylindrical lens provides the advantage that the power density at the output aperture of the system can be scaled to meet the eye safety requirements of a potential lidar system.

Figure 5.10 shows a schematic functional sketch of a possible lidar system setup. The monolithic laser shown above has a peak power of 600 W with a pulse duration of 7.5 ns and a M^2 of 1.2. Through the monitor diode, the start time of the time-of-flight measurement can be deter-

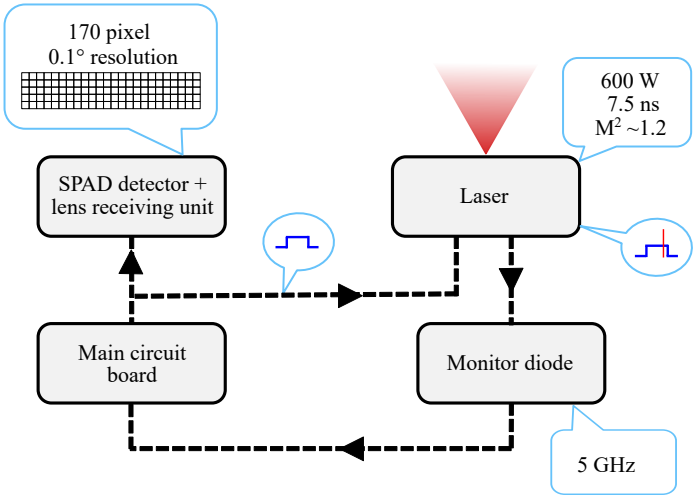

Figure 5.10: Schematic functional sketch of a possible lidar setup based on a passively Q-switched line flash and a multi-line SPAD detector.

mined and transferred to the main board where subsequent calculations of the object distance take place. The laser line emitted into the field is reflected by possible objects and then picked up by a possible Silicon-based SPAD detector equipped with upstream receiving optics. A possible detector with 170 horizontal pixels and multiple planes could thus cover a horizontal FoV of 17° at a potential vertical resolution of 0.1°. While the low peak power for such a line flash lidar would necessarily result in a very short detection range, the planned system is merely a proof-of-principle concept. As mentioned above, several papers have already shown that pulse energies between 10-100 mJ are possible in single pulse operation for passively Q-switched lasers above 1000 nm [21, 22, 181]. To some extent, this should be transferable to the wavelength of 914 nm.

5.4 SUMMARY AND OUTLOOK

In this chapter, a passively Q-switched microchip laser composed of Nd^{3+}:YVO_4 and Cr^{4+}:YAG was demonstrated. The system shows a high potential for lidar system applications. By QC pumping at a frequency of 200 Hz, the thermal load in the crystal was minimized and no active cooling was required to operate the system. Furthermore, it was shown that the whole microchip laser could be operated without cooling in a temperature range between 20-50 °C by adjusting the pump current only. The short monolithic resonator produced short pulse durations well below 10 ns and operation on a single longitudinal mode with a spectral width of only a few picometers was possible. The quasi-three-level operation of the system allowed an emission wavelength of 914 nm ensuring compatibility with state-of-the-art Silicon detectors. Further, beam quality studies showed that the laser is nearly diffraction-limited with an M^2 better than 1.2 in both directions. Stability measurements of pulse energy, pulse duration, peak power, and wavelength underlined the great potential of this system. The passively Q-switched microchip laser shown here served as a kind of proof-of-principle for the underlying potential and forms the basis for future investigations and possible optimizations. Thus, by adjusting the initial transmission, the pump spot, and the output coupler reflectivity, it should be possible to generate larger pulse energies, resulting in a significantly reduced pulse duration, while the repetition rate offers a wide range of applications by QC pumping.

For future investigations, the edge emitter pump laser diode could be replaced by a surface-emitting semiconductor laser array with a quadratic pattern. This would have the advantage that a single spherical

pump lens could be used instead of the two cylindrical lenses to image the pump light squarely in the laser crystal. In addition, by rotating the laser crystal, the half-wave plate can be dispensed with, in principle creating an overall system structure with a footprint of a few centimeters only. Furthermore, the smaller temperature-dependent pump wavelength shift of the surface emitter (0.07 nm/K vs. 0.3 nm/K) would lead to a larger operating range while matching the ambient temperature (see Figure 5.3). Also, it would be conceivable to use a wavelength-stabilized laser diode.

As mentioned above, in terms of the range of the lidar demonstrator, it would be useful to scale the pulse energy and consequently the peak power. For this purpose, the pump spot diameter in the crystal, the initial transmission of the saturable absorber, and the OCM could be optimized.

In addition to this, it would be interesting to record the average output power as a function of input power at different temperatures to get a better and more detailed system understanding concerning pulse energy scalability and pulse build-up time. Moreover, the temporal jitter between the individual pulses could be recorded and analyzed as a function of the pump power.

6 SUMMARY AND OUTLOOK

In this work, a passively Q-switched Nd^{3+}:YVO_4 laser was realized for application in an automotive lidar sensor. While most solid-state lasers have emission wavelengths above one micrometer, in this case, a quasi three-level system at a wavelength of 914 nm was deliberately addressed. Compared to lidar wavelengths above 1000 nm, this offers the advantage of reduced atmospheric water absorption and also allows the use of widely established and inexpensive silicon-based detector technology.

In the first part of this work, three resonator configurations were used to investigate relevant laser parameters for a possible lidar application. Thereby, the configurations were chosen in such a way that individual laser parameters could be investigated as decoupled as possible from the overall system.

In the first resonator configuration, the improved selectivity of longitudinal modes in passive Q-switching compared to CW operation was demonstrated using a retractable saturable absorber. By introducing the saturable absorber into the resonator, the number of modes was significantly reduced, indicating that operation on one or a few longitudinal modes can be expected for shorter resonators. However, this also indicated that the passive Q-switching significantly reduces both the conversion efficiency and the slope efficiency. Although a maximum conversion efficiency of more than 20 % for the passive Q-switching is quite a remarkable result, the comparison with theory revealed that there is further potential for optimizing the overlap between the pump and resonator modes.

With the second resonator configuration, the resonator length could be changed without affecting the fluence on the saturable absorber and a linear relationship to the obtained pulse duration was shown. In a lidar application, the pulse duration plays an important role. For short pulse durations, both a high longitudinal resolving power and at the same time a large sensor range can be enabled on account of large peak power. To maximize the peak power, the laser pulse duration can be reduced and the pulse energy can be increased. Experimental as well as simulative investigations have shown that the achievable pulse energy can be considerably modified by the reflectivity of the output coupler and the initial transmission of the saturable absorber. However, these two parameters in turn strongly affect the laser threshold. Consequently, an optimum of pulse energy, pulse duration, and laser threshold can be met by a sophisticated choice of components and resonator length.
Concerning the adjustable repetition rate, the system showed a nearly linear relationship between repetition rate and pump power up to a maximum of about 60 kHz. At the same time, the pulse duration, as well as the pulse energy, remained almost unaffected by the applied pump power, which means that a wide frequency range for possible lidar applications can be set via this parameter. This behavior of the repetition rate, pulse duration, and pulse energy could be reproduced very well by simulations based on a rate equation model up to a pump power slightly above three times the pump threshold. However, above three times the pump threshold, experiments revealed an increased excitation of different longitudinal modes that can lead to satellite pulses and instabilities in the laser dynamics. As a result, an increasing deviation between simulations and experiments could be observed in this range with increasing pump power. Also, in later measurements of the long-term stability of the laser output parameters, it was observed that longitudinal mode competition can lead to undesired instabilities in the central wavelength, pulse energy, pulse duration, and peak power.

A third resonator approach was used to investigate the temperature-dependent properties of the passively Q-switched laser. Over a temperature range of 70 °C, a small shift of the central wavelength of just 1.7 pm °C^{-1} was observed for the gain crystal. Together with a stable narrowband emission bandwidth, an excellent signal-to-noise level at the detector can be achieved in the application in combination with a narrowband bandpass filter. Furthermore, the passively Q-switched laser also showed an excellent beam quality in this temperature range with an $M^2 < 2$. For a potential lidar application, this enables an excellent resolution to be obtained in the field.

In an advanced approach, a passively QC switched monolithic resonator setup was investigated as a demonstrator for future lidar experiments and applications. While passively Q-switched solid-state lasers typically provide repetition rates in the kilohertz range through continuous pumping, in this study the QC pumping process allowed single-pulse operation at a repetition rate of 200 Hz. Due to the short monolithic resonator, pulse durations in the single-digit nanosecond range were achieved, which resulted in a peak power of over 600 W even despite the low pulse energy of a few microjoules. However, future experimental and numerical investigations of the pump spot diameter, the initial transmission of the saturable absorber, and the reflectivity of the output coupler mirror should provide significantly larger pulse energies.
In addition, it was shown that the short resonator allows stable operation on a single longitudinal mode with a spectral width of a few picometers only. Along with the extremely small temperature-dependent wavelength shift, this allows the use of extremely narrowband spectral filters in lidar applications, resulting in an excellent signal-to-noise ratio at the detector. Furthermore, it was shown that operation on a single longitudinal mode, compared to the multi-longitudinal operation of a longer resonator (Chapter 4), can lead to improved stability of the out-

put parameters. Moreover, experimental studies on the switching timing of the laser have shown that the pump laser diode and the monolithic laser crystal can be used over a temperature range of 20-50 °C without active temperature control, but only by adjusting the pump current. For future measurements, it is quite conceivable to replace the used edge emitter pump laser diode with a surface emitter semiconductor laser array with a square aperture. Due to the smaller temperature-dependent wavelength shift of surface emitters in contrast to edge emitters (0.07 nm/K vs. 0.3 nm/K), the overall system could consequently be used at a significantly larger temperature range without active temperature control. In addition, due to the square aperture, a single spherical pump lens, instead of the two cylindrical lenses, should be sufficient to image the pump light squarely in the laser crystal. This would make the entire laser setup much more compact.
In the future, it is possible to use the monolithic laser demonstrator to realize a lidar application, as described in more detail in Chapter 4. In this case, the demonstrated approach for generating a laser line could produce excellent resolution in the field due to the nearly diffraction-limited beam quality with an $M^2 < 1.2$.

In addition to the previously mentioned possibilities of system optimization of the discrete experimental setup and improvement of the monolithic laser demonstrator concerning a possible lidar application, there are additionally larger projects which are conceivable in the future. Some general ideas are described in the following:

- **Compact microchip laser system directly pumped by a high-power VCSEL array**
  High-power 808 nm VCSEL arrays with QCW powers up to 100 W are state-of-the-art and commercially available today. By developing a suitable microlens array, this VCSEL array could be bonded or glued directly to the coupling facet of the monolithic resonator

structure to enable a highly compact overall system that is also extremely robust.

- **Master Oscillator Power Amplifier System**
  A commercially available 914 nm laser diode or the passively Q-switched laser setup shown could serve as a seed source for a master oscillator power amplifier system based on a Nd^{3+}:YVO_4 amplifier crystal. Consequently, relatively high-energy laser pulses could be achieved with a relatively small thermal load in the seed laser. When it appears necessary to suppress amplified spontaneous emission (ASE), the amplifier crystal could be cut at an angle into different segments and then bonded back together after applying a dielectric coating that reflects ASE. Hereby, depending on the desired pulse energy, a single- or multipass amplifier system is conceivable.

- **Saturable absorbers around 900 nm**
  The physical properties such as ground-state and excited-state absorption cross-section, as well as the recovery time of the saturable absorber, have a fundamental influence on the passive Q-switching and consequently on the output parameters of the laser. Further investigations of the Cr^{4+}:YAG absorbers used for applications around 900 nm could yield significant system optimization in this respect. Additionally to Cr^{4+}:YAG, several other saturable absorber materials could be taken into consideration for passive Q-switching around 900 nm. These include a variety of host materials doped with chromium and vanadium. Furthermore, even more exotic absorber materials based on semiconductor quantum structures, organic dye solutions, color centers, or graphene layers can be considered to be suitable.

APPENDIX 7

7.1 SETUP AND DEVICES FOR CHARACTERIZATION

The setup for characterizing the different laser setups from Chapter 4 and Chapter 5 is shown schematically in Figure 7.1. The exact specifications of the equipment and instruments used are summarized in Table 7.1.

Using a flip mirror the beam could be deflected to determine important parameters like the beam quality factor M^2, the divergence angle, and the waist in focus employing beam quality analysis. The use of two non-polarizing beam splitter cubes (Thorlabs BS017) allowed simultaneous analysis of laser power, pulses in time, and the associated spectrum. The

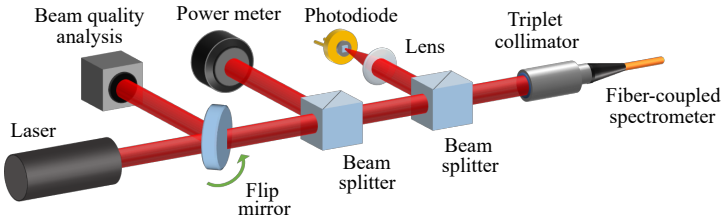

Figure 7.1: Experimental setup for characterization of the laser experiments shown in Chapter 4 and Chapter 4. The designations and specifications of the measuring devices used are summarized in Table 7.1.

type	designation	specification
beam quality analysis	Ophir BeamSquared SP920	λ : 266-1100 nm 400 mm NIR lens
power meter	Ophir 3A-P	λ : 0.15-8 µm P_{CW} : 15 µW-3 W
power meter	Ophir 10A-P	λ : 0.15-8 µm P_{CW} : 40 µW-10 W
energy meter	Ophir PE9-C	λ : 0.15-12 µm E_P : 0.2 µJ-1 mJ max. frequency: 25 kHz
photodiode	Thorlabs InGaAs DET08C/M	λ : 800-1700 nm 5 GHz
oscilloscope	LeCroy WavePro 604HD	bandwidth: 6 GHz 20 GS/s
spectrometer	Ocean Optics HR4000	λ : 770-854 nm slit: 5 µm $\Delta\lambda$: 50 pm
spectrometer	Hyperfine HF-8991-3	λ : 800-1000 nm $\Delta\lambda$: 2 pm

Table 7.1: Overview of the used measurement devices including the specifications.

decoupling into the fiber-coupled spectrometer was done here using a triplet collimator (Thorlabs TC06APC-980).

7.2 QUASI-CONTINUOUS PULSE TRAIN ANALYSIS

For the analysis of the QC pulse trains, a post-processing program was developed in Matlab. With the help of this evaluation, the temporal dynamics of the laser can be investigated in terms of repetition rate, pulse duration, pulse energy, and peak power, and thus possible disturbing influences such as longitudinal mode competition or satellite pulses can be identified.

In addition to stable laser operation, this method requires a photodi-

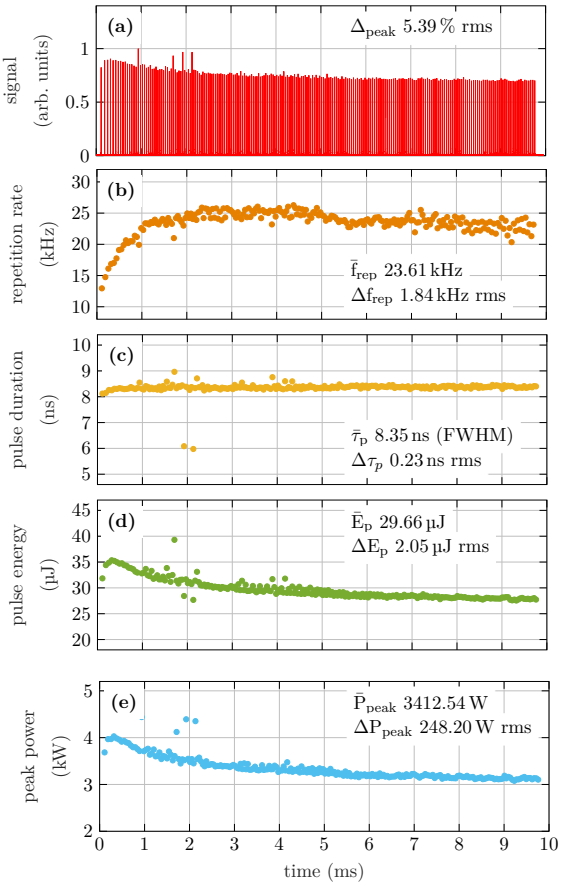

Figure 7.2: Exemplary post-processing analysis of a QC pulse train at a pump duration of 10 ms. The pulse train recorded with a fast photodiode is shown in (a). The repetition rate calculated from the single pulse position is shown in (b). Subframe (c) shows the pulse duration obtained by a multitude of Gaussian fits. The pulse energy obtained by integrating the individual pulse areas is shown in (d). Figure (e) shows the peak power calculated from pulse energy and pulse duration.

ode and an oscilloscope with large bandwidth and storage capacity to sample the entire pulse train with sufficiently high resolution. Figure 7.2 (a) shows an example of a solid-state laser pulse train recorded with a sampling rate of 10 GS/s for a pump duration of 10 ms. In the post-processing program, the captured pulse train (a) is first normalized and then a peak finder is used to identify the individual pulse positions. A Gaussian fit is applied around each of these peak positions to determine the pulse height, pulse width (FWHM), and exact pulse position. The fitted positions of the individual pulses are used to determine the mutual pulse spacing, which is the inverse of the repetition rate, shown in (b). Through this plot, it can be seen that the first pulses have a much larger mutual spacing and a steady state is reached within a few milliseconds. For the exemplary pulse train, the mean repetition rate is 23.61 kHz with a variation of 1.84 kHz rms. The fitted half-width of the pulse duration is shown in (c) and has a mean value of 8.35 ns with a variation of 0.23 ns rms. The corresponding proportional pulse energy in (d) is obtained by integrating over the area of each pulse and then summing all areas. The total area of the pulse train corresponds to the total energy in the pulse train and, taking into account the repetition rate and the duty cycle, a total average power can thus be evaluated. If the average output power is now recorded with a power meter, the total pulse train energy and also the individual pulse energy can be compared and recalculated. Using the characterization setup shown in Figure 7.1, it is possible to simultaneously record the average output power and the pulse train over the period. The accuracy of the analysis method for determining the single pulse energy versus the mean output power can be validated for low repetition rates (<25 kHz) using an energy meter (Ophir PE9-C). Here, a maximum deviation of only around 1 % was found between the pulse energy calculated via the average power and the individual pulse energy measured at the energy meter, so that the post-processing analysis method is quite suitable in

stable laser operation. However, the prerequisite for this method is that the laser runs stably concerning the average output power and that the pulse patterns reproduce themselves.
The peak power can be calculated (Eq. 4.3) by using the back-calculated single pulse energy and taking into account the pulse duration, which is shown in (e).
With the help of this analysis method the time to reach steady-state operation as well as effects like longitudinal mode competition and satellite pulses (see 4.3.1) can be determined quite easily.

7.3 FIBER-COUPLED PUMP LASER CHARACTERIZATION

The fiber-coupled 808 nm pump laser (BWT K808DA5RN-35.00W) that was used for the laser experiments in Chapter 4 is characterized in the following. The pump current and resulting output power were controlled by a laser driver (Ostech ds11-la14v14), which is capable of pro-

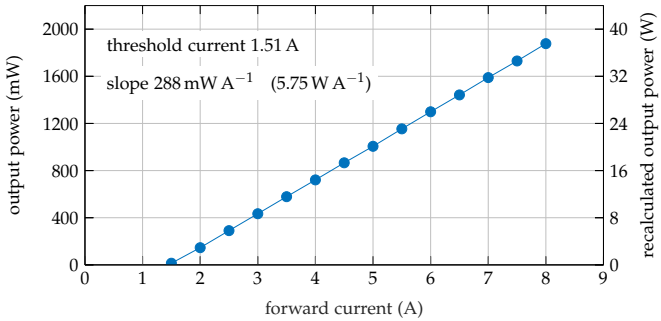

Figure 7.3: Output power of the 808 nm fiber-coupled pump laser concerning the applied forward current recorded at a duty cycle of 5 % (10 ms/200 ms). The right y-axis shows the recalculated equivalent CW output power.

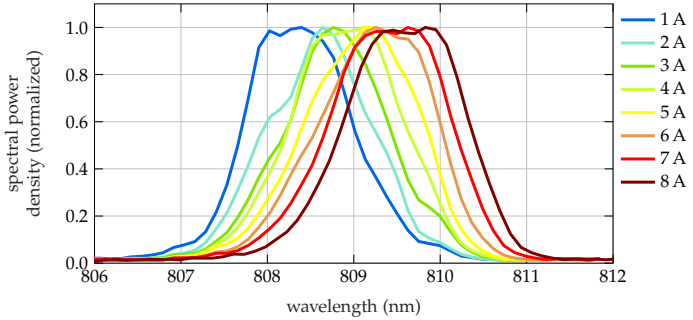

Figure 7.4: Emission spectrum of the 808 nm fiber-coupled pump laser as a function of the applied forward current between 1 A and 8 A.

viding a maximum output current of 14 A. The exact laser temperature and the resulting central wavelength were regulated by two Peltier elements (Laird PE-071-14-15) which were sandwiched between the laser housing and a water-cooled heat sink used for heat dissipation.

Figure 7.3 shows the investigation of the output power as a function of the applied forward current at a duty cycle of 5 % (10 ms/200 ms) and

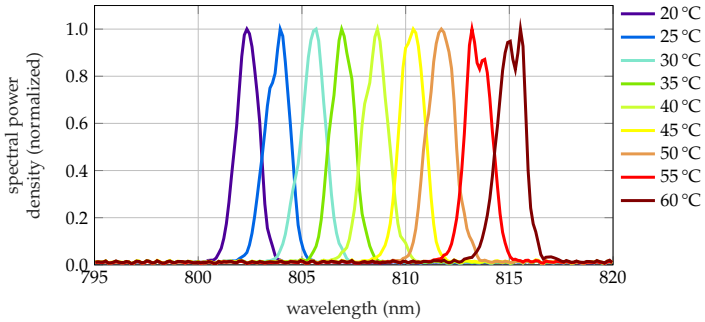

Figure 7.5: Emission spectrum of the 808 nm fiber-coupled pump laser for different temperatures between 20 °C and 60 °C at a constant applied forward current of 6 A.

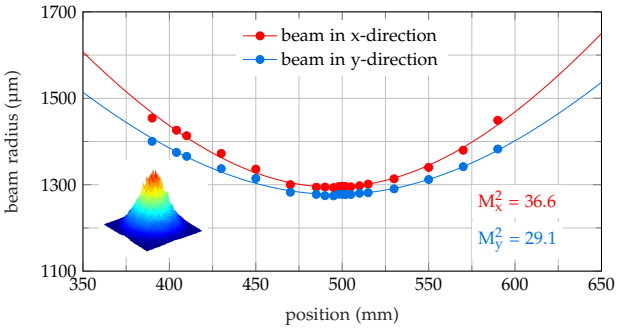

Figure 7.6: Beam caustics generated in the measuring device for determining the beam quality factor M^2. The inset shows the transverse beam profile recorded at a relative position of 450 mm.

a set temperature of 25 °C. The left axis shows the measured output power, whereas the right axis indicates the recalculated output power for continuous operation. Starting at a current threshold of 1.51 A, the output power increases linearly with a slope of 288 mW A^{-1}, corresponding to 5.75 W A^{-1} for the continuous operation. The maximum output power of 37.5 W per pulse results in a conversion efficiency of 46.9 % with a slope efficiency of 57.3 %. The spectral shift of the wavelength is shown as a function of the applied pump current in Fig. 7.4. The spectral width (FWHM) of the pump laser was about 1.4 nm. With increasing forward current, a spectral redshift of about 0.17 nm A^{-1} was measured. Similarly, Figure 7.5 shows the effect of temperature on the emission spectrum. Here, a shift of about 0.32 nm $°C^{-1}$ was observed for a temperature variation of the Peltier element between 20 °C and 60 °C.

For the investigation of the beam quality, the divergent pump beam was collimated using a spherical lens (f=100 mm) to ensure loss-free coupling into the M^2 measuring device. The beam caustic generated in the instrument at an applied forward current of 8 A is shown in Figure

7.6. The beam quality factor M^2 in x- and y-direction was 36.6 and 29.1, respectively. Measurement of the beam quality at lower output powers showed no significant changes compared to the measurement at maximum output power. The inset shows the recorded transverse beam profile at a relative position of 450 mm.

7.4 FREE-SPACE PUMP LASER CHARACTERIZATION

This section characterizes the 808 nm laser diode that was used in Chapter 5 to investigate the potential for lidar systems. Here, the module had a fiber core diameter of 105 µm and a numerical aperture of 0.22. The laser diode was controlled analogously to the fiber-coupled pump laser using a laser driver (Ostech ds11-la14v14) with a maximum output current of 14 A. For temperature control and tuning of the wavelength, the diode was mounted on a water-cooled aluminum holder. The custom-

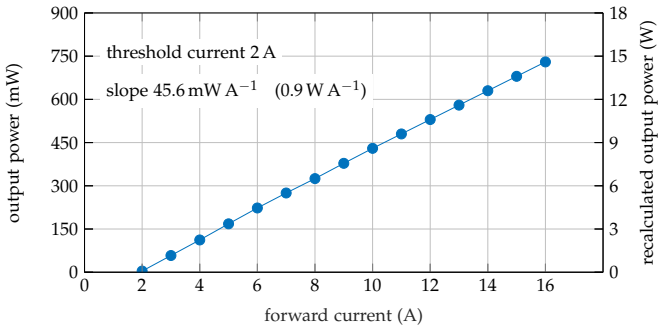

Figure 7.7: Output power of the 808 nm laser diode concerning the applied forward current recorded at a duty cycle of 5 % (10 ms/200 ms). The right y-axis shows the recalculated equivalent CW output power.

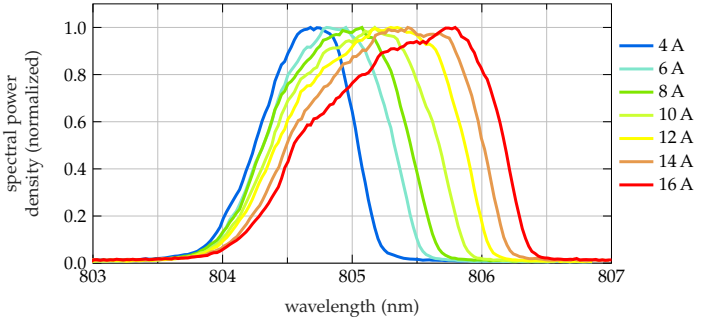

Figure 7.8: Emission spectrum of the 808 nm laser diode as a function of the applied forward current between 4 A and 16 A.

designed holder allowed the diode to be tilted both vertically and horizontally using a two-axis mount (Thorlabs KM100PM).

The output power as a function of the forward current is shown in Figure 7.7, using a duty cycle of 5 % (10 ms/200 ms) and a temperature of 40 °C. The recalculated output power for continuous operation is shown on the right axis. The output power increases linearly from a threshold current of 2 A with a slope of 52.1 mW A^{-1} to a maximum

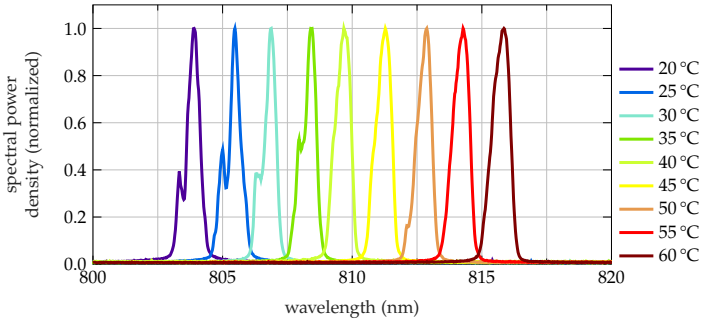

Figure 7.9: Emission spectrum of the 808 nm laser diode for various temperatures between 20 °C and 60 °C at a constant applied forward current of 6 A.

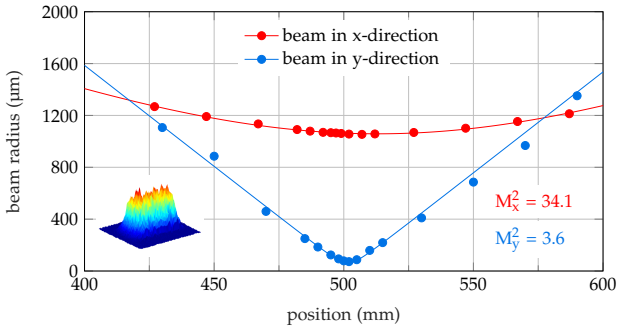

Figure 7.10: Beam caustics generated in the measuring device for determining the beam quality factor M^2. The inset shows the transverse beam profile recorded at a relative position of 550 mm.

output power of 730 mW. For continuous operation, this would correspond to an equivalent maximum output power of 14.6 W, while the slope is 0.9 W A^{-1}. At an operating voltage of 2 V, this equals a slope efficiency of 51.9 % and a maximum conversion efficiency of 45.6 %. The spectrum of the laser diode is shown for different forward currents in Fig. 7.8. The spectral width (FWHM) increased from about 0.77 nm at 4 A to about 1.44 nm at 16 A for increasing currents. In addition, it was observed that the center wavelength shifts by about 0.06 nm A^{-1}. Figure 7.9 shows the temperature-dependent wavelength shift for temperatures between 20 °C and 60 °C at a constant current of 6 A. With increasing temperature, the central wavelength shifts with 0.29 nm $°C^{-1}$ towards the infrared spectral region. To measure the beam quality factor M^2, it was necessary to collimate the fast axis using cylindrical lenses (f=50 mm) to permit truncation of the beam when it is coupled into the measuring device. The resulting beam caustic in the measuring device is shown in Figure 7.10 and results in a beam quality factor of 34.1 and 3.6 in x- and y-direction, respectively. The curve was recorded at a forward current of 6 A and a laser diode temperature of 40 °C, but no

significant deviations in beam quality were observed for other currents or temperatures.

ACRONYMS

AL aspheric lens

AR anti reflection

ASE amplified spontaneous emission

BPP beam parameter product

CW continuous wave

EMC electromagnetic compatibility

ESA excited-state absorption

FEA finite element analysis

FOM figure of merit

FOV field of view

FSR free spectral range

FWHM full width at half maximum

GSA ground-state absorption

HWP half-wave plate

MPE maximum permissible exposure

OC output coupler

OCM output coupler mirror

QC quasi-continuous

QCW quasi-continuous wave

SL spheric lens

SPD spectral power density

TOF time-of-flight

LIST OF PUBLICATIONS AND CONTRIBUTIONS

JOURNAL CONTRIBUTIONS

Marco Nägele, Klaus Stoppel, and Thomas Dekorsy, "Passively Q-switched 914 nm microchip laser for lidar systems," Opt. Express **29**, 23799-23809 (2021).

Marco Nägele, Sascha Kalusniak, Christian Kränkel, Klaus Stoppel, and Thomas Dekorsy, "Saturable absorbers for passive Q-switching between 900-920 nm," Opt. Mater. Express (in preperation).

CONFERENCE CONTRIBUTIONS

Marco Nägele, Klaus Stoppel, Heiko Ridderbusch, and Thomas Dekorsy "Passively Q-switched Nd:YVO_4 laser operating at 914 nm," SPIE Photonics West, 8946-12, San Francisco 2020, oral.

CONFERENCE PROCEEDINGS

Marco Nägele, Klaus Stoppel, Heiko Ridderbusch, and Thomas Dekorsy "Passively Q-switched Nd:YVO_4 laser operating at 914 nm," in Proceedings of Solid State Lasers XXIX: Technology and Devices. Vol. 11259. International Society for Optics and Photonics, 2020.

PREVIOUS PROJECTS

Marco Nägele, Tobias Steinle, Florian Mörz, Heiko Linnenbank, Andy Steinmann, and Harald Giessen, "Compact harmonic cavity optical parametric oscillator for optical parametric amplifier seeding," Opt. Express **28**, 25000-25006 (2020).

BIBLIOGRAPHY

[1] J. Bilbro, G. Fichtl, D. Fitzjarrald, M. Krause, and R. Lee, "Airborne Doppler Lidar Wind Field Measurements," Bulletin - American Meteorological Society **65**(4), 348–359 (1984).

[2] R. T. Menzies and R. Michael Hardesty, "Coherent Doppler Lidar for Measurements of Wind Fields," Proceedings of the IEEE **77**(3), 449–462 (1989).

[3] M. Wirth, A. Fix, P. Mahnke, H. Schwarzer, F. Schrandt, and G. Ehret, "The airborne multi-wavelength water vapor differential absorption lidar WALES: system design and performance," Applied Physics B: Lasers and Optics **96**(1), 201–213 (2009).

[4] K. Lim, P. Treitz, M. Wulder, B. St-Ongé, and M. Flood, "LiDAR remote sensing of forest structure," Progress in Physical Geography **27**(1), 88–106 (2003).

[5] J. A. Bellian, C. Kerans, and D. C. Jennette, "Digital outcrop models: Applications of terrestrial scanning lidar technology in stratigraphic modeling," Journal of Sedimentary Research **75**(2), 166–176 (2005).

[6] E. Barrett and O. Bend-Dov, "Applications of the Lidar to Air Pollution Measurements," Journal of Applied Meteorology **148**, 148–162 (1967).

[7] M. Beniston, J. P. Wolf, M. Beniston-Rebetez, H. J. Kolsch, P. Rairoux, and L. Woste, "Use of lidar measurements and nu-

merical models in air pollution research," Journal of Geophysical Research **95**(D7), 9879–9894 (1990).

[8] M. E. Warren, "Automotive LIDAR Technology," 2019 Symposium on VLSI Circuits **1**, 254–255 (2019).

[9] J. Hälker and H. Barth, "Lidar as a Key Technology for Automated and Autonomous Driving," ATZ worldwide **120**, 70–73 (2018).

[10] F. Villa, F. Severini, and F. Madonini, "SPADs and SiPMs Arrays for Long-Range High-Speed Light Detection and Ranging (LiDAR)," Sensors **21**(11), 3839 (2021).

[11] A. McCarthy, X. Ren, A. Della Frera, N. R. Gemmell, N. J. Krichel, C. Scarcella, A. Ruggeri, A. Tosi, and G. S. Buller, "Kilometer-range depth imaging at 1550 nm wavelength using an InGaAs/InP single-photon avalanche diode detector," Optics Express **21**(19), 22098 (2013).

[12] R. Lussana, F. Villa, A. D. Mora, D. Contini, A. Tosi, and F. Zappa, "Enhanced single-photon time-of-flight 3D ranging," Optics Express **23**(19), 24962 (2015).

[13] I. Takai, H. Matsubara, M. Soga, M. Ohta, M. Ogawa, and T. Yamashita, "Single-Photon avalanche diode with enhanced NIR-sensitivity for automotive LIDAR systems," Sensors **16**(4), 459 (2016).

[14] K. Morimoto, A. Ardelean, M.-L. Wu, A. C. Ulku, I. M. Antolovic, C. Bruschini, and E. Charbon, "Megapixel time-gated SPAD image sensor for 2D and 3D imaging applications," Optica **7**(4), 346 (2020).

[15] T. Okino, S. Yamada, Y. Sakata, S. Kasuga, M. Takemoto, Y. Nose, H. Koshida, M. Tamaru, Y. Sugiura, S. Saito, S. Koyama, M. Mori, Y. Hirose, M. Sawada, A. Odagawa, and T. Tanaka, "A 1200×900 6µm 450fps Geiger-Mode Vertical Avalanche Photodiodes CMOS Image Sensor for a 250m Time-of-Flight Ranging System Using Direct-Indirect-Mixed Frame Synthesis with Configurable-Depth-Resolution Down to 10cm," in *IEEE International Solid-State Circuits Conference-(ISSCC)*, pp. 96–98 (IEEE, 2020).

[16] D. Chitnis and S. Collins, "A SPAD-based photon detecting system for optical communications," Journal of Lightwave Technology **32**(10), 2028–2034 (2014).

[17] K. S. Roy Henderson, *Laser Safety* (CRC Press, 2003).

[18] M. Kutila, P. Pyykonen, H. Holzhuter, M. Colomb, and P. Duthon, "Automotive LiDAR performance verification in fog and rain," in *IEEE Conference on Intelligent Transportation Systems, Proceedings (ITSC)*, pp. 1695–1701 (2018).

[19] J. D. Spinhirne, "Micro Pulse Lidar," IEEE Transactions on Geoscience and Remote Sensing **31**(1), 48–55 (1993).

[20] T. Raj, F. H. Hashim, A. B. Huddin, M. F. Ibrahim, and A. Hussain, "A survey on LiDAR scanning mechanisms," Electronics **9**(5), 741 (2020).

[21] A. Kausas and T. Taira, "Giant-pulse Nd:YVO_4 microchip laser with MW-level peak power by emission cross-sectional control," Optics Express **24**(4), 3137 (2016).

[22] A. Maleki, M. H. Moghtader dindarlu, H. Saghafifar, M. Kavosh Tehrani, M. Soltanolkotabi, M. Dehghan Baghi, and M. R. Maleki Ardestani, "57 mJ with 10 ns passively Q-switched diode pumped

Nd:YAG laser using Cr^{4+}:YAG crystal," Optical and Quantum Electronics **48**(1), 1–12 (2016).

[23] G. J. Spühler, R. Paschotta, M. P. Kullberg, M. Graf, M. Moser, E. Mix, G. Huber, C. Harder, and U. Keller, "A passively Q-switched Yb:YAG microchip laser," Applied Physics B: Lasers and Optics **72**(3), 285–287 (2001).

[24] A. C. Butler, D. J. Spence, and D. W. Coutts, "Scaling Q-switched microchip lasers for shortest pulses," Applied Physics B: Lasers and Optics **109**(1), 81–88 (2012).

[25] Y. Sato and T. Taira, "Temperature dependencies of stimulated emission cross section for Nd-doped solid-state laser materials," Optical Materials Express **2**(8), 1076 (2012).

[26] D. K. Serkland, G. A. Keeler, K. M. Geib, and G. M. Peake, "Narrow linewidth VCSELs for high-resolution spectroscopy," Vertical-Cavity Surface-Emitting Lasers XIII **7229**(505), 722907 (2009).

[27] E. Haglund, Å. Haglund, J. S. Gustavsson, B. Kögel, P. Westbergh, and A. Larsson, "Reducing the spectral width of high speed oxide confined VCSELs using an integrated mode filter," Vertical-Cavity Surface-Emitting Lasers XVI **8276**(0), 82760L (2012).

[28] R. Michalzik, *VCSELs* (Springer, 2013).

[29] W. J. Fleming, "Overview of Automotive Sensors," IEEE Sensors Journal **1**(4), 296–308 (2001).

[30] T. J. Kane, "1.34 µm Nd:YVO_4 laser passively Q-switched by V:YAG and optimized for LiDAR," in *Proceedings of the SPIE*, February 2020, p. 1125902 (2020).

[31] R. Zhou, T. Zhang, E. Li, X. Ding, Z. Cai, B. Zhang, W. Wen, P. Wang, and J. Yao, "8.3 W diode-end-pumped continuous-wave

Nd:YAG laser operating at 946-nm," Optics Express **13**(25), 10115–10119 (2005).

[32] P. Jiang, "Efficient 914-nm Nd:YVO_4 laser under double-end polarized pumping," Applied Optics **55**(5), 1072–1075 (2016).

[33] J. Gao, X. Yu, F. Chen, X. Li, R. Yan, K. Zhang, J. Yu, and Y. Wang, "12.0-W continuous-wave diode-end-pumped Nd:$GdVO_4$ laser with high brightness operating at 912-nm," Optics Express **17**(5), 3574 (2009).

[34] F. Chen, J. Sun, R. Yan, and X. Yu, "Reabsorption cross section of Nd^{3+} -doped quasi-three-level lasers," Scientific Reports **9**(1), 1–8 (2019).

[35] H. B. Seyed Pourmand, Noriah Bidin, "Temperature and input energy dependence of the 946-nm stimulated emission cross section of Nd^{3+}:YAG pumped by a flashlamp," Chinese Physics Letters **29**(3), 034206 (2012).

[36] J. Eichler, "Thermal lensing and depolarization in a highly pumped Nd:YAG laser amplifier," Journal of Physics D: Applied Physics **26**(11), 1884 (1993).

[37] U. Kindereit, A. J. Weger, F. Stellari, P. Song, H. Deslandes, T. Lundquist, and P. Sabbineni, "Near-infrared photon emission spectroscopy of a 45 nm SOI ring oscillator," IEEE International Reliability Physics Symposium Proceedings pp. 1–7 (2012).

[38] E. Herault, F. Balembois, and P. Georges, "Nd:$GdVO_4$ as a three level laser at 879 nm," Optics Letters **31**(18), 2731–2733 (2006).

[39] W. Gong, Y. Qi, and Y. Bi, "A comparative study on continuous laser operation on the $^4F_{3/2}$- $^4I_{9/2}$ transitions of Nd:$GdVO_4$ and Nd:YVO_4 crytals," Optics Communications **282**(5), 955–957 (2009).

[40] J. Gao, X. Yu, B. Wei, and X. D. Wu, "Quasi-three-level Nd:YVO_4 laser operation at 914 nm under 879 nm diode laser pumping," Laser Physics **20**(7), 1590–1593 (2010).

[41] F. Chen, X. Yu, C. Wang, R. P. Yan, X. D. Li, J. Gao, Z. H. Zhang, and J. H. Yu, "Diode-pumped short pulse passively Q-switched 912 nm Nd:$GdVO_4$/Cr:YAG laser at high repetition rate operation," Laser Physics **20**(6), 1275–1278 (2010).

[42] X. Yu, R. Yan, X. Li, Y. Ma, D. Chen, and Y. Junhua, "High power 2 MHz passively Q-switched nanosecond Nd:YVO_4/Cr^{4+}:YAG 914 nm laser," Applied Optics **51**(14), 2728–2732 (2012).

[43] M. Nägele, K. Stoppel, H. Ridderbusch, and T. Dekorsy, "Passively Q-switched Nd:YVO_4 laser operating at 914 nm," in *Proceedings of the SPIE*, February, p. 112590P (2020).

[44] W. Koechner, *Solid-State Laser Engineering* (Springer, 2006).

[45] A. Siegman, *Lasers* (University Science Books, 1986).

[46] J. Eichler, *Laser* (Springer, 2018).

[47] R. Paschotta, *Encyclopedia of laser physics and technology* (Wiley-VCH, 2008).

[48] R. Moncorgé, "Laser materials based on transition metal ions," Optical Materials **63**, 105–117 (2017).

[49] Y. Kalisky, *Solid State Lasers - Tunable Sources and Passive Q-switchting* (SPIE Press, 2014).

[50] M. Inguscio and R. Wallenstein, *Solid State Lasers* (Springer, 1993).

[51] W. Koechner, "Thermal Lensing in a Nd:YAG Laser Rod," Applied Optics **9**(11), 2548 (1970).

[52] X. Peng, A. Asundi, Y. Chen, and Z. Xiong, "Heating measurements in diode-end-pumped $NdYVO_4$ lasers," Optical Engineering **40**(6), 1100–1105 (2001).

[53] S. Li, Y. Li, S. Zhao, G. Li, X. Wang, K. Yang, D. Li, and T. Li, "Thermal effect investigation and passively Q-switched laser performance of composite Nd:YVO_4 crystals," Optics and Laser Technology **68**, 146–150 (2015).

[54] D. Jin, Z. Bai, Q. Wang, Y. Chen, Z. Liu, R. Fan, Y. Qi, J. Ding, X. Yang, Y. Wang, and Z. Lu, "Doubly Q-switched single longitudinal mode Nd:YAG laser with electro-optical modulator and Cr:YAG," Optics Communications **463**, 125500 (2020).

[55] V. V. Antsiferov and G. I. Smirnov, *Physics of Solid-State Lasers* (Cambridge International Science Publishing Ltd., 2005).

[56] A. Sennaroglu, *Solid -State Lasers and Applications* (CRC Press, 2007).

[57] J. J. Degnan, "Theory of the optimally coupled Q-Switched laser," IEEE Journal of Quantum Electronics **25**(2), 214–220 (1989).

[58] J. Liu, B. Ozygus, S. Yang, U. Seelig, A. Ding, H. Weber, X. Xu, and Z. Shao, "Efficient passive Q-switching operation of a diode-pumped Nd:$GdVO_4$ laser with a Cr^{4+}:YAG saturable absorber," Journal of the Optical Society of America B **20**(4), 652 (2003).

[59] J. J. Degnan, D. B. Coyle, and R. B. Kay, "Effects of thermalization on Q-switched laser properties," IEEE Journal of Quantum Electronics **34**(5), 887–899 (1998).

[60] S. P. Ng, D. Y. Tang, L. Qian, and L. J. Qin, "Satellite pulse generation in diode-pumped passively Q-switched Nd:$GdVO_4$ lasers," IEEE Journal of Quantum Electronics **42**(7), 625–632 (2006).

[61] R. Paschotta, *Field Guide to Laser Pulse Generation*, 8 (SPIE Press Book, 2008).

[62] J. B. Khurgin, F. Jin, G. Solyar, C.-C. Wang, and S. Trivedi, "Cost-effective low timing jitter passively Q-switched diode-pumped solid-state laser with composite pumping pulses," Applied Optics **41**(6), 1095 (2002).

[63] A. Steinmetz, D. Nodop, J. Limpert, and A. Tünnermann, "Reduction of timing-jitter in a passively Q-switched microchip laser using self-injection seeding," Optics InfoBase Conference Papers **35**(17), 2885–2887 (2010).

[64] B. Cole, L. Goldberg, C. W. Trussell, A. Hays, B. W. Schilling, and C. McIntosh, "Reduction of timing jitter in a Q-Switched Nd:YAG laser by direct bleaching of a Cr^{4+}:YAG saturable absorber," Optics Express **17**(3), 1766 (2009).

[65] Z. Burshtein, P. Blau, Y. Kalisky, Y. Shimony, and M. R. Kokta, "Excited-State Absorption Studies of Cr^{4+} Ions in Several Garnet Host Crystals," IEEE Journal of Quantum Electronics **34**(2), 292–299 (1998).

[66] R. Grange, M. Haiml, R. Paschotta, G. J. Spühler, L. Krainer, M. Golling, O. Ostinelli, and U. Keller, "New regime of inverse saturable absorption for self-stabilizing passively mode-locked lasers," Applied Physics B: Lasers and Optics **80**(2), 151–158 (2005).

[67] G. Xiao and M. Bass, "A Generalized Model for Passively Q-Switched Lasers Including Excited State Absorption in the Saturable Absorber," IEEE Journal of Quantum Electronics **33**(1), 41–44 (1997).

[68] A. Szabo and R. A. Stein, "Theory of Laser Giant Pulsing by a Saturable Absorber," Journal of Applied Physics **36**(5), 1562–1566 (1965).

[69] X. Zhang, S. Zhao, Q. Wang, Q. Zhang, L. Sun, and S. Zhang, "Optimization of Cr^{4+} -Doped Saturable-Absorber -Switched Lasers," Quantum **33**(12), 2286–2294 (1997).

[70] H. Sakai, H. Kan, and T. Taira, ">1 MW peak power single-mode high-brightness passively Q-switched Nd^{3+}:YAG microchip laser," Optics Express **16**(24), 19891–19899 (2008).

[71] J. Dong, A. Shirakawa, and K. I. Ueda, "Numerical simulation of a diode-laser-pumped self-Q-switched Cr,Yb:YAG microchip laser," Optical Review **12**(3), 170–178 (2005).

[72] J. H. Mathews and Kurtis D. Fink, *Numerical methods using MATLAB* (Prentice-Hall Pub. Inc., 2004).

[73] N. Pavel, S. Jiro, K. Sunao, and T. Taira, "High Average Power Diode End-Pumped Composite Nd:YAG Laser Passively Q-switched by Cr^{4+}:YAG Saturable Absorber," Japanese Journal of Applied Physics **1253**(3R), 1253–1259 (2001).

[74] G. H. C. New and T. B. O'Hare, "A simple criterion for passive Q-switching of lasers," Physics Letters A **68**(1), 27–28 (1978).

[75] Y. F. Chen, Y. P. Lan, and H. L. Chang, "Analytical model for design criteria of passively Q-switched lasers," IEEE Journal of Quantum Electronics **37**(3), 462–468 (2001).

[76] G. H. C. New and T. B. O'Hare, "A simple criterion for passive Q-switching of lasers," Physics Letters A **68**(1), 27–28 (1978).

[77] M. C. Marconi, O. E. Martinez, and F. P. Diodati, "Second threshold condition in the case of Q switching by self-focusing," Journal of the Optical Society of America B **3**(12), 1630 (1986).

[78] Y. Bai, D. Shen, C. Li, J. Song, and K. I. Ueda, "Passively Q-switched Nd:S-VAP laser with a Cr^{4+}:YAG crystal saturable absorber," Journal of the Communications Research Laboratory **46**(3), 377–378 (1997).

[79] X. Zhang, A. Brenier, J. Wang, and H. Zhang, "Absorption cross-sections of Cr^{4+}:YAG at 946 and 914 nm," Optical Materials **26**(3), 293–296 (2004).

[80] A. W. Tucker, M. Birnbaum, C. L. Fincher, and J. W. Erler, "Stimulated-emission cross section at 1064 and 1342 nm in Nd:YVO_4," Journal of Applied Physics **48**(12), 4907–4911 (1977).

[81] H. Kogelnik and T. Li, "Laser Beams and Resonators," Proceedings of the IEEE **54**(10), 1312–1329 (1966).

[82] N. Hodgson and H. Weber, *Laser Resonators and Beam Propagation* (Springer, 2004).

[83] D. Metcalf, P. de Giovanni, J. Zachorowski, and M. Leduc, "Laser resonators containing self-focusing elements," Applied Optics **26**(21), 4508 (1987).

[84] V. Magni, "Resonators for solid-state lasers with large-volume fundamental mode and high alignment stability," Applied Optics **25**(1), 107 (1986).

[85] H. Kogelnik, "Imaging of Optical Modes — Resonators with Internal Lenses," Bell System Technical Journal **44**(3), 455–494 (1965).

[86] C. M. Stickley and L. G. Hanscom, "Laser Brightness Gain and Mode Control by Compensation for Thermal Distortion," IEEE Journal of Quantum Electronics **2**(4), 134 (1966).

[87] H. P. Kortz, R. Iffländer, and H. Weber, "Stability and beam divergence of multimode lasers with internal variable lenses," Applied Optics **20**(23), 4124 (1981).

[88] H. Weber, R. Ifflander, and P. Seiler, "High Power Nd-Lasers for Industrial Applications," High Power Lasers and Their Industrial Applications **0650**(October 1986), 92 (1986).

[89] H.-S. Shi, G. Zhang, and H.-Y. Shen, "Measurement of principal refractive indices and the thermal refractive index coefficients of yttrium vanadate," Journal of Synthetic Crystals **30**(1), 85–88 (2001).

[90] A. K. Cousins, "Temperature and Thermal Stress Scaling in Finite-Length End-Pumped Lasers Rods," IEEE Journal of Quantum Electronics **28**(4), 1057–1069 (1992).

[91] C. Pfistner, R. Weber, H. P. Weber, S. Merazzi, and R. Gruber, "Thermal Beam Distortions In End-Pumped Nd: YAG, Nd:GSGG, and Nd:YLF Rods," IEEE Journal of Quantum Electronics **30**(7), 1605–1615 (1994).

[92] L. Yan and C. H. Lee, "Thermal effects in end-pumped Nd:phosphate glasses," Journal of Applied Physics **75**(3), 1286–1292 (1994).

[93] S. Chénais, S. Forget, F. Druon, F. Balembois, and P. Georges, "Direct and absolute temperature mapping and heat transfer measurements in diode-end-pumped Yb:YAG," Applied Physics B: Lasers and Optics **79**(2), 221–224 (2004).

[94] H. Zhang, Y. Wen, L. Zhang, Z. Fan, J. Liu, and C. Wu, "Influences of Pump Spot Radius and Depth of Focus on the Thermal Effect of Tm:YAP crystal," Current Optics and Photonics **3**(5), 458–465 (2019).

[95] S. B. Sutton and G. F. Albrecht, "Optical distortion in end-pumped solid-state rod lasers," Applied Optics **32**(27), 5256 (1993).

[96] U. O. Farrukh, A. M. Buoncristiani, and C. E. Byvik, "An Analysis of the Temperature Distribution in Finite Solid-State Laser Rods," IEEE Journal of Quantum Electronics **24**(11), 2253–2263 (1988).

[97] S. C. Tidwell, J. F. Seamans, M. S. Bowers, and A. K. Cousins, "Scaling CW Diode-End-Pumped Nd:YAG Lasers to High Average Powers," IEEE Journal of Quantum Electronics **28**(4), 997–1009 (1992).

[98] J. Frauchiger, P. Albers, and H. P. Weber, "Modeling of Thermal Lensing and Higher Order Ring Mode Oscillation in End-Pumped CW Nd:YAG Lasers," IEEE Journal of Quantum Electronics **28**(4), 1046–1056 (1992).

[99] M. E. Innocenzi, H. T. Yura, C. L. Fincher, and R. A. Fields, "Thermal modeling of continuous-wave end-pumped solid-state lasers," Applied Physics Letters **56**(19), 1831–1833 (1990).

[100] Z. Xiong, Z. G. Li, N. Moore, W. L. Huang, and G. C. Lim, "Detailed investigation of thermal effects in longitudinally diode-pumped Nd:YVO_4 lasers," IEEE Journal of Quantum Electronics **39**(8), 979–986 (2003).

[101] Z. Zhuo, T. Li, X. Li, and H. Yang, "Investigation of Nd:YVO_4/YVO_4 composite crystal and its laser performance

pumped by a fiber coupled diode laser," Optics Communications **274**(1), 176–181 (2007).

[102] E. H. Bernhardi, A. Forbes, C. Bollig, and M. J. D. Esser, "Estimation of thermal fracture limits in quasi-continuous-wave end-pumped lasers through a time-dependent analytical model," Optics Express **16**(15), 11115 (2008).

[103] S. Cante, S. J. Beecher, and J. I. Mackenzie, "Characterising energy transfer upconversion in Nd-doped vanadates at elevated temperatures," Optics Express **26**(6), 6478–6489 (2018).

[104] X. Délen, F. Balembois, and P. Georges, "High gain single stage and single pass Nd:YVO_4 passive amplifier for picosecond pulses," Advanced Solid-State Photonics, ASSP 2012 **29**(9), 2339–2346 (2012).

[105] P. Zhu, D. Li, P. Hu, A. Peixin, P. Shi, C. Haas, N. Wu, and K. Du, "High efficiency 165 W near-diffraction-limited Nd:YVO_4 slab oscillator pumped at 880 nm," Optics Letters **33**(17) (2008).

[106] W. Han, X. Chen, L. Xia, S. Wang, H. Zhang, and J. Liu, "Continuous-wave and passive Q-switching laser performance of Yb:YSGG crystal," Optics Express **22**(25), 31404 (2014).

[107] L. Goldberg, B. Cole, C. McIntosh, V. King, A. D. Hays, and S. R. Chinn, "Narrow-band 1 W source at 257 nm using frequency quadrupled passively Q-switched Yb:YAG laser," Optics Express **24**(15), 17397 (2016).

[108] M. Zhao, C. Wang, Q. Hao, Z. Zou, J. Liu, X. Fan, and L. Su, "High single-pulse energy passively Q-switched laser based on Yb,Gd:SrF_2 crystal," Chinese Optics Letters **18**(10), 101401 (2020).

[109] T. Kondo, D. Schlenker, T. Miyamoto, Z. Chen, M. Kawaguchi, E. Gouardes, F. Koyama, and K. Iga, "Lasing Characteristics of 1.2 μm Highly Strained GaInAs/GaAsQuantum Well Lasers," Japanese Journal of Applied Physics, Part 1: Regular Papers and Short Notes and Review Papers **40**(2 A), 467–471 (2001).

[110] L. W. Sung and H. H. Lin, "Highly strained 1.24-μm InGaAs/-GaAs quantum-well lasers," Applied Physics Letters **83**(6), 1107–1109 (2003).

[111] Y. P. Huang, H. C. Liang, J. Y. Huang, K. W. Su, A. Li, Y. F. Chen, and K. F. Huang, "Semiconductor quantum-well saturable absorbers for efficient passive Q switching of a diode-pumped 946 nm Nd:YAG laser," Applied Optics **46**(25), 6273–6276 (2007).

[112] G. M. Thomas and M. J. Damzen, "Passively Q-switched Nd:YVO_4 laser with greater than 11W average power," Optics Express **19**(5), 4577 (2011).

[113] Y. Cheng, J. Dong, and Y. Ren, "Enhanced performance of Cr,Yb:YAG microchip laser by bonding Yb:YAG crystal," Optics Express **20**(22), 24803 (2012).

[114] J. Dong, A. Shirakawa, and K. Ueda, "Switchable pulses generation in passively Q-switched multilongitudinal-mode microchip laser," Laser Physics Letters **4**(2), 109–116 (2007).

[115] J. Dong, A. Shirakawa, and K. I. Ueda, "Sub-nanosecond passively Q-switched Yb:YAG/Cr^{4+}:YAG sandwiched microchip laser," Applied Physics B: Lasers and Optics **85**(4), 513–518 (2006).

[116] J. Dong, K.-i. Ueda, A. Shirakawa, H. Yagi, T. Yanagitani, and A. A. Kaminskii, "Composite Yb:YAG/Cr^{4+}:YAG ceramics picosecond microchip lasers," Optics Express **15**(22), 14516 (2007).

[117] B. Xu, P. Camy, J.-L. Doualan, A. Braud, Z. Cai, F. Balembois, and R. Moncorgé, "Frequency doubling and sum-frequency mixing operation at 4692, 471, and 473 nm in Nd:YAG," Journal of the Optical Society of America B **29**(3), 346 (2012).

[118] W. R. Sooy, "The natural selection of modes in a passive Q-switched laser," Applied Physics Letters **7**(2), 36–37 (1965).

[119] Y. Wang, W. Yang, H. Zhou, M. Huo, and Y. Zhen, "Temperature dependence of the fractional thermal load of Nd:YVO_4 at 1064 nm lasing and its influence on laser performance," Optics Express **21**(15), 18068 (2013).

[120] B. Braun, F. X. Kärtner, G. Zhang, M. Moser, and U. Keller, "56-ps passively Q-switched diode-pumped microchip laser," Optics Letters **22**(6), 381 (1997).

[121] Y. G. Wang, X. Y. Ma, J. Y. Peng, H. M. Tan, and L. S. Qian, "High-repetition rate Q-switched Nd:YVO_4 laser with a composite semiconductor absorber," Applied Optics **45**(25), 6616–6619 (2006).

[122] E. Mehner, A. Steinmann, R. Hegenbarth, B. Braun, and H. Giessen, "Stable MHz-Repetition-Rate Passively Q-Switched Microchip Laser Frequency Doubled by MgO:PPLN," Advanced Solid-State Photonics, ASSP 2012 pp. 12–14 (2012).

[123] J. Dong, K. I. Ueda, H. Yagi, and A. A. Kaminskii, "Laser-diode pumped self-Q-switched microchip lasers," Optical Review **15**(2), 57–74 (2008).

[124] J. J. Zayhowski and C. Dill, "Diode-pumped passively Q-switched picosecond microchip lasers," Optics Letters **19**(18), 1427 (1994).

[125] D. Y. Tang, S. P. Ng, L. J. Qin, and X. L. Meng, "Deterministic chaos in a diode-pumped Nd:YAG laser passively Q-switched by a Cr^{4+}:YAG crystal," Optics Letters **28**(5), 325 (2003).

[126] M.-D. Wei, C.-H. Chen, and K.-C. Tu, "Spatial and temporal instabilities in a passively Q-switched Nd:YAG laser with a Cr^{4+}:YAG saturable absorber," Optics Express **12**(17), 3972 (2004).

[127] J. Dong, A. Shirakawa, and K. I. Ueda, "Antiphase dynamics of sub-nanosecond microchip Cr,Yb:YAG self-Q-switched multimode laser," European Physical Journal D **39**(1), 101–106 (2006).

[128] S. P. Ng and D. Y. Tang, "Period-doubling route to chaos in diode-pumped passively Q-switched Nd: $GdVO_4$ and Nd:YVO_4 lasers," International Journal of Bifurcation and Chaos **16**(9), 2689–2696 (2006).

[129] M. D. Wei, C. C. Cheng, and S. S. Wu, "Instability and satellite pulse of passively Q-switching Nd:$LuVO_4$ laser with Cr^{4+}:YAG saturable absorber," Optics Communications **281**(13), 3527–3531 (2008).

[130] R. Sutherland, *Handbook of nonlinear optics* (CRC Press, 2003).

[131] V. G. Niziev and A. V. Nesterov, "Influence of beam polarization on laser cutting efficiency," Journal of Physics D: Applied Physics **32**(13), 1455–1461 (1999).

[132] T. W. H. Hill, N. Carlson and T. W. H. R. E. Teets, F. V. Kowalski, W. T. Hill, N. Carlson, "Laser Polarization Spectroscopy," in *Advances in Laser Spectroscopy I*, vol. 113 (1977).

[133] H. Liu, O. Hornia, Y. C. Chen, and S.-h. Zhou, "Single-Frequency -Switched Cr – Nd:YAG Laser Operating at 946-nm Wavelength," IEEE Journal of Selected Topics in Quantum Electronics **3**(1), 26–28 (1997).

[134] A. Di Lieto, P. Minguzzi, A. Pirastu, S. Sanguinetti, and V. Magni, "A 7-W diode-pumped Nd: YVO_4 CW laser at 1.34 µm," Applied Physics B **75**(4) (2002).

[135] H. F. Lin, W. Z. Zhu, F. B. Xiong, and H. X. Shen, "An efficient and high polarized single cavity Nd:YVO_4 microchip laser," Applied Physics B: Lasers and Optics **111**(3), 453–456 (2013).

[136] Y. Xing-Peng, L. Qiang, C. Hai-Long, F. Xing, G. Ma-Li, and W. Dong-Sheng, "A novel orthogonally linearly polarized Nd: YVO_4 laser," Chinese Physics B **19**(8) (2010).

[137] C. Jung, B.-A. Yu, I.-S. Kim, Y. L. Lee, N. E. Yu, and D.-K. Ko, "A linearly-polarized Nd:YVO_4/KTP microchip green laser," Optics Express **17**(22), 19611 (2009).

[138] X. P. Yan, Q. Liu, H. L. Chen, X. Fu, M. L. Gong, and D. S. Wang, "A novel orthogonally linearly polarized Nd:YVO_4 laser," Chinese Physics B **19**(8) (2010).

[139] Y. F. Chen, T. M. Huang, C. L. Wang, and L. J. Lee, "Compact and efficient 3.2-W diode-pumped Nd: YVO_4/KTP green laser," Applied Optics **37**(24), 5727–5730 (1998).

[140] H. S. He, M. M. Zhang, J. Dong, and K. I. Ueda, "Linearly polarized pumped passively Q-switched Nd:YVO_4 microchip laser for Ince-Gaussian laser modes with controllable orientations," Journal of Optics (United Kingdom) **18**(12) (2016).

[141] J. J. Degnan, "Optimization of Passively Q-Switched Lasers," IEEE Journal of Quantum Electronics **31**(11), 1890–1901 (1995).

[142] F. D. Patel and R. J. Beach, "New formalism for the analysis of passively Q-switched laser systems," IEEE Journal of Quantum Electronics **37**(5), 707–715 (2001).

[143] J. Kim, S. Moon, Y. Park, and H. S. Kim, "Optimization of a passively Q-switched Yb:YAG laser Ignitor pumped by a laser diode with low power and long pulse width," Current Optics and Photonics **4**(2), 127–133 (2020).

[144] M. Badtke, H. Tanaka, L. J. Ollenburg, S. Kalusniak, and C. Kränkel, "Passively Q-switched 8.5-ns Pr^{3+}:YLF laser at 640 nm," Applied Physics B: Lasers and Optics **127**(6), 1–6 (2021).

[145] X. Peng, L. Xu, and A. Asundi, "High-power efficient continuous-wave TEM_{00} intracavity frequency-doubled diode-pumped Nd:YLF laser," Applied Optics **44**(5), 800–807 (2005).

[146] T. Dietrich, S. Piehler, M. Rumpel, P. Villeval, D. Lupinski, M. Abdou-Ahmed, and T. Graf, "Highly-efficient continuous-wave intra-cavity frequency-doubled Yb:LuAG thin-disk laser with 1 kW of output power," Optics Express **25**(5), 4917 (2017).

[147] N. D. Zameroski, M. Wanke, and D. Bossert, "Cavity length dependence of mode beating in passively Q-switched Nd-solid state lasers," Solid State Lasers XXII: Technology and Devices **8599**(March 2013), 85991V (2013).

[148] X. Zhang, S. Zhao, Q. Wang, Q. Zhang, L. Sun, and S. Zhang, "Optimization of Cr^{4+}-doped saturable-absorber Q-switched lasers," IEEE Journal of Quantum Electronics **33**(12), 2286–2294 (1997).

[149] E. Castellano-Hernández, S. Kalusniak, P. W. Metz, and C. Kränkel, "Diode-Pumped Laser Operation of Tb^{3+}:$LiLuF_4$ in the Green and Yellow Spectral Range," Laser and Photonics Reviews **14**(2), 1–7 (2020).

[150] J. Brooks, G. M. Bonner, A. J. Kemp, and D. J. M. Stothard, "Stability of Q-switched 2 µm lasers," OSA Continuum **3**(3), 568–579 (2020).

[151] Q. Berthomé, A. Grisard, B. Faure, G. Souhaité, E. Lallier, J. M. Melkonian, and A. Godard, "Actively Q-switched tunable single-longitudinal-mode 2 µm Tm:YAP laser using a transversally

chirped volume Bragg grating," Optics Express **28**(4), 5013–5021 (2020).

[152] L. Wang, Y. Qing, G. Mingwei, G. Chunqing, and W. Sijia, "Stable high-power Er:YAG ceramic single- frequency laser at 1645 nm," Optics Express **24**(13), 14966–14973 (2016).

[153] Y. J. Huang, Y. P. Huang, P. Y. Chiang, H. C. Liang, K. W. Su, and Y. F. Chen, "High-power passively Q-switched Nd:YVO_4 UV laser at 355 nm," Applied Physics B: Lasers and Optics **106**(4), 893–898 (2012).

[154] P. Li, H. Zhang, X. Chen, and Q. Wang, "Diode-pumped Nd:YAG ceramic laser at 946 nm passively Q-switched with a Cr^{4+}:YAG saturable absorber," Optics and Laser Technology **44**(3), 578–581 (2012).

[155] Y. Chen, Y. Lin, J. Huang, X. Gong, Z. Luo, and Y. Huang, "Single-longitudinal-mode 1521 nm passively q-switched Er:Yb:$YAl_3(BO_3)_4$ pulse microchip laser," Optics Express **27**(18), 26080 (2019).

[156] T. Y. Fan and R. L. Byer, "Modeling and CW Operation of a Quasi-Three-Level 946 nm Nd:YAG Laser," IEEE Journal of Quantum Electronics **23**(5), 605–612 (1987).

[157] C. Li, "Theoretical and Experimental Investigations of Diode-Pumped Tm:YAG Laser in Active Mirror," Optical Review **6**(5), 439–442 (1999).

[158] M. Nie, Q. Liu, E. Ji, and M. Gong, "End-pumped temperature-dependent passively Q-switched lasers," Applied Optics **54**(28), 8383 (2015).

[159] M. Bass, "The temperature dependence of Nd^{3+} doped solid-state lasers," IEEE Journal of Quantum Electronics **39**(6), 741–748 (2003).

[160] J. Xue, J. Shi, W. Chen, Y. Pan, and B. Su, "Temperature dependence of a Cr^{4+}:YAG passively Q-switched single-longitudinal-mode Nd:YVO_4 ring cavity laser," Optik **130**, 769–776 (2017).

[161] A. Kausas and T. Taira, "Giant-pulse Nd:YVO_4 microchip laser with MW-level peak power by emission cross-sectional control," Optics Express **24**(4), 3137 (2016).

[162] S. Xing and J. Bergquist, "Thermal Shifts of the Spectral Lines in the $^4F_{3/2}$ to $^4I_{11/2}$ Manifold of an Nd:YAG Laser," IEEE Journal of Quantum Electronics **24**(9) (1988).

[163] T. Saiki, K. Funahashi, S. Motokoshi, K. Imasaki, K. Fujioka, H. Fujita, M. Nakatsuka, and C. Yamanaka, "Temperature characteristics of small signal gain for Nd^{3+}/Cr^{4+}:YAG ceramic lasers," Optics Communications **282**(4), 614–616 (2009).

[164] O. Kimmelma, I. Tittonen, and S. C. Buchter, "Thermal tuning of laser pulse parameters in passively Q-switched Nd:YAG lasers," Applied Optics **47**(23), 4262–4266 (2008).

[165] X. Délen, F. Balembois, and P. Georges, "Temperature dependence of the emission cross section of Nd:YVO_4 around 1064 nm and consequences on laser operation," Journal of the Optical Society of America B **28**(5), 972–976 (2011).

[166] D. K. Sardar and R. M. Yow, "Stark components of $^4F_{3/2}$, $^4I_{9/2}$ and $^4I_{11/2}$ manifold energy levels and effects of temperature on the laser transition of Nd3+ in YVO_4," Optical Materials **14**, 5–11 (2000).

[167] Q. Mingxin, D. J. Booth, G. W. Baxter, and G. C. Bowkett, "Performance of a Nd:YVO_4 microchip laser with continuous-wave pumping at wavelengths between 741 and 825 nm," Applied Optics **32**(12), 2085 (1993).

[168] P. K. Mukhopadhyay, K. Ranganathan, J. George, S. K. Sharma, and T. P. Nathan, "Effect of Nd^{3+} concentration on CW and pulsed performance of fiber-coupled diode laser pumped Nd:YVO_4 laser at 1064 nm," Pramana - Journal of Physics **59**(1), 75–89 (2002).

[169] N. Mermilliod, R. Romero, I. Chartier, C. Garapon, and R. Moncorge, "Performance of Various Diode-Pumped Nd: Laser Materials: Influence of Inhomogeneous Broadening," IEEE Journal of Quantum Electronics **28**(4), 1179–1187 (1992).

[170] D. E. Zelmon, D. L. Small, and R. Page, "Refractive-index measurements of undoped yttrium aluminum garnet from 0.4 to 5.0 μm," Applied Optics **37**(21), 4933–4935 (1998).

[171] T. W. M. Lauterborn, W. Kurz, *Coherent Optics* (Springer Berlin Heidelberg, 1995).

[172] J. Dong and K. I. Ueda, "Longitudinal-mode competition induced instabilities of Cr^{4+}, Nd^{3+}: $Y_3Al_5O_12$ self-Q-switched two-mode laser," Applied Physics Letters **87**(15), 151102 (2005).

[173] S.-Y. Tsai, C.-P. Chiu, K.-C. Chang, and M.-D. Wei, "Periodic and chaotic dynamics in a passively Q-switched Nd:$GdVO_4$ laser with azimuthal polarization," Optics Letters **41**(5), 1054 (2016).

[174] T. S. Lomheim and L. G. DeShazer, "Optical-absorption intensities of trivalent neodymium in the uniaxial crystal yttrium orthovanadate," Journal of Applied Physics **49**(11), 5517–5522 (1978).

[175] A. Brenier, C. Tu, Z. Zhu, and J. Li, "Diode pumped passive Q switching of Yb^{3+} -doped $GdAl_3$ $(BO_3)_4$ nonlinear laser crystal," Applied Physics Letters **90**(7), 071103 (2007).

[176] X. Chen and B. Di Bartolo, "Temperature dependence of spectral linewidths and lineshifts of Nd $^{3+}$ ions in $CaY_2Mg_2Ge_3O_{12}$ laser crystal," Journal of Applied Physics **75**(3), 1710–1714 (1994).

[177] J. G. Sliney, K. M. Leung, M. Birnbaum, and A. W. Tucker, "Lifetimes of the $^4F_{3/2}$ state in Nd : YVO_4," Journal of Applied Physics **50**(5), 3778–3779 (1979).

[178] N. I. Khan, S. H. Choudhury, and A. A. Roni, "A comparative study of the temperature dependence of lasing wavelength of conventional edge emitting stripe laser and vertical cavity surface emitting laser," in *IEEE International Conference on Optical Communication Systems*, pp. 141–145 (INSTICC, 2011).

[179] L. McDonagh, R. Wallenstein, R. Knappe, and A. Nebel, "High-efficiency 60 W TEM_{00} Nd:YVO_4 oscillator pumped at 888 nm," Optics Letters **31**(22), 3297 (2006).

[180] R. S. Cudney and C. Minor, "Sub-nanosecond, megawatt compact diode-pumped Nd:YLF laser," Revista Mexicana de Física **64**(5), 512 (2018).

[181] M. Tsunekane, T. Inohara, A. Ando, N. Kido, K. Kanehara, and T. Taira, "High peak power, passively Q-switched microlaser for ignition of engines," IEEE Journal of Quantum Electronics **46**(2), 277–284 (2020).

[182] T. Taira, A. Mukai, Y. Nozawa, and T. Kobayashi, "Single-mode oscillations of laser-diode-pumped Nd:YVO_4," Optics letters **16**(24), 1955–1957 (1991).

[183] D. Jin, Z. Bai, Q. Wang, Y. Chen, Z. Liu, R. Fan, Y. Qi, J. Ding, X. Yang, Y. Wang, and Z. Lu, "Doubly Q-switched single longitudinal mode Nd:YAG laser with electro-optical modulator and Cr^{4+}:YAG," Optics Communications **463**, 125500 (2020).

[184] H. S. Chan, S. Y. Wang, S. T. Lin, and A. H. Kung, "Sub-nanosecond timing jitter in a passively Q-switched microlaser by active Q-switched laser bleaching," Pacific Rim Conference on Lasers and Electro-Optics, CLEO - Technical Digest pp. 12–13 (2013).

[185] A. Kausas and T. Taira, "Timing jitter control by scanning coupled cavity in passively Q-switched Nd: YVO_4/Cr: YAG laser," Advanced Solid State Lasers, ASSL 2014 **2**, 4–6 (2014).

ACKNOWLEDGEMENTS

Conducting this dissertation was a very formative time, during which I learned a great deal from both a professional and personal perspective. In summary, I would like to thank all the people who supported, motivated and inspired me. In particular, I would like to thank...

- Prof. Dr. Thomas Dekorsy, who supported me as my doctoral advisor in all aspects and gave me the great opportunity to complete this doctorate.
- PD Dr. habil. Christian Kränkel for kindly agreeing to be reviewer and for the successful collaboration and great support during the characterization of saturable absorbers.
- Klaus Stoppel, my supervisor, who supported me both professionally and organizationally during my doctoral studies.
- Dr. Heiko Ridderbusch for the professional exchange and support in the Bosch Mentor Program.
- Dr. Hiroki Tanaka for many supportive discussions, ideas, and good cooperation.
- my family and especially my girlfriend Claudia for their patience and gorgeous support in so many ways.